FUNDAMENTAL UNDERSTANDING OF OXYGEN REDUCTION AND REACTION BEHAVIOR AND DEVELOPING HIGH PERFORMANCE AND STABLE HETERO-STRUCTURED CATHODES

Federal Agency: Deportment of Energy – National Energy Technology Laboratory

Award Number: DE- FE00009675

Project Title: Fundamental Understanding of Oxygen Reduction and Reaction Behavior and Developing High Performance and Stable Hetero-structured Cathodes

Principal Investigator: Dr. Xingbo Liu
(304) 293-3339
Xingbo.Liu@mail.wvu.edu

Submission Date: November 14, 2016

DUNS Number: 929332658

Recipient Organization (Name and Address): West Virginia University
Morgantown, West Virginia 26506

Project/Grant Period (Start Date, End Date): October 1, 2012 to May 31, 2016

Reporting Period End Date: May 31, 2016

Report Term or Frequency: Final Technical Report

Signature of Submitting Official (electronic signatures (i.e., Adobe Acrobat) are acceptable)

11/15/2016

Abstract

New unique hetero-structured cathode has been developed in this project. $La_2NiO_{4+\delta}$ (LNO) as a surface catalyst with interstitial oxygen defects was introduced onto the state-of-the-art $(La_{0.6}Sr_{0.4})_{0.95}Co_{0.2}Fe_{0.8}O_{3-\delta}$ (LSCF) cathode to enhance the surface-limited ORR kinetics on SOFC cathode. Furthermore, the hetero-structured cathode surface maintains high activity under electrode polarization with much less negative effects from surface cation segregation of Sr, which is known to cause degradation issues for conventional LSCF and LSC cathodes, thus improving the cathode long-term stability. The interface chemistry distribution and oxygen transport properties have been studied to prove the enhancement of power out and stability of LNO-infiltrated LSCF cathode. The further investigation demonstrates that CeO_2 & $La_{2-x}NiO_{4+\delta}$ (x=0-0.2) co-infiltration is a simple and cost-effective method to improve both performance and stability of LSCF cathode by limiting nano-particles growth/delamination and further improve the surface stability.

For the first time, a physical model is proposed to illustrate how unique interstitial species on hetero-structured cathode surface work to regulate the exchange rate of the incorporation reaction. Meanwhile, fundamental investigation of the surface oxygen exchange and bulk oxygen transport properties under over-potential conditions across cathode materials have been carried out in this project, which were discussed and compared to the Nernst equation that is generally applied to treat any oxide electrodes under equilibrium.

Table of Contents

List of Figures

List of Tables

1.0 Executive Summary

Objectives: The primary objectives of this project were aimed at the development of highly active and stable intermediate temperature solid oxide fuel cell cathodes by improving ORR kinetics and enhancing cation segregation tolerance through the introduction of a hetero-structured oxygen reactive interface on the LSCF cathode surface and/or the TPB area between the cathode and electrolyte (YSZ/GDC). Meanwhile, the another focus of the project work is to promote fundamental understanding of the surface and bulk defect/cation-chemistry related oxygen electrode activity and stability by establishment of both a novel experimental protocol and a theoretical continuum model to analyze the physical characteristics and reaction kinetic parameters governing oxygen transport in the hetero-structured cathode material.

Project description: This project are (1) to develop cathodes with hetero-structured surfaces that demonstrate high performance and stability, via low-cost infiltration method; and (2) to develop the fundamental understanding of the oxygen reduction and reaction (ORR) mechanisms, especially the oxygen exchange/transport behavior between the hetero-structured surface (LNO nicklate) and bulk (perovskite) of the cathode under over-potential through systematic experimental investigations and theoretical modeling;.

Accomplishment to date: New unique hetero-structured cathode has been developed in this project. $La_2NiO_{4+\delta}$ (LNO) as a surface catalyst with interstitial oxygen defects was introduced onto the state-of-the-art bulk $(La_{0.6}Sr_{0.4})_{0.95}Co_{0.2}Fe_{0.8}O_{3-\delta}$ (LSCF) to enhance the surface-limited ORR kinetics for cathode side. Furthermore, the hetero-structured cathode surface maintains high activity under electrode polarization with fewer negative effects from surface cation segregation of Sr, which is known to cause degradation issues for conventional LSCF and LSC cathodes, thus improving the cathode long-term stability. The higher interface oxygen exchange coefficient (3×10-4 cm/s), with respect to that of bare LSCF cathode (9.02×10-5cm/s), indicates that the incorporation rate of oxygen into LSCF is enhanced when using LNO/LSCF cathode. A low degradation rate of 0.39% at a constant current density for the fuel cell using LNO-infiltrated LSCF cathode can be still achieved after long-term durability of about 500 h at 750^{o}C. The interface chemistry distribution and oxygen transport properties have been studied to prove the enhancement of power out and stability of LNO-infiltrated LSCF cathode. The Co and Sr diffusion, as well as higher interstitial oxygen and oxygen vacancy concentration, have been detected in surface LNO layer by XPS and TEM-EDX data. For the first time, a physical model is proposed to illustrate how unique interstitial species on hetero-structured cathode surface work to regulate the exchange rate of the incorporation reaction. The further investigation demonstrates that CeO_2 & $La_{2-x}NiO_{4+\delta}$ (x=0-0.2) co-infiltrated LSCF is one potential infiltration materials for bare LSCF cathode to limit nano-particles growth/delamination and further improve the surface stability based on CeO_2 high melting point & wetting properties and $La_{2-x}NiO_{4+\delta}$ high surface chemical stability.

Fundamental understanding of the surface oxygen exchange and bulk oxygen transport properties under over-potential conditions across cathode materials have been carried out in this project. The alternation of the local chemical composition of the electrode materials and electrical boundary conditions under service condition usually ~0.3 V over-potential have been discussed and compared to the Nernst equation that is generally applied to treat any oxide electrodes under equilibrium. It is found that the electrode bulk is not locally electro-neutral and the resultant electrostatic gradient can be established in the region near electrolyte due to the uneven distributions of ions and electrons. Therefore, besides the concentration gradient, electrical field force produced by the electrostatic potential is also the driving forces in the ion diffusion and introduces new concepts in handling chemical and electrical contributions in the overall electrochemical response of electrode system. Meanwhile, the uncoordinated relationship on

electrode resistance is found between thermodynamic (oxygen partial pressure) and electrochemical (over-potential) activated conditions based on the Nernst equation. This Non-Nernst behavior demonstrates that it should be cautious to choose the effective activity or concentration used in Nernst equation to build the equivalence relation between thermodynamic and electrochemical driving force and predict performance of electrode.

Potential Impact: This project will provide fundamental understanding on the surface defect/cation-chemistry related oxygen electrode activity and stability by establishment of both novel experimental protocol and theoretical model to analyze the physical characteristics and reaction kinetic parameters governed oxygen transport across the hetero-interface on cathode material. In the meantime, this project will provide a pathway to develop next generation cathode with both high performance and stability, while the methodology applied in this project requires minimum alteration of technologies that are currently employed by SECA industrial teams.

Major Participants: West Virginia University; National Energy Technology Laboratory, which helped to investigate the long term stability of SOFCs with WVU infiltrated cathode.

2.0 Results and Discussion

Task 1: Program Management

Task 1.1 Project Management Plan

The project management plan was submitted within 30 days after the award and the principle investigator kept in communication with the project officer at NETL with any changes or deviations from the agreed upon plan. All quarterly reports were submitted within a timely manner and the PI tracked project tasks against the project timeline and the project management plan to ensure that milestones were being met. All project tasks and milestones have been completed.

Subtask 1.2 Project Communications

The principle investigator kept in communication with the project officer at NETL about the status of the project, any issues regarding the project, and concerns about the timeline. The PI also gave tours throughout the project to the project officer and other NETL researchers to keep them up to date on the status of the project and the laboratory testing.

Task 2: Fundamental Understanding of the ORR kinetics under over-potential conditions

Instead of open circuit voltage conditions, electrodes are usually operated under constant over-potential, which supplies additional energy for electrode resistance compensation, when the cells are run with external circuit. However, the lack of a clear understanding of the change of physical properties locally in the materials bulk under non-equilibrium condition with steady net current calls for further investigation in which surface oxygen exchange and bulk oxygen transport properties are studied under over-potential conditions.

Task 2.1 Fundamental Understanding of Over-potential Effect on Bulk Oxygen Transport

In this part, parallel charged species pathways in MIECs were considered, and oxygen defects and potential distribution in cathode bulk were investigated. Oxygen intermediates and defect distribution were considered for simulating the potential distribution across the cathode.

Firstly, the influence of over-potential on the bulk pathway was dedicated, which will be discussed and compared to the Nernst equation that is generally applied to treat any oxide electrodes under equilibrium. The relevant potentials controlling electrode processes include electrostatic potential, electrochemical potential of electron and ion. The distributions of those potentials and resultant influence on electrode processes are treated with drift diffusion equations. It is found that the electrode bulk is not locally electroneutral and the resultant electrostatic gradient can be established in the region near electrolyte due to the uneven distributions of ions and electrons. Therefore, besides the concentration gradient, electrical field force produced by the electrostatic potential is also the driving forces in the ion diffusion and introduces new concepts in handling chemical and electrical contributions in the overall electrochemical response of electrode system.

Such electron-ion current transition starts from the upper boundary of the active length, finishes outside electrolyte with electronic current finally blocked. The active length estimated from chemical capacitance for cathode material (not available now for oxide anodes) by Adler et al. can be as big as 7~15 μm depending mainly on D/k and microstructure. The transport path in MIEC near electrolyte actually can be illustrated as in Fig. 2.1. Though 3PB reaction in lots of cases is important to the overall electrode kinetics as well, it is ignored here in order to focus our topic to 2PB exclusively. Oxygen ions are transported inside the MIEC from the MIEC/electrolyte interface to MIEC inner surface, as indicated by the red lines. According to the current density inside different portion of MIEC, the electrochemical equipotential lines (ELs) for oxygen is drawn

qualitatively also. For segment between any two ELs, the transport behavior inside it can be simplified into a 1-dimensional case as shown in Fig. 2.1c, which renders simpler mathematical treatment without loss the important physical essence. The driving force of such transport has in lots of cases been ascribed to the oxygen vacancy gradient alone, and the influence or even the existence of electrical field was neglected, most probably because it seems impossible to build electrical field inside the bulk of a conductive material. The existence of electrical field in MIEC bulk and the distributions of defects and potentials herein will be analytically derived first; then independently solved from the governing equations also based on the 1-dimensinoal model.

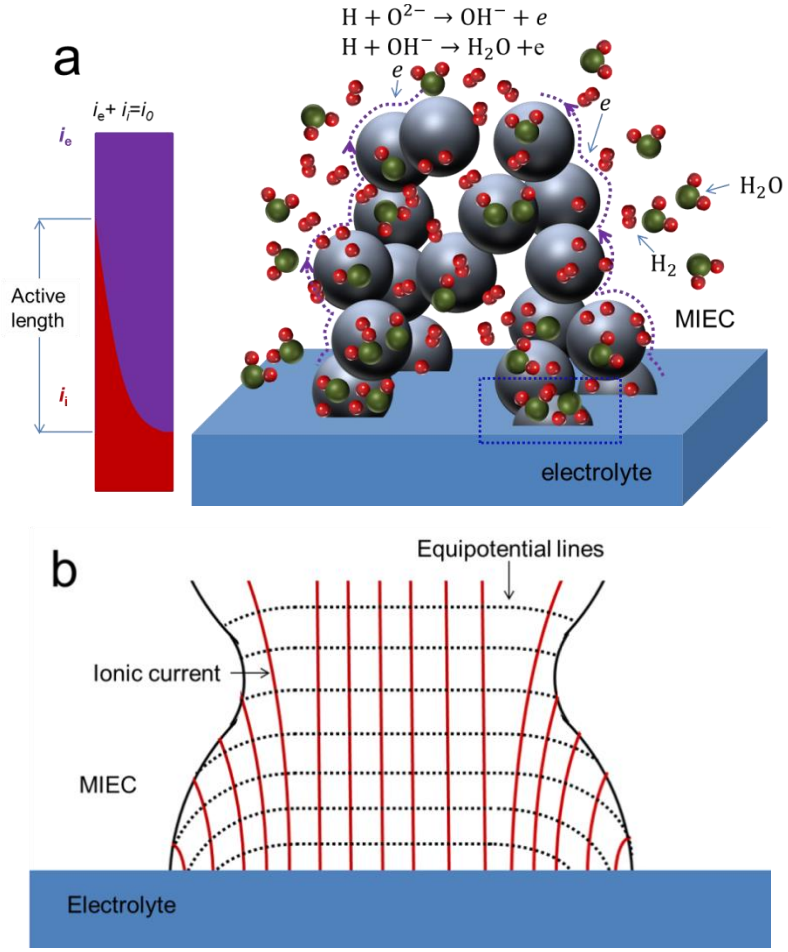

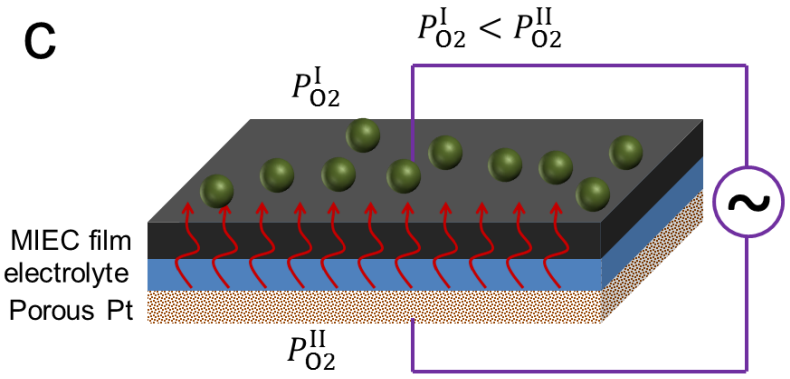

Figure 2. 1 Schematic diagram for MIEC anode operation (a), the ionic flowing and equipotential lines at MIEC anode near the interface area (b), and the 1-D model derived based on it (c).

The motion of chemical species in MIEC electrode is governed by the Nernst-Planck equation. For one-dimension case, the mass flux of species i under steady state takes the form as:

$$j_i^{\text{mass}}(x) = -D_i \frac{\partial c_i(x)}{\partial x} - \frac{\sigma_i}{z_i e} \frac{\partial \phi(x)}{\partial x} \tag{2.1}$$

where x is the position, Di the chemical diffusion coefficient, ci the concentration, σi the conductivity, ϕ the galvanic potential, zi the valence, e the electron charge. The first term in RHS represents the diffusion, and second term migration.

According to the Nernst-Einstein relationship, the equation above can be rearranged as:

$$j_i^{\text{mass}}(x) = -\frac{\sigma_i}{(z_i e)^2} \frac{\partial \tilde{\mu}_i(x)}{\partial x} \tag{2.2}$$

where

$$\tilde{\mu}_i(x) = \mu_i(x) + z_i e \phi(x) \tag{2.3}$$

$$\mu_i(x) = \mu_i^0(x) + \mathrm{k_B} T \ln c_i(x) \tag{2.4}$$

is the electrochemical and chemical potentials, respectively. k_B and T remain the usual physical meanings.

The current density, Ii=zie j_i^{mass}, is then

$$I_i(x) = -\frac{\sigma_i}{z_i e} \frac{\partial \tilde{\mu}_i(x)}{\partial x} \tag{2.5}$$

The current of charged species in the solid bulk is determined by its electrochemical potential gradient.

For clarity, the electronic species is henceforth indicated by the subscript “e”, and the ionic one by “v” in view of oxygen vacancy being the most common ionic defect in MIEC electrode materials. Assuming the electrolyte is purely ionic conductive at this moment, when a certain current, I0, is

flowing through the electrolyte, the ionic and electronic currents in the MIEC film will be I0 and 0, respectively, given that there is no sink or source for either electrons or ions in MIEC under steady state. According to Eq. 2.5, the electrochemical potential of electrons, $\tilde{\mu}_{\mathrm{e}}(x)$, is constant along the thickness of electrode.

Partial differentiation of Eq. 3.3 with respect to x for electron is

$$\frac{\partial \tilde{\mu}_{\mathrm{e}}(x)}{\partial x} = \frac{\partial \mu_{\mathrm{e}}(x)}{\partial x} - e\frac{\partial \phi(x)}{\partial x} = 0 \tag{2.6}$$

In order to investigate the galvanic potential term above, let us make an assumption on the electron chemical potential as $\frac{\partial \mu_{\mathrm{e}}(x)}{\partial x} = 0$, that is, the electrons are evenly distributed in the anode bulk. Such assumption yields $\frac{\partial \phi(x)}{\partial x} = 0$ accordingly, meaning no electrical field inside the bulk.

With this result, for the ionic current on the other hand, the ionic concentration gradient in anode bulk serves as the only driving force for ionic flux as in Eq. 2.7:

$$\frac{\partial \tilde{\mu}_{\mathrm{v}}(x)}{\partial x} = \frac{\partial \mu_{\mathrm{v}}(x)}{\partial x} + 2e\frac{\partial \phi(x)}{\partial x} = \frac{\partial \mu_{\mathrm{v}}(x)}{\partial x} = -\frac{2e}{\sigma_{\mathrm{v}}} i_0 \tag{2.7}$$

Inserting Eq. 4 for ion into Eq. 7.7, one obtains

$$\frac{\mathrm{k_B}T}{c_{\mathrm{v}}(x)}\frac{\partial c_{\mathrm{v}}(x)}{\partial x} = -\frac{2e}{\sigma_{\mathrm{v}}} i_0 \tag{2.8}$$

As a result, the oxygen ion defects are not uniformly distributed in the anode bulk. Given the even cation charge background and the assumed uniform distribution of electrons, the local charge density at position x in the bulk, ρ(x), is

$$\rho(x) = \Sigma z_{\mathrm{cations}} e c_{\mathrm{cations}} - c_{\mathrm{e}} - 2e\mathrm{A}_0 + 2ec_{\mathrm{v}}(x) = 2ec_{\mathrm{v}}(x) + \mathrm{const} \not\equiv 0 \tag{2.9}$$

where A_0 is the theoretical volume density of oxygen lattice sites.

Poisson's equation for one-dimension case writes

$$\frac{\partial^2 \phi(x)}{\partial x^2} = -\frac{\rho(x)}{\varepsilon_0 \varepsilon} \tag{2.10}$$

Inserting Eq. 2.9 into Poisson's equation, it ends up with $\frac{\partial \phi(x)}{\partial x} \neq 0$, which is contradictory to the deviation before under the assumption of $c_e(x)$=constant. Such contradiction clearly demonstrates this assumption is not self-consistent, therefore cannot be true. There exist local net charges and electrical field inside the MIEC anode bulk. Such logical reasoning is illustrated in Fig. 2.2

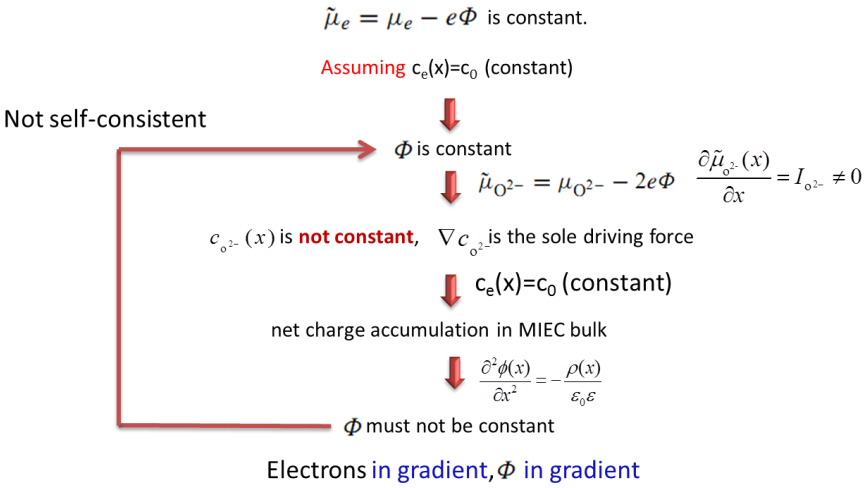

Figure 2. 2 logical flow chart for the possible distribution of electronic defects and the existence of galvanic potential in MIEC bulk.

With regard to the theoretical analysis above, a couple of points in the reasoning process need to be remarked. The first is the purely ionic conductivity for electrolyte. In reality, no matter how small it is, the electronic conductivity in electrolyte material will not be 0 strictly. The significance of the electronic conductivity in electrolyte has been addressed by Virkar. It was shown that such conductivity is one of the most important parameters for one to determine the profile of $\tilde{\mu}_e(x)$ and the equivalent oxygen partial pressure inside electrolyte. However, assuming an ideal ion-conductive electrolyte will not affect the validity of the analysis above, because, in principle, the ion transport from electrolyte to anode and the building-up of voltage difference between cathode and anode in Fig. 2.1c, or in other words, the applicability of Nernst equation, do not exclude the existence of electronic conductivity in the electrolyte. Secondly, we leave out the charges located at boundaries but only focus on the local charges in bulk. The abrupt change in electrical properties at the boundary of two phases leads to the relocation of charges, which breaks the local neutrality as a result. From the viewpoint of traditional electrode investigation, where the charge neutrality is always assumed in the bulk, one would believe that those boundary charges may strongly affect the specific value of electrical field inside the anode. However, in the present case, studied is the very relationship between charges and electrical field. The local neutrality assumption is not adopted here, since it is actually one of the subjects to be addressed as will be shown later. Poisson's equation is the governing law, theoretically formulizing the relationship between charges and the change of electrical field. Therefore, making use of this equation will neither omit nor double-count the influence from any relevant charges. In this regard, boundary charges need not to be considered additionally. At last, the conductivities have been implicitly taken as constant and independent to the concentration of charge carriers. Such practice is adopted to keep equations tidy and will not affect the nature of this problem qualitatively. With those issues clarified, it is clear to us now that the analysis above is physically rigorous and the

electrical field is built inside the anode bulk regardless of the high electrical conductivity the anode materials may possess.

To determine the correct electron distribution profile and other related properties in MIEC bulk, three simplified scenarios are tried. The first scenario is drawn as Fig. 2.3a. For uneven distribution, the population of electrons is assumed to decrease from anode surface (S) to anode/electrolyte interface (I), which leads to a tendency of electron flux from S to I due to the concentration gradient. Cancelling out such tendency to reach a zero net electron current requests the electrical field to be established as illustrated in Fig. 2.3a. The corresponding local positive and negative charges inside the bulk come from the relocation of electronic and ionic defects. Then, the population of ionic defects, $V_o^{\cdot\cdot}$, must increase from I to S in order to yield the electrical field as such. The ionic current corresponding to the influence from vacancy gradient and electrical field is denoted as I_{grad} and I_{fld} respectively. One can easily find both I_{grad} and I_{fld} flow from S to I in this circumstance, and the overall ionic current as a sum of I_{grad} and I_{fld} will be from S to I also, which is in consistence with the real situation at marked by the arrow above. The second scenario is drawn as Fig. 2.3b. The population of electrons is assumed to increase from S to I this time. With the same routine, it ends up with two ionic current flowing from I to S, making the overall current opposite with the real one in direction, therefore is impossible. Monotonic change of electron population from one side to the other has been used in those two cases. In the last case, a non-monotonic change will be tried. As displayed in Fig. 2.3c, the electron population from S to I first increases to the peak then starts to decrease. Likewise, it can be readily determined that the overall current will flow from the middle of the MIEC to the sides, which is nonsense. Of course, the electron population can decreases first, and then rises back from S to I, which just changes the detail and will not bring anything new. In fact, there are countless different examples for the non-monotonic case, but the particular example used here along with those two monotonic ones can represent all scenarios. Among them, only the case shown in Fig. 2.3a coincides with the real situation. The finding that electrons cannot be uniformly distributed in the anode bulk and an electrical field must exist is obtained without any boundary condition restriction, which simply means that the MIEC segment subject to study can be the whole anode bulk, or any pieces of volume inside the bulk. Therefore, whatever the specific non-monotonic distribution looks like, it will end up with contradictory result.

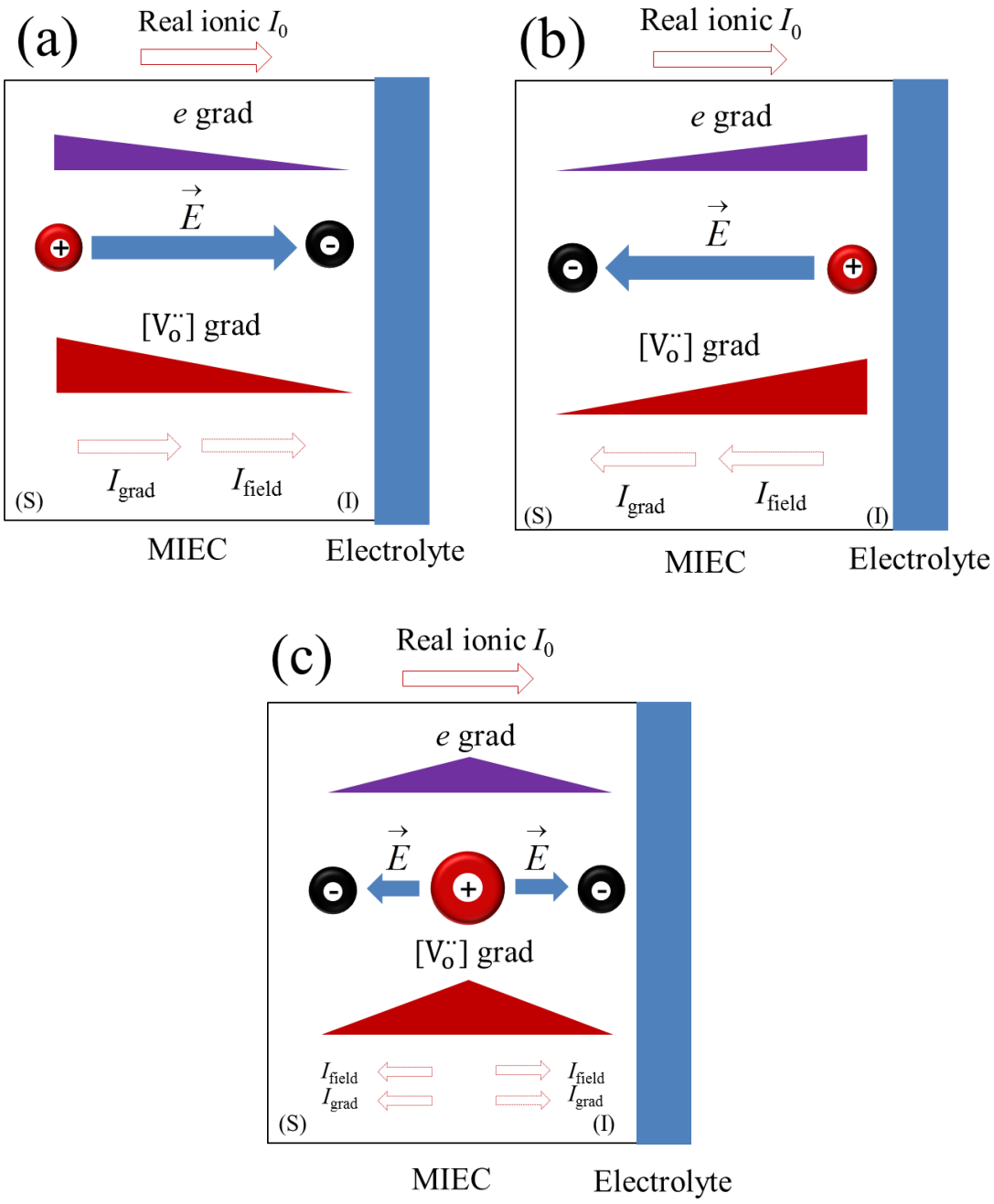

Figure 2. 3 Three scenarios for the defects distribution in MIEC anode under steady state with current I_0.

By making use of Eq. 2.4 and 2.5, the scenario in Fig. 2.3a can be interpreted into Fig. 2.4b with specific parameters including cv, ce, ϕ and etc. The situation under OCV is also described in Fig. 2.4a for comparison. As the ion transport behavior in MIEC cathode is not different from anode here in terms of the governing equations, those properties are extended into the cathode for the sake of completeness. The transition of those parameters from anode to cathode through electrolyte is arbitrarily illustrated. And the complexity concerning the interface properties, though

very important, is left out here in order to focus on the MIEC bulk. For more informative study regarding the interface and electrolyte, one is recommended to refer to Virkar's work. Under OCV, all parameters display a uniform profile throughout the MIEC film in both cathode and anode sides. The Nernst potential EN represented as

$$E_{\mathrm{N}} = \frac{RT}{4F} \ln \frac{P_{\mathrm{O}_2}^{\mathrm{I}}}{P_{\mathrm{O}_2}^{\mathrm{II}}} \tag{2.11}$$

is equal to Vocv under the assumption of zero electronic conductivity in electrolyte.

$$E_{\mathrm{N}} = V_{\mathrm{ocv}} = \frac{{}_{\mathrm{c}}\tilde{\mu}_{\mathrm{e}} - {}_{\mathrm{a}}\tilde{\mu}_{\mathrm{e}}}{-F} \tag{2.12}$$

As can be seen in Fig. 2.4a, both EN and the galvanic potential are built up inside the electrolyte. Under steady state with a certain current flowing, the transport of ion is positively driving by both electrical field and cv gradient. The contribution from each of them trade off with one another to yield a certain difference in $\tilde{\mu}_{\mathrm{v}}$ from surface to interface that can be determined from impedance measurement. Decreasing in cv from surface to interface may limit the MIEC performance by a resultant reduced ionic conductivity in the most active area, but on other hand also be able to stabilize the material near interface if cv is small enough. Therefore, cv is of particular interest with respect to the performance reduction/enhancement upon polarization and electrode reliability under large load. As cv(x) is tied to ϕ(x), it cannot be simply determined from the material stoichiometry data at the calculated PO_2 through Eq. 2.11, since the contribution from ϕ will decrease the change in cv. Quantification of cv and ϕ requires to solve those equations analytically or numerically.

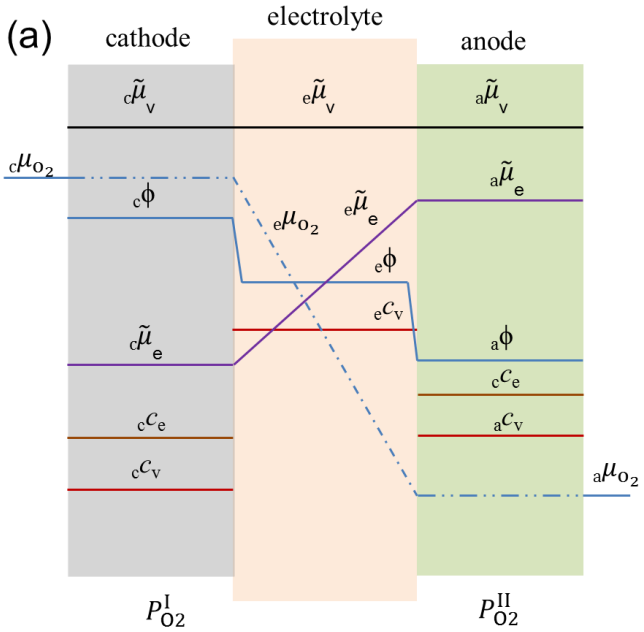

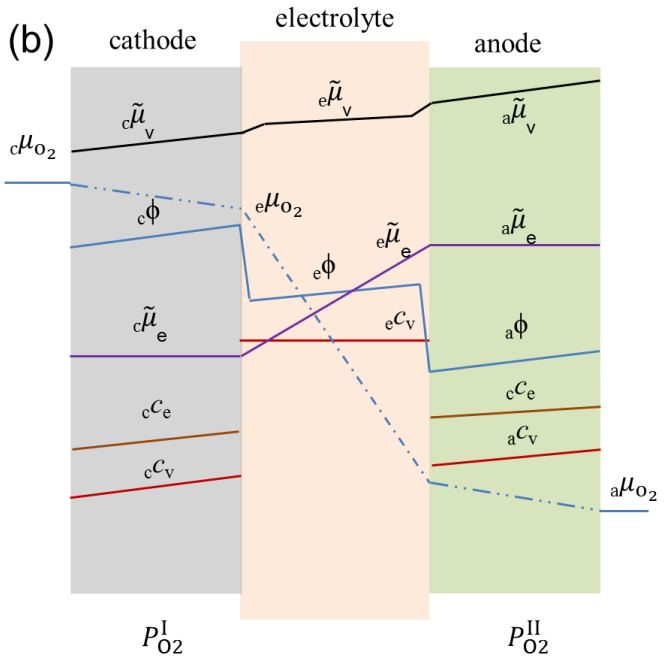

Figure 2. 4 Three scenarios for the defects distribution in MIEC anode under steady state with current I_0.

In the 1-dimensinal MIEC cathode model, if assuming electron and oxygen vacancy as charge carrier, the governing equation set under steady state can be rearranged as:

$$\frac{\partial c_v(x)}{\partial x}+\frac{2F}{RT}c_v\frac{\partial \phi(x)}{\partial x}=\frac{j_v^{mass}}{-D_v} \tag{2.13}$$

$$\frac{\partial c_e(x)}{\partial x}-\frac{F}{RT}c_e\frac{\partial \phi(x)}{\partial x}=0 \tag{2.14}$$

$$\frac{\partial^2 \phi(x)}{\partial x^2}=-\frac{\rho(x)}{\varepsilon_0\varepsilon} \tag{2.10}$$

The difficulty in solving such so-called Nernst-Planck-Poisson system lies in the non-linearity. To obtain analytical solutions, assumptions need to be made to replace Poisson's equation. Two assumptions have been used widely in the pertaining studies, namely electro-neutrality and constant field assumption. As one can readily find that electro-neutrality leads to constant field and vice versa when inserting it back to Poisson's equation, it may be confusing to understand the difference between those two assumptions. In this regard, the related background will be briefly reviewed here. Electro-neutrality was adopted by Planck himself in 1890 to develop solution for the steady state Nernst-Planck equation. Such assumption seems largely reasonable in view of basic physical conceptions on conductive materials. And justification for it is usually realized by the fact that if under appropriate use, inserting back the obtained galvanic potential into Poisson's

equation yields small, though not constantly zero, charge density. On the other hand, Goldman in 1943 introduced the constant field assumption to solve the transport properties in a conductive membrane under steady state. Such assumption reduces the 2-order differential Poisson's equation into 1-order, and allows one to integrate the Nernst-Planck equations (2.13) and (2.14) directly. Despite the simplicity brought by these two assumptions, the fundamental concerns associated with the validity of them can be summarized as: (1) why in the first place they can be consistent with Poisson's equation; (2) and if they are, do they cover all the circumstances where Eq.2.10 is applicable. Later on, MacGillivray et al. clarified above concerns, and demonstrated with the perturbation theory that the electro-neutrality and constant field assumptions are nothing else but two extreme cases of Poisson's equation. The applicability of each hypothesis can be evaluated based on a dimensionless factor,

$$\alpha^2 = \left(\frac{\varepsilon\varepsilon_0 \mathrm{k_B} T}{z^2 e^2 c} / l^2\right) \quad \text{or} \quad \alpha = \frac{\lambda_\mathrm{D}}{l} \tag{2.15}$$

where λD is the Debye length and l sample thickness.

When

α<<1, local electroneutrality applicable;

α>>1, constant field applicable;

α≅1, neither assumption is correct.

As can be seen now, electro-neutrality and constant field hypotheses are used under totally opposite circumstances.

In the present case, for most MIEC materials in SOFCs application, assuming T=1000K, ce≅cv≅4000 mol/m3 (i.e. ~0.3/unit cell), λD can be calculated as 4×10-22ε m, a value far smaller than the active length of 1~10 μm for MIEC cathode given ε in the range of 1012~1014 .

Therefore the electro-neutrality can be the appropriate approximation here. Poisson's equation is replaced by

$$2cv - ce - ca = 0 \tag{2.16}$$

where ca is positive for the acceptor dopant and negative for donor dopant.

Inserting Eq. 2.16 into 2.13 to eliminate cv, then subtracting 0.5×Eq. 2.14, one obtains

$$\left(\frac{3}{2}c_\mathrm{e} + c_\mathrm{a}\right)\frac{F}{RT}\frac{\partial\phi}{\partial x} = \frac{j_\mathrm{v}^\mathrm{mass}}{-D_\mathrm{v}} \tag{2.17}$$

Inserting Eq. 2.14 into Eq. 2.17,

$$\left(\frac{3}{2} + \frac{c_\mathrm{a}}{c_\mathrm{e}}\right)\frac{\partial c_\mathrm{e}}{\partial x} = \frac{j_\mathrm{v}^\mathrm{mass}}{-D_\mathrm{v}} \tag{2.18}$$

Integrating Eq. 2.18 yields

$$x = -\frac{D_{\mathrm{v}}}{j_{\mathrm{v}}^{\mathrm{mass}}}\left(\frac{3}{2}c_{\mathrm{e}} + c_{\mathrm{a}}\ln c_{\mathrm{e}}\right) + const \tag{2.19}$$

where const is a constant determined by boundary conditions.

The explicit solution of ce towards x cannot be developed as the inverse function is not applicable. Therefore Matlab computing is introduced to display the profiles of ce, then cv and ϕ. In particular, the contribution comparison between electrical field and chemical gradient for ion transport can be evaluated now. According to Eq. 2.13, the ratio can be represented as

$$r_{\mathrm{E/C}} = \frac{f_{\mathrm{ele}}}{f_{\mathrm{che}}} = \frac{\frac{2F}{RT}c_{\mathrm{v}}\frac{\partial\phi}{\partial x}}{\frac{\partial c_{\mathrm{v}}}{\partial x}} = \frac{4c_{\mathrm{v}}}{c_{\mathrm{e}}} \tag{2.20}$$

For a clear contrast, the distribution of cv under the assumption of no electrical field contribution is also provided based on Fick's 1st law,

$$-D_{\mathrm{v}}\frac{\partial c_{\mathrm{v}}(x)}{\partial x} = j_{\mathrm{v}}^{\mathrm{mass}} \quad \text{or} \quad c_{\mathrm{v}}(x) = \frac{j_{\mathrm{v}}^{\mathrm{mass}}}{-D_{\mathrm{v}}}x + const \tag{2.21}$$

In principle, there are four combinations of electronic/ionic defects in MIEC materials (though not all can be found in or belong to the presently available anode category):

e-V, electron-vacancy, e.g. (LaSr)TiO_3 anode;

h-V, hole-vacancy, e.g. YCCC, YCCN anodes, or (LaSr)(CoFe)$O_{3-\delta}$ cathode;

e-O, electron-interstitial oxygen;

h-O, hole-interstitial oxygen, e.g. $La_2NiO_{4+\delta}$ in O-hyperstoichiometry regime;

Similar to the e-V case, the solutions for the rest combinations can be derived via the same route. To answer the question whether the results solved from equations above and that from the previous qualitatively analysis as in Fig. 2.4 is consistent with each other or not, e-V case is exhibited first.

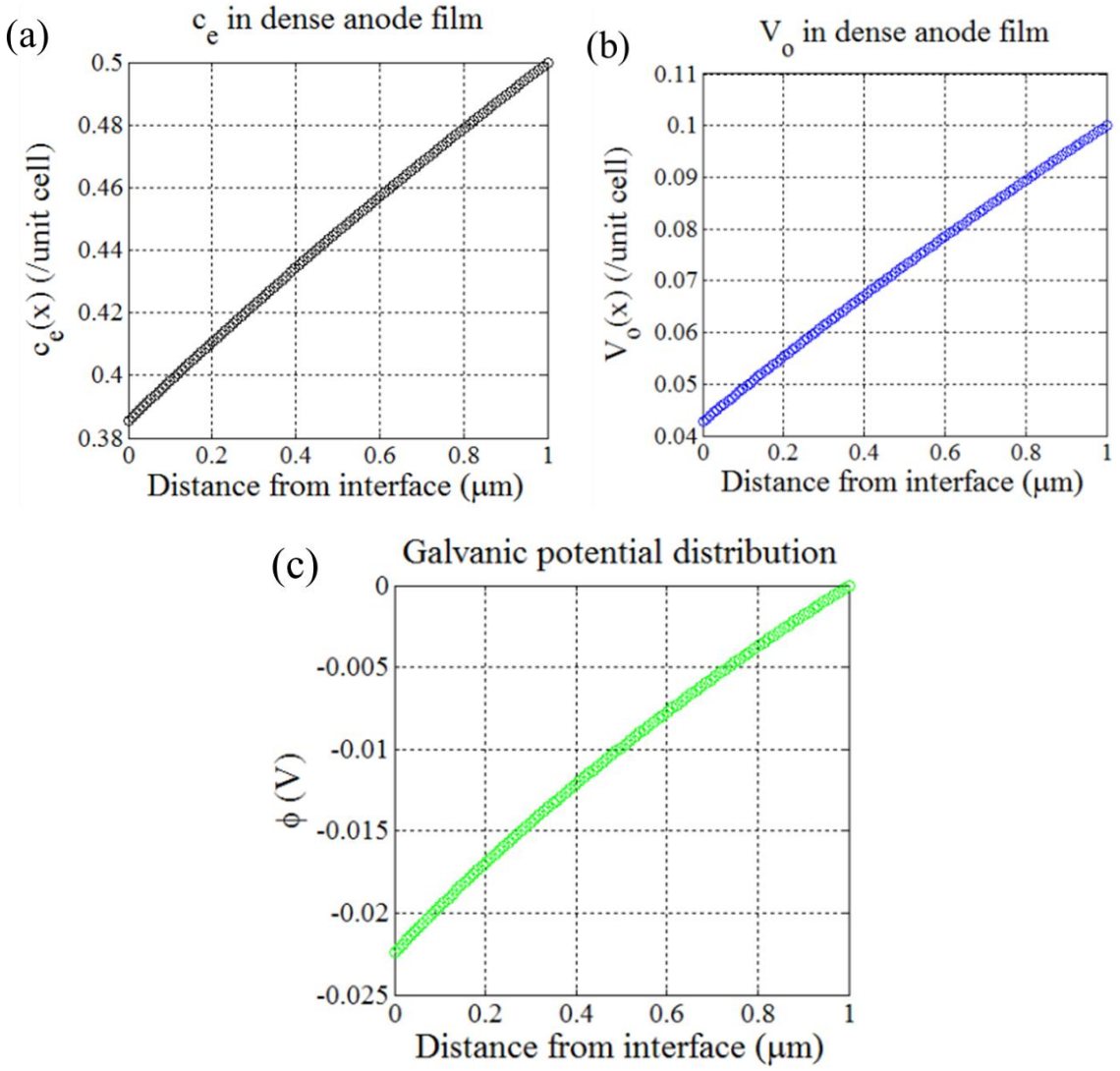

Figure 2.5 Electron (a) and vacancy (b) and galvanic potential distributions in a 1μm La0.3Sr0.7TiO3 anode film as the e-V type.

Using $La_{0.3}Sr_{0.6}TiO_3$ (LST) to represent the e-V type, and setting the boundary condition ce=0.5/unit cell at the anode surface, and i=0.5 A/cm^2, Dv=10-7 cm^2/s, T=1000 K, the local concentration of charge carriers and galvanic potential in LST can be solved. The results are displayed in Fig. 2.5. Under steady state ce, cv, ϕ all increase from surface to interface, showing perfect agreement with the case in Fig. 2.4b. The galvanic potential ϕ is set as 0 at the anode/electrolyte surface since only the potential difference matters. Obviously ϕ is not even inside the MIEC bulk, challenging the usual wisdom that no electrical field is possible inside such a conductor. It should be point out that Dv for LST is roughly set since the real number is still not available in literature. However, it is good enough to show the theoretical principle here. When increasing the current to 1 A/cm2, the corresponding change in those parameters can be shown in Fig. 2.6.

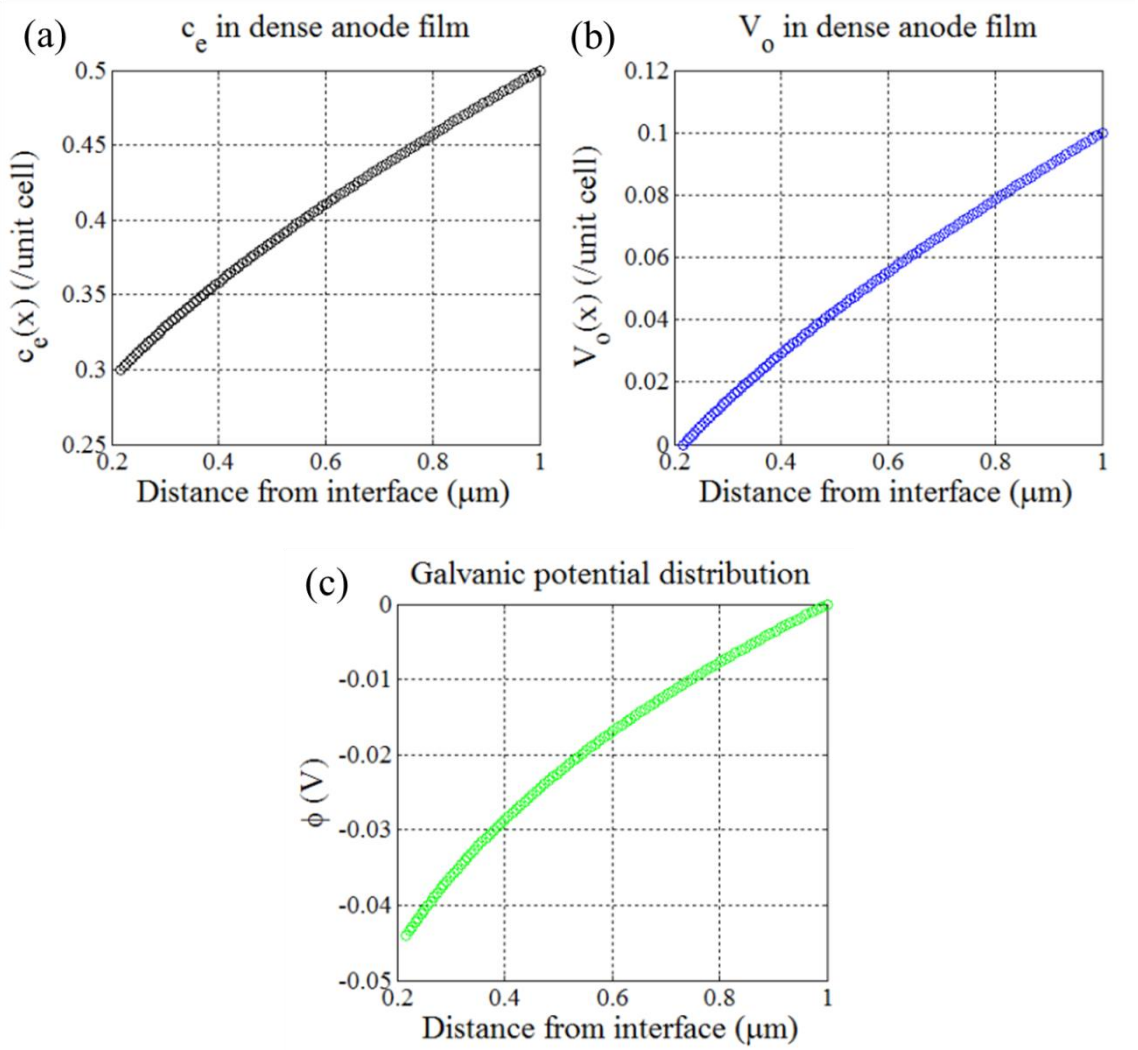

Figure 2.6 Limiting current in LST and the electron (a) and vacancy (b) and galvanic potential distributions (c).

In Fig. 2.6, the current is increased from 0.5 to 1 A/cm2 compared to Fig. 2.5 with other parameters remain unchanged. Those curves are found to stop at 0.2 μm instead of reaching the interface. Surface instead of interface is chosen as boundary to yield boundary conditions since during electrode operation under different conditions, surface exposed to fixed PO_2 or PH_2 is more likely to be known in term of the charge carriers densities. Therefore, such phenomenon in fact means the limiting current is arrived with those given parameters for LST, which reasonably represents the real situation that the bulk diffusion process does not literally obey ohm's law (appears in the polarization response of EIS instead of x-axis intercept), and limiting current can be reach easily with small ion diffusion coefficient.

The results for the rest three cases are displayed in Fig. 2.7-9. Cell volumes are set to 200 Å3 and Dv=10-6 cm2/s, T=1000 K, i=1 A/cm2 and thickness 10 μm. The others parameters used in calculation are listed behind.

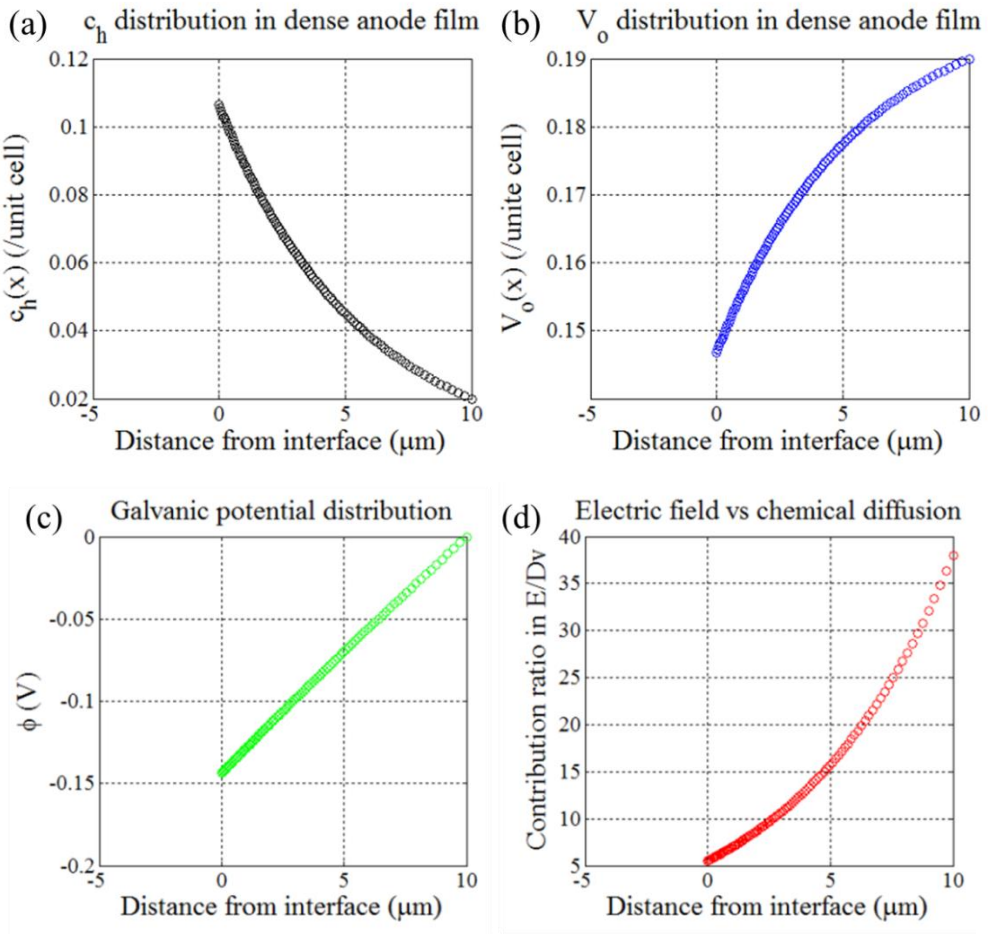

Figure 2. 7 Profiles for ch (a), $V_{\ddot{O}}$ (b), ϕ (c) and rE/C (d) in h-V type with acceptor doping 0.4/unit cell and 0.02/unit cell of ch at surface.

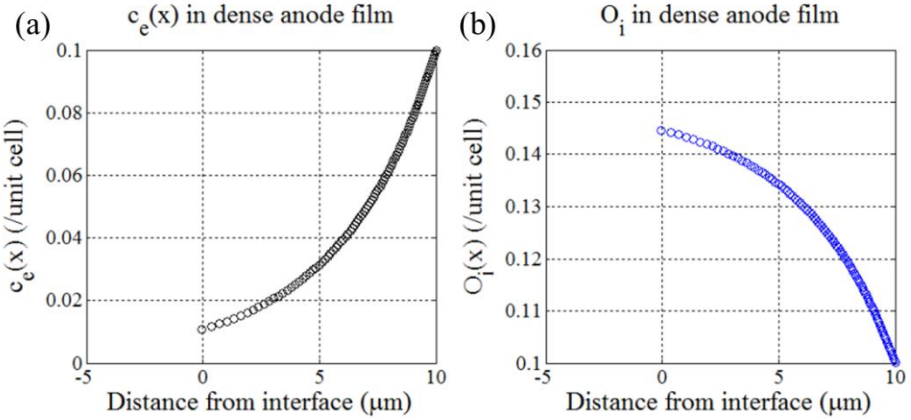

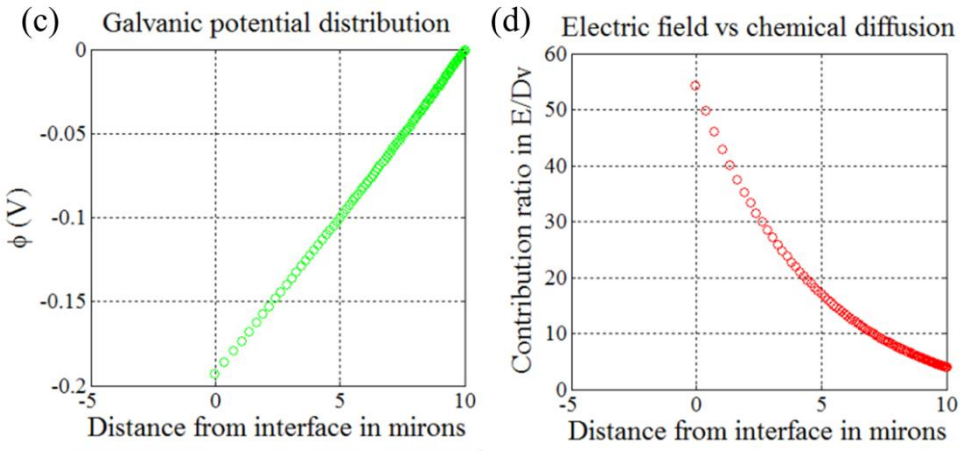

Figure 2. 8 Profiles for ce (a), $0_i''$ (b), ϕ (c) and rE/C (d) in e-O type with donor doping 0.3/unit cell and 0.1/unit cell of ce at surface.

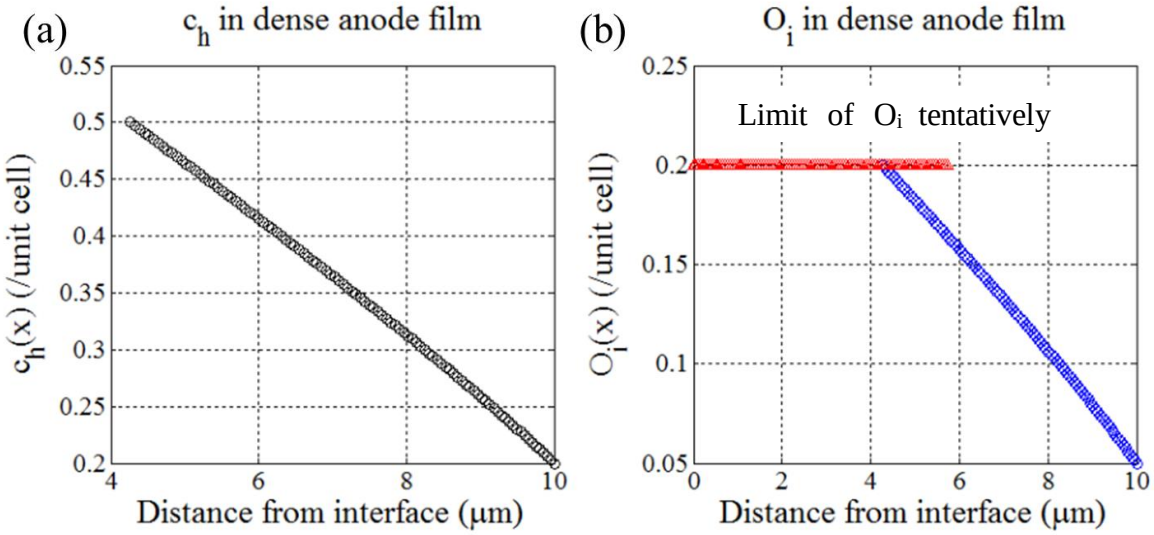

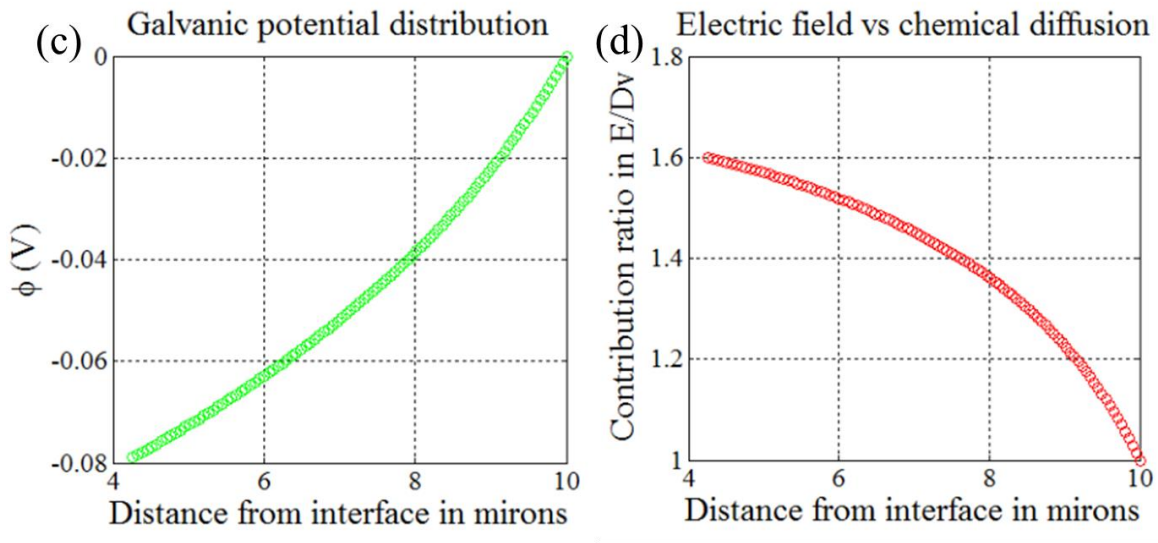

Figure 2. 9 Profiles for ch (a), O_i'' (b), ϕ (c) and rE/C (d) in h-O type with acceptor doping 0.1/unit cell and 0.2/unit cell of ch at surface.

From those figures, it is found that if hole as the opponent of electron is the charge carriers, e.g. in YCCC, the profile shows exactly opposite tendency of electron as shown in Fig. 2.7, the same is also valid when O_i'' replacing $V_O^{\cdot\cdot}$ as the ionic defects as shown in Fig. 2.8. That is in good consistence with the qualitative analysis where only the net charge matters regardless of what the specific form the charge carrier takes. It is also noted that the galvanic potential built inside the bulk with given current 1 A/cm2 is not small at all, but could account for a big portion of the total anode over-potential. The contribution from electrical field in ion transport shown by those figures is even bigger than that from chemical diffusion.

It is worth noting that in the derivation above Dv in Eq. 2.13 is taken as constant regardless of the change of cv along MIEC film. According to the random-walk theory by Goodenough,

$$D_v = D_v^0 \exp(\frac{-\Delta G_m}{k_B T}) \tag{2.22}$$

$$D_v^0 = \frac{l^2}{6} z(1-n_v) f v_0 \tag{2.23}$$

where l is distance between two oxygen sites, z the number of near-neighbor oxygen sites surrounding one oxygen, nv the fraction of vacancy site (proportional to cv), f a geometrical factor depending on the jump path, v0 the attempt frequency. As cv(x)<<3 under the present situation for perovskite MIEC, 1-nv≈1, thus making Dv being constant a reasonable approximation.

To verify those results experimentally, LSCF/GDC half cells were measured. Though anode bulk transport is the subject here, experiment was conducted in the cathode mode, because firstly, the principle in the above qualitative/quantitative treatment is not unique to anode but also applicable to cathode; secondly, there is a large body of data regarding MIEC cathode but almost nothing there for anode part, from which the necessary input parameter is readily available.

An $La_{0.6}Sr_{0.4}Co_{0.2}Fe_{0.8}O_3$ (~1.2 mm)/GDC(~30 μm) bilayer was fabricated through the spray-modified dry pressing method as described in experimental section. The sample was tested in the configuration shown in Fig. 2.10a. In order to avoid the electronic conductivity in GDC, testing was carried out in air instead in anode-H2/cathode-air. To simulate cathode mode on LSCF, positive and negative potential was applied to Pt counter electrode and LSCF, respectively. Constant currents flew through this bilayer. Fig. 2.10b shows the microstructure of the cross-section. The adhesion between GDC/LSCF is good and GDC was successfully densified to ensure no electron current or gas leaking. The goal of this experiment is to see whether a current which is too high to be realized by mere chemical diffusion in LSCF/GDC pellet can be flew through it without damaging the sample, therefore proving the extra contribution from electrical field.

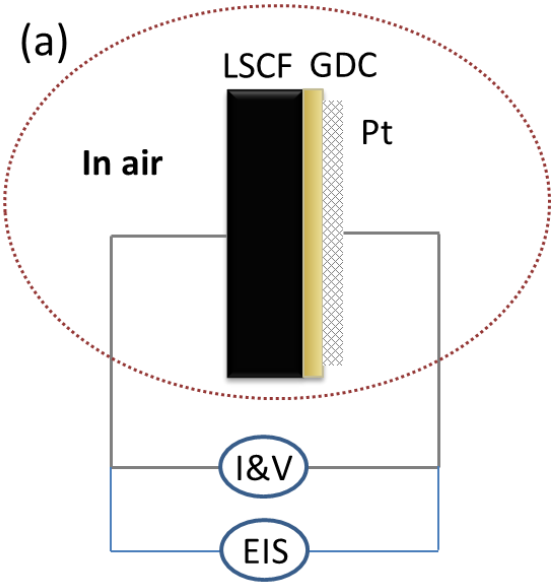

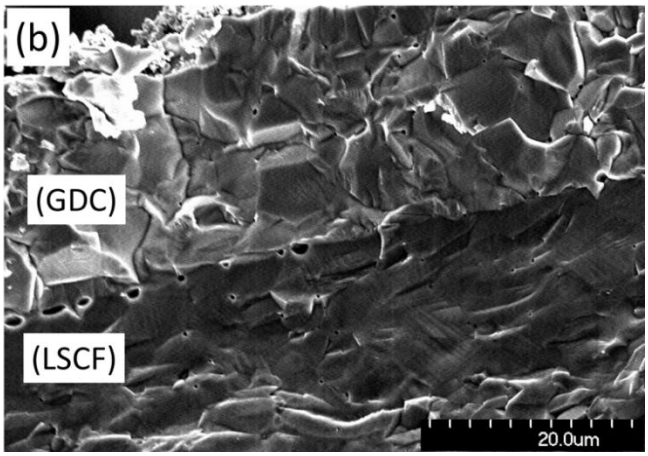

Figure 2. 10 The configuration of LSCF/GDC measurement (a) and cross-sectional LSCF/GDC (d).

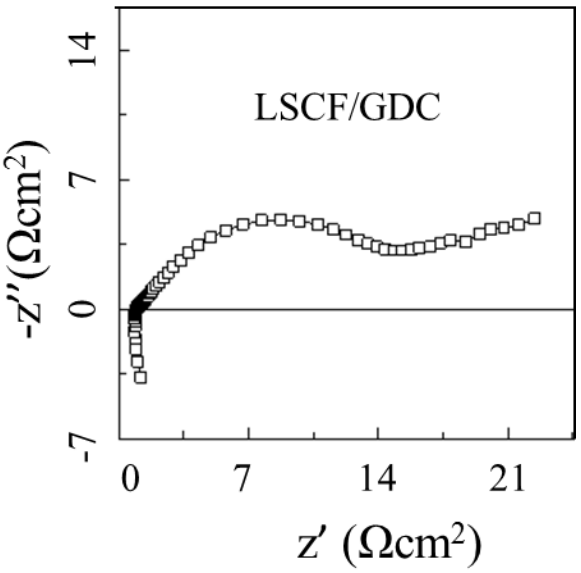

Figure 2. 11 EIS of LSCF/GDC bilayer in air 700oC

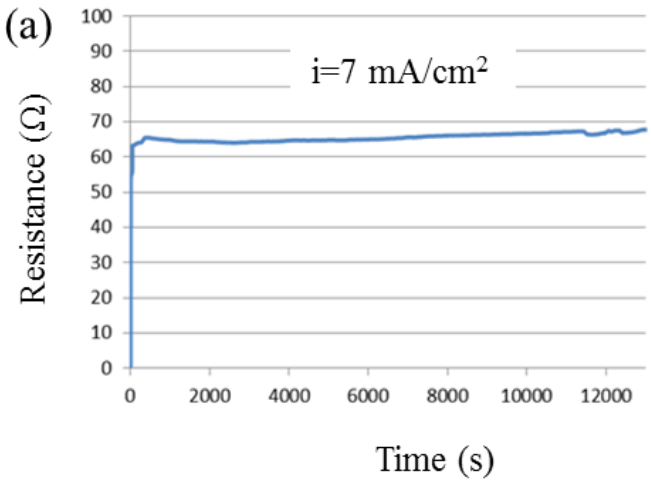

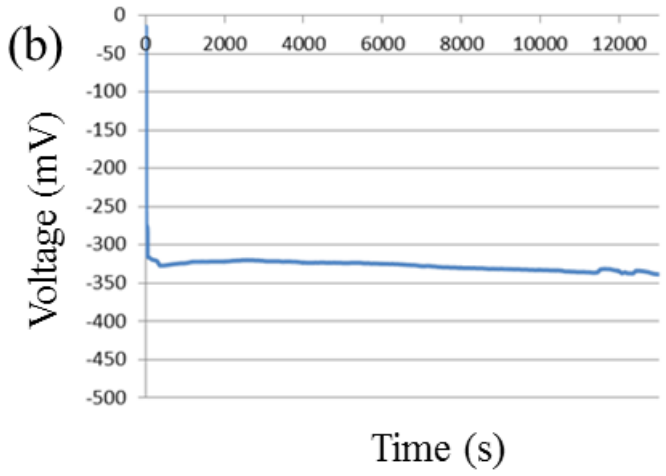

Figure 2. 12 DC resistance under constant current loading for LSCF/GDC bilayers (a), and the variation of applied voltage (b).

Fig. 2.11 shows the EIS of such bilayer measured in air at 700oC. The arc represents the surface reaction, i.e. 14 Ωcm2, and the tail the transport resistance that cannot be known from this spectrum. Fig. 2.12a shows the DC resistance under a constant current loading, 7 mA/cm2, on the sample. The total resistance is ~66 Ω (or 46 Ωcm2), which means 32 Ωcm2 is for oxygen transport. Fig. 2.12b shows voltage vs. time, which clearly demonstrates the stability of this sample under this current. The potential applied to the transport process can be calculated as 226 mV. Based on this condition, the distribution of charge carriers under traditional chemical diffusion only assumption and chemical diffusion/electrical field driving co-control assumption can be resolved.

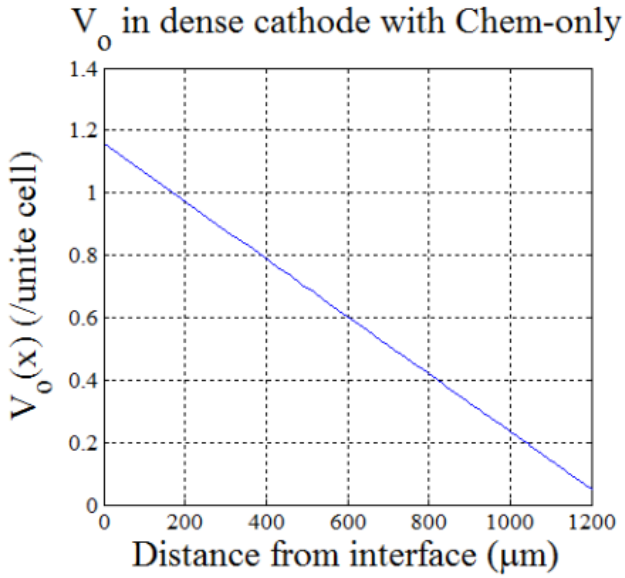

Figure 2. 13 Calculated profiles for $V_O^{\cdot\cdot}$ (b) in LSCF under chemical diffusion only assumption based on the same experimental conditions.

According to literature data, the boundary condition on $V_O^{\cdot\cdot}$ is set to 0.05/unit cell, Dv 2.5×10-6 cm2/s at 700oC. Fig. 2.13 shows the profile of $V_O^{\cdot\cdot}$ under the chemical diffusion only assumption with the same input conditions as in experiment. The vacancy concentration increases linearly from surface to interface. The final concentration near interface is ~1.2/unit cell, which in fact is high enough to give rise to decomposition of LSCF, therefore is not consistent with experiment result. On the other hand, Fig. 2.14 shows the corresponding calculations on those charge carriers and potentials according to the analytic solutions above with the same condition. It can be found that in most of the active length ion migration driven by electrical field instead of chemical diffusion dominates the ion transport as shown in Fig. 2.14d. Due to such contribution, the concentration gradient turns less steep accordingly and yields much smaller vacancy concentration at the interface; therefore avoid the decomposition of LSCF.

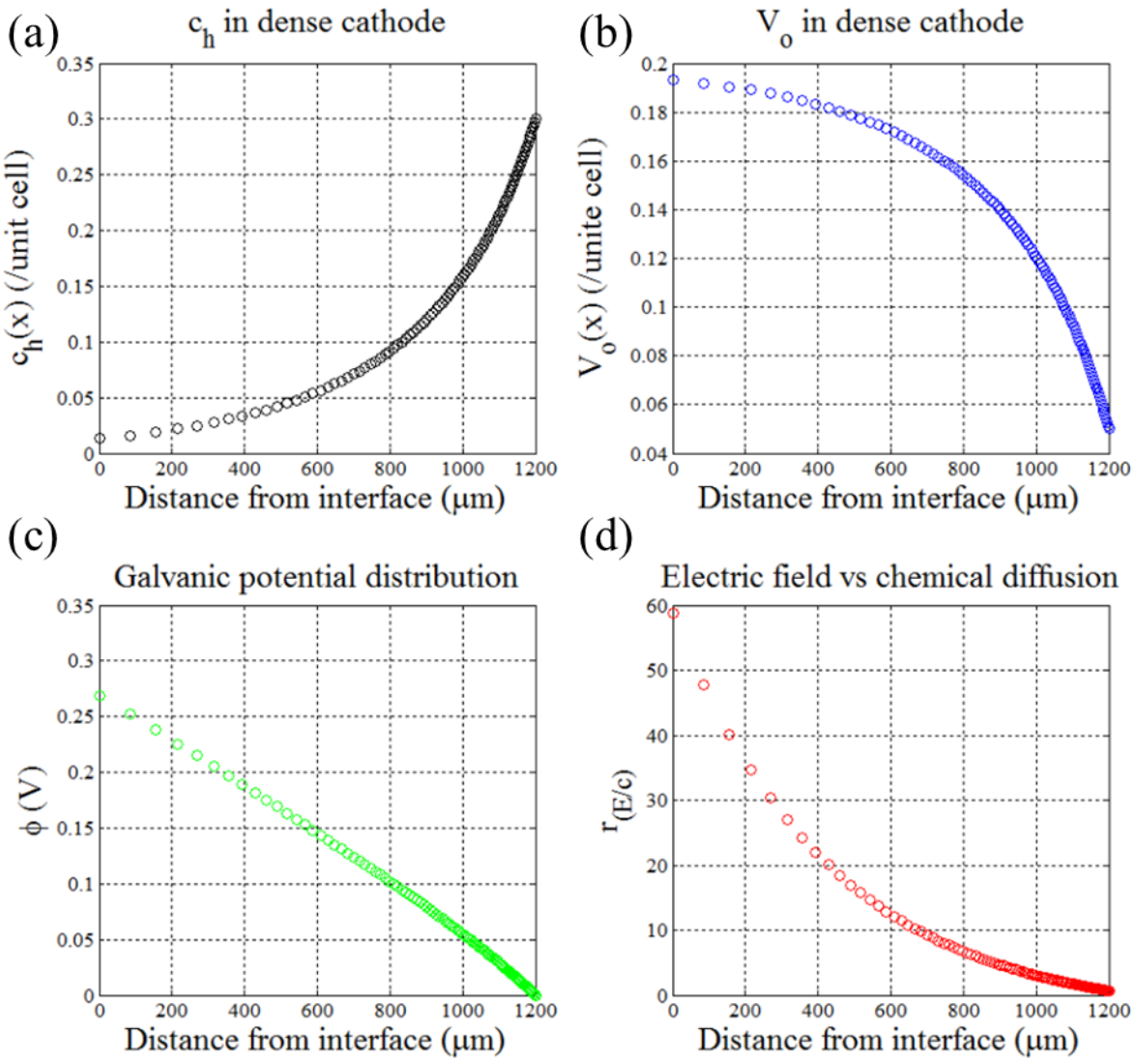

Figure 2. 14 Calculated profiles for ch (a), $V_O^{\cdot\cdot}$ (b), ϕ (c) and rE/C (d) in LSCF based on the experimental conditions.

In the above content, the transport behavior is studied independently by analysis based on sound physical knowledge and by solving the Nernst-Planck-Poisson equations mathematically. Two routes are confirmed to be consistent with each other without sharing common restrictive assumptions, lending credibility to those treatments. However, the role of the first route is more than being used to check the consistency. It shows the basic concept in the MIEC bulk transport that the mathematical treatment is not able to convey. Since the electro-neutrality is adopted in the latter (as also in lots of similar studies), it then becomes superfluous to ask and also impossible to answer whether the MIEC bulk is really electroneutral or in fact locally charged but with electro-neutrality being an appropriate approximation in some cases. Through the first route, it is clearly demonstrated that MIEC bulk under steady state is not neutral but with local charges anywhere, which could be viewed as a complement to the conventional conception on this subject that only chemical diffusion is believed to be true. The validity of analytical solutions for ce, cv and ϕ is further verified through experiment, given without E contribution, either the current flow of 7 mA/cm in the dense LSCF pellets measured here or the constant current load ~0.6 A/cm2 in the practical porous LSCF cathode can be realized. It is unveiled by those results that E contribution is significant in most cases and usually greater than the chemical diffusion.

In the other hand, for local chemical composition, it has been shown by above calculations and can be briefly summarized that the real concentration of ionic defects (vacancy or interstitial oxygen) under service condition in either anode or cathode are less deviated from the as-prepared composition compared to estimated from the Nernst equation using equivalent PO2-stoichiometry data. The schematic diagram is displayed in Fig. 2.15. As a result, the stability of anode material toward the relatively high PO2 in anode/electrolyte interface, or cathode towards the relatively low PO2 in cathode/electrolyte interface is less severe due to the existence of electrical field in the bulk.

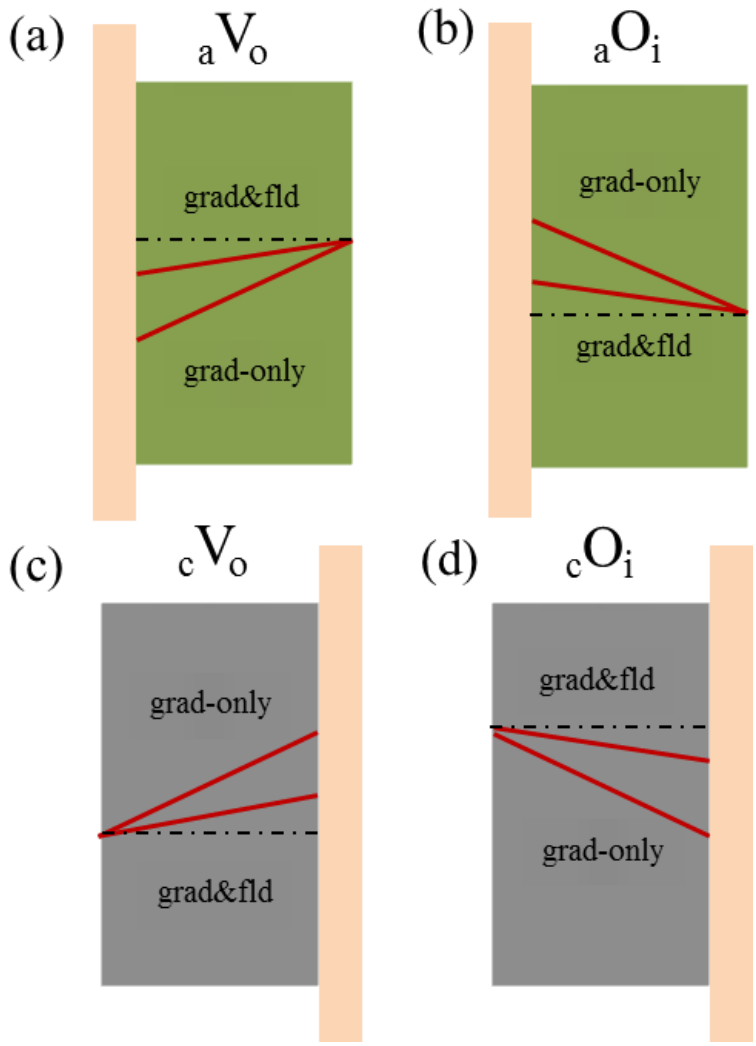

Figure 2. 15 schematic drawing of oxygen defect profiles in anode and cathode, vacancy in anode (a), interstitial oxygen in anode (b), vacancy in cathode (c), interstitial oxygen in cathode (d)

According to the profiles of ϕ in Fig. 2.6-9 representing all types of MIEC materials, it is clear that the electrical fields in both anode and cathode work to facilitate the transport of oxygen defects. However, as shown in Fig. 2.15, only for anode materials with O_i'' and cathode materials with $V_O^{\cdot\cdot}$ defects, the over-potential and then the electrical field will maintain higher ionic conductivities for those materials under polarization relative to equilibrium status, while for the opposite cases, anode materials with $V_O^{\cdot\cdot}$ and cathode materials with O_i'', e.g. YCCC anode and $La_2NiO_{4+\delta}$ cathode, the over-potential will shut down the bulk pathway gradually.

At last, besides the influence on the anion transport, the electrical field introduces a new concept for the cation transport in electrode which has never been appreciated before, for it not only drives the anions but inevitably drives the cations movement in the electrode as well. In fact, the diffusion of cation has been mention as one of the causes for the performance relaxation after different treatments in literature, but no firm theoretical support had been provided. With the framework exhibited here, such process could be well-grounded.

Task 2.2 Fundamental Understanding of Over-potential Effect on Surface Oxygen Exchange Kinetics

In this part, sufficient quantitative information of surface electrode resistance were considered, and get the theoretical resistance obtained from EIS was calculated based on different reaction process. Oxygen intermediates and defect concentration were considered for simulating the theoretical resistance across the cathode surface.

In thin dense electrode, if surface oxygen chemical adsorption and dissociation process was considered as dominant rate limiting step firstly because of higher slope value under different oxygen partial pressure, the cathode reaction on the surface can be expressed as:

$$1/2O_2 + e' + s \rightarrow O_{ad}^- \tag{2.24}$$

Here *s* is the unoccupied site on LSCF surface, and O_{ad}^- is the adsorbed oxygen species. Based on dynamic equilibrium theory, the rates of the forward and backward process of Eq. (2.7) are shown as follows

$$v_{f1} = k_{f1} P_{O_2}^{1/2} \cdot \Gamma \cdot (1 - \theta) \tag{2.25}$$

$$v_{b1} = k_{b1} \Gamma \cdot \theta \tag{2.26}$$

where θ is the fraction of oxygen site coverage, Γ is the density of surface oxygen adsorption site, and the k_{f1} and k_{b1} are the rate constants of forward and backward oxygen adsorption/desorption process, respectively. When the reaction reaches chemical equilibrium under OCV, the net rates of this surface step is zero:

$$k_{f1} P_{O_2}^{1/2} \Gamma \left(1 - \theta^{\Theta}\right) - k_{b1} \Gamma \theta^{\Theta} = 0 \tag{2.27}$$

And oxygen species coverage could be wrote as:

$$\theta^{\Theta} = \frac{K_1^{\Theta} \cdot P_{O_2}^{1/2}}{K_1^{\Theta} \cdot P_{O_2}^{1/2} + 1}$$

$$K_1^{\Theta} = \frac{k_{f1}}{k_{b1}} \tag{2.28}$$

Under electrochemical impedance spectroscopy measurement conditions, a small current or voltage perturbation is applied on electrode, oxygen species coverage can be expressed as:

$$\theta = \frac{K_1^{\Theta} P_{O_2}^{1/2} - \mathrm{j}_{\mathrm{perturbation}} / \left(F \cdot \Gamma \cdot k_{b1}\right)}{K_1^{\Theta} P_{O_2}^{1/2} + 1} \tag{2.29}$$

The voltage variation leaded by current perturbation can be calculated based on surface double charge layer,

$$\mathrm{V}_{bias} = \frac{RT}{F} \cdot \ln \frac{\theta^{\Theta}}{\theta} = \frac{RT}{F} \cdot \ln \frac{\dfrac{K_1^{\Theta} \cdot P_{O_2}^{1/2}}{K_1^{\Theta} \cdot P_{O_2}^{1/2} + 1}}{\dfrac{K_1^{\Theta} \cdot P_{O_2}^{1/2} - j_{perturbation} / \left(F \cdot \Gamma \cdot k_{b1}\right)}{K_1^{\Theta} \cdot P_{O_2}^{1/2} + 1}} \tag{2.30}$$

$$\frac{\partial \mathrm{V}_{bias}}{\partial j_{bias|j_{bias}=0}} = \frac{RT}{F} \cdot \frac{1}{F \cdot k_{b1} \cdot \Gamma} \cdot \frac{1}{K_1^{\Theta} \cdot P_{O_2}^{1/2} - j_{perturbation} / \left(F \cdot \Gamma \cdot k_b\right)} = \frac{RT}{F^2 \cdot k_{f1} \cdot \Gamma \cdot P_{O_2}^{1/2}} \tag{2.31}$$

Under these conditions, the electrode resistance is determined by the rate constant of forward reaction of surface oxygen adsorption and desorption process, the density of surface oxygen adsorption site and PO2. And the electrode resistance is proportional to $P_{O_2}^{1/2}$ under constant temperature.

While, if surface oxygen incorporation process was considered as dominant rate limiting under different oxygen partial pressure, the oxygen flux on the surface can be expressed as:

$$O_{ad}^{-} + e^{'} + \mathrm{V}_{\mathrm{O}}^{\bullet\bullet} \rightarrow O_{\mathrm{O}}^{\times} + s \tag{2.32}$$

where $\mathrm{V}_{\mathrm{O}}^{\bullet\bullet}$ is oxygen vacancy on LSCF surface. The rates of the forward and backward process of Eq. (9) are shown as follows

$$v_{f2} = k_{f2} C_{\mathrm{V}_{\mathrm{O}}^{\bullet\bullet}} \cdot \Gamma \cdot \theta \tag{2.33}$$

$$v_{b2} = k_{b2} \cdot C_{\mathrm{O}_{\mathrm{O}}^{\times}} \cdot \Gamma \cdot \left(1 - \theta\right) \tag{2.34}$$

where $C_{\mathrm{V}_{\mathrm{O}}^{\bullet\bullet}}$ is the concentration of oxygen vacancy and $C_{\mathrm{O}_{\mathrm{O}}^{\times}}$ is the concentration of lattice oxygen on electrode surface which was assumed as constant 1/a in our analysis, and the k_{f2} and k_{b2} are the rate constants of forward and backward process of oxygen incorporation, respectively. When the reaction reaches chemical equilibrium under OCV, the oxygen species coverage could be expressed as:

$$\theta^{\Theta} = \frac{1}{a \cdot K_2^{\Theta} \cdot C_{\mathrm{V}_{\mathrm{O}}^{\bullet\bullet}} + 1}$$

$$K_2^{\Theta} = \frac{k_{f2}}{k_{b2}} \tag{2.35}$$

When the electrode was operated under a small current or voltage perturbation conditions, oxygen species coverage can be expressed as:

$$\theta = \frac{1 + a \cdot j_{perturbation} / \left(F \cdot k_{b2} \cdot \Gamma\right)}{a \cdot K_2^{\Theta} \cdot C_{\mathrm{V}_{\mathrm{O}}^{\bullet\bullet}} + 1} \tag{2.36}$$

If the over-potential is established by adsorbed oxygen species, the voltage variation leaded by current perturbation can be calculated based on surface double charge layer,

$$V_{bias} = \frac{RT}{F} \cdot \ln \frac{\theta^{\Theta}}{\theta} = \frac{RT}{F} \cdot \ln \frac{\dfrac{1}{K_2^{\Theta} \cdot C_{V_O^{\bullet\bullet}}^{\Theta} + 1}}{\dfrac{1 + j_{perturbation} / (F \cdot k_{b2} \cdot \Gamma)}{K_2^{\Theta} \cdot C_{V_O^{\bullet\bullet}}^{\Theta} + 1}} \tag{2.37}$$

$$R_p = \frac{\partial V_{bias}}{\partial j_{bias} | j_{bias}=0} = \frac{RT}{F} \cdot \frac{1}{F \cdot k_{b2} \cdot \Gamma} \tag{2.38}$$

Hence, for the oxygen incorporation process, the electrode resistance is independent on oxygen partial pressure and just determined by the rate constant of backward reaction and the density of surface oxygen adsorption site.

The XRD patterns of mixed LSCF and GDC powders after sintering 1300oC for 4h is shown in Figure 2.16. There is no obvious impurity in the pattern except for LSCF cubic Pm3m peaks and GDC cubic peaks.

The cross-section and surface microstructures of the dense LSCF obtained from a disc of the sintered sample are shown in Figure 2.17. The LSCF surface is composed of a stack of dense single crystals with a diameter of 2- 4μm. The single crystal particles have well defined edges and corners. The cross-section shows that the thickness of the LSCF layer is about in the range of 5-20μm after pre-polishing the LSCF surface with 0.25μm polishing paste to remove the surface oxide. And the good contact between the GDC and LSCF interface was achieved without cracks and delamination.

The electrochemical properties of the LSCF dense electrode were determined by electrochemical impedance spectroscopy (EIS) with Metrohm Auto lab instrument. The AC current output was measured with amplitude potential of 10mV in a frequency range from 106 Hz to 0.01Hz under difference conditions. The impedance spectrograms were analyzed by Z-plot/Z-view software (Z-view 3.0) with a simple equivalent circuit. The different gas compositions were made by air and nitrogen with the total gas flux set to 400ml/min and the bias voltage between the reference electrode and LSCF dense electrode were controlled by constant current source.

The typical AC Impedance spectra were recorded at 700ºC under difference oxygen partial pressures ($2*10^{-4}$-0.21 atm). Fig.18. shows that the electrode resistant exhibits a strong dependence on the oxygen partial pressure. And this behavior, combined with the reported high characteristic length (hundreds of microns) of LSCF, suggests that the surface oxygen reduction reaction is the rate limiting step for the dense LSCF electrode used here with thickness less than 50μm. A sample fitting equivalent circuit R (R_LQ_L) was used to fit those spectra in our impedance analysis. The dependence of electrode resistance on the oxygen partial pressure was shown in Figure 2.19. It was found that the reaction order for this single process is about to 0.39, which indicates that the rate limiting step for the dense LSCF is the chemical adsorption and dissociation process or incorporation of oxygen species process.

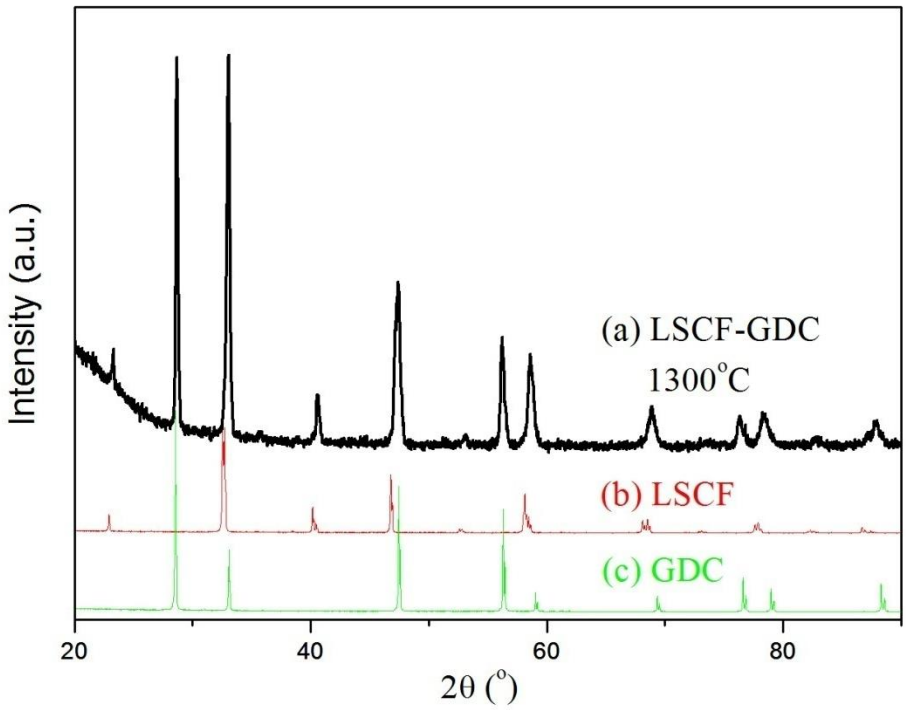

Figure 2. 16 XRD pattern of (a) mixed LSCF & GDC powders, (b) pure LSCF powders and (c) pure GDC powders after sintering at 1300oC for 4h.

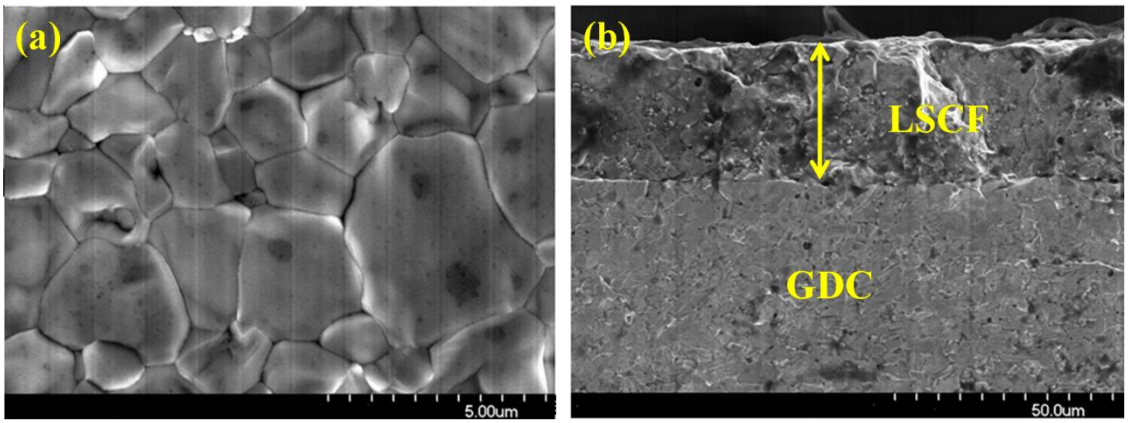

Figure 2. 17 SEM images of (a) surface and (b) cross-section of LSCF/GDC dense samples after sintering 1300oC for 4h.

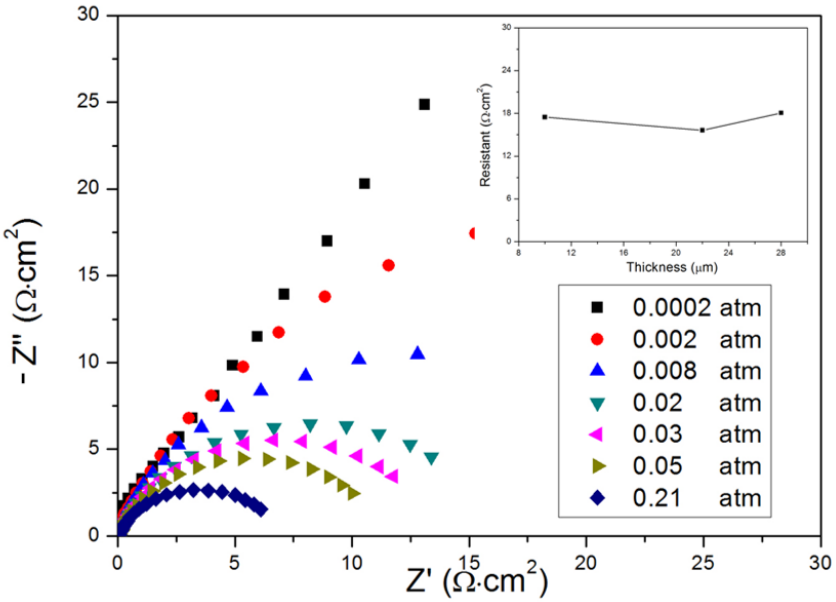

Figure 2. 18 Impedance spectra of dense LSCF electrode under different oxygen partial pressures.

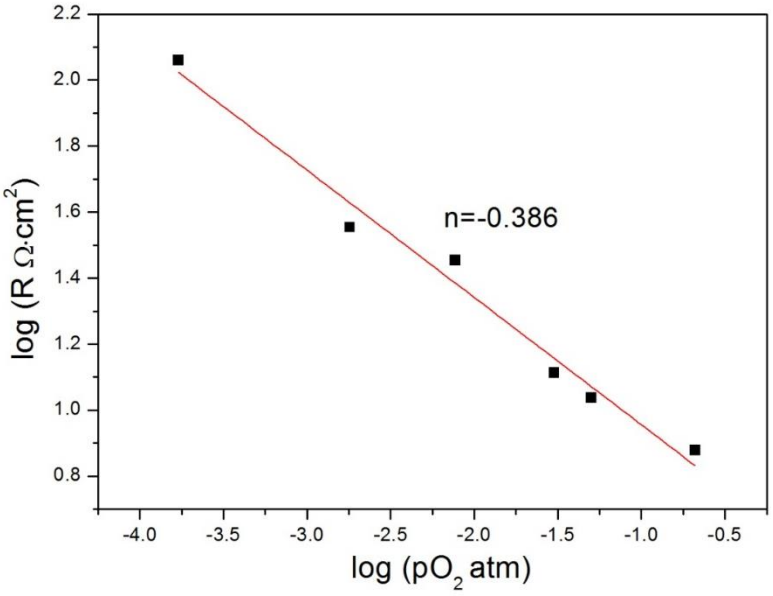

Figure 2. 19 The electrode resistance as a function of oxygen partial pressure at 700oC

To characterize the electrode resistance under polarization, the AC impedance measurement and DC bias voltages were applied on three electrode cells. And the bias voltage applied on LSCF side is estimated from the following equation

$$\eta = E - I \times R_{ohm} \tag{2.39}$$

Where E (V) is the applied voltage between the LSCF cathode and the reference electrode, I (A) is the current flowing through the cell and Rohm (Ωcm2) is the electrolyte resistance measured by the electrochemical impedance spectrum. The voltage consumption from bulk transport is ignored here because although several researchers suggested that the potential in the MIEC electrode was not uniform according to the electric neutrality and immobile cations or oxygen defects distribution was assumed, the Galvani potential drop in dense LSCF bulk was ignored in our analysis based on the verified surface reaction limitation and high ionic and electronic conductivity of the LSCF electrode, In other words, and the bias voltage is just influence the surface work function and the electrode/electrolyte contact potential difference.

Firstly, since the rate constants of forward and backward process are assumed to have an Arrhenius form, they can be expressed as:

$$k_f = \frac{kT}{h} e^{-\Delta \tilde{G}_f / RT} \tag{2.40}$$

$$k_b = \frac{kT}{h} e^{-\Delta \tilde{G}_b / RT} \tag{2.41}$$

Where h is Plank's constant and is the variations of Gibbs free energy for the forward or backward reaction. Hence, when a steady state is obtained under a constant bias voltage, those can be calculated as follows

$$k_{fm}^{\eta} = k_{fm} \exp\left(-\alpha F \eta\right) \tag{2.42}$$

$$k_{bm}^{\eta} = k_{bm} \exp\left((1-\alpha) F \eta\right) \tag{2.43}$$

$$K_m^{\eta} = \frac{k_{fm} \exp\left(-\alpha F \eta\right)}{k_{bm} \exp\left((1-\alpha) F \eta\right)} \tag{2.44}$$

Where α is the transfer coefficient, and the ratio of the rate constants of forward and backward process is expressed as K_m^{η}. Therefore, if the rate limiting step is surface adsorption/desorption process, according to prior calculation, the electrode resistance under applied bias voltages can be calculated as:

$$\mathrm{V}_{bias} = \frac{RT}{F} \cdot \ln \frac{\theta^{\eta}}{\theta^{perturbation}} = \frac{RT}{F} \cdot \ln \frac{K_1^{\eta} \cdot P_{O_2}^{1/2} - j/\left(F \cdot \Gamma \cdot k_b^{\eta}\right)}{K_1^{\eta} \cdot P_{O_2}^{1/2} - \left(j + j_{perturbation}\right)/\left(F \cdot \Gamma \cdot k_b^{\eta}\right)} \tag{2.45}$$

$$R_p = \frac{\partial \mathrm{V}_{bias}}{\partial j_{bias}|_{j_{bias}=0}} = \frac{RT}{F^2 \cdot k_b^{\eta} \cdot \Gamma} \cdot \frac{1}{K_1^{\eta} \cdot P_{O_2}^{1/2} - j/\left(F \cdot \Gamma \cdot k_b^{\eta}\right)}$$

$$= \frac{RT}{F^2 \cdot k_{f1} \cdot \exp\left(-\alpha F \eta\right) \cdot \Gamma \cdot P_{O_2}^{1/2} - j} \tag{2.46}$$

However, if the rate limiting step is oxygen species incorporation process and the applied bias voltage is consumed by adsorbed oxygen species, the voltage variation leaded by current perturbation can be calculated based on surface double charge layer,

$$V_{bias} = \frac{RT}{F} \cdot \ln \frac{\theta^{\eta}}{\theta^{perturbation}} = \frac{RT}{F} \cdot \ln \frac{\dfrac{1 + j/\left(F \cdot \Gamma \cdot k_{b2}^{\eta}\right)}{K_2^{\eta} \cdot C_{V_O^{\bullet\bullet}}^{\eta} + 1}}{\dfrac{1 + \left(j_{perturbation} + j\right)/\left(F \cdot \Gamma \cdot k_{b2}^{\eta}\right)}{K_2^{\eta} \cdot C_{V_O^{\bullet\bullet}}^{\eta} + 1}} \tag{2.47}$$

$$R_p = \frac{\partial V_{bias}}{\partial j_{bias|j_{bias}=0}} = \frac{RT}{F} \cdot \frac{1}{F \cdot k_{b2} \cdot \exp\left((1-\alpha)F\eta\right) \cdot \Gamma + j} \tag{2.48}$$

Based on the total cathode reaction Eq (2.49) and the basic Nernst equation Eq(2.50), the relationship between thermos-dynamical driving force and electrochemical driving force can be established. It was assumed that the activity of the oxygen species involved in cathode reaction can be approximated as the oxygen concentration C(x) and because of the strong stability of YSZ electrolyte in the appropriate range of bias voltage or the variation of oxygen partial pressure, the electrochemical potential of oxygen vacancy in the electrolyte keeps constant in a large range. The precise corresponding values are listed in Table 2.1.

$$V_{O,YSZ}^{\bullet\bullet} + 1/2O_2 + 2e' \rightarrow + O_{O,YSZ}^{\times} \tag{2.49}$$

$$E = E^{\Theta} + \frac{RT}{4F} \ln\left(\frac{P_{O_2}}{P_{O_2}^{\Theta}}\right) \tag{2.50}$$

When cathodic polarization was applied on the cells, the oxygen species coverage on the surface of electrodes, which similar to increase of oxygen partial pressure, is lower than that under matching oxygen partial pressure according to the Nernst equation because of the positive current, which affects the surface double layer structure and then increases the calculated polarization resistance. While, under anodic polarization, the phenomenon of surface oxygen coverage is in reverse since current j becomes negative. The oxygen species coverage on the surface of electrodes, which similar to increase of oxygen partial pressure, is lower than that under matching oxygen partial pressure according to the Nernst equation. It results in lower polarization resistance than that of samples under matching oxygen partial pressure. Figure 2.20 shows the electrode resistance as a function of bias voltage. With the enhancement of the electrochemical driving force for the cathode reaction, the larger surface oxygen exchange coefficient was obtained, which the effects of the chemical driving force. As a comparison, the corresponding values depending on the oxygen partial pressure was are plotted in the diagram as well. Comparing with the effect of thermos-dynamical chemical driving force it can be seen that in the cathodic polarization part the function of electrochemical driving force has slowed. And instead, in the anodic polarization part the chemical driving force has much less effect on the cathode reaction than that of electrochemical one active. The distinction becomes larger with increasing the bias voltage. Following the above phenomena, the quantitative analysis of electrode resistance under bias voltage was modeled and calculated based on different reaction process.

Therefore, the uncoordinated relationship on polarization resistance values was obtained between oxygen partial pressure and bias voltage based on the Nernst equation, where the slope for the variation of bias voltage is lower than that for the variation of oxygen partial pressure. But since the comparison of resistance Even though it can reflect the trend between thermo-dynamical and electrochemical force, it can't quantitative characterize the Nernst equation between thermo-dynamical and electrochemical force. The operating full cell should be monitored under different

oxygen partial pressure and bias voltage, in which variation of the current density can reflect accurately whether the relationship of thermos-dynamical with electrochemical force obey the Nernst equation or not. It will be proved in our future research.

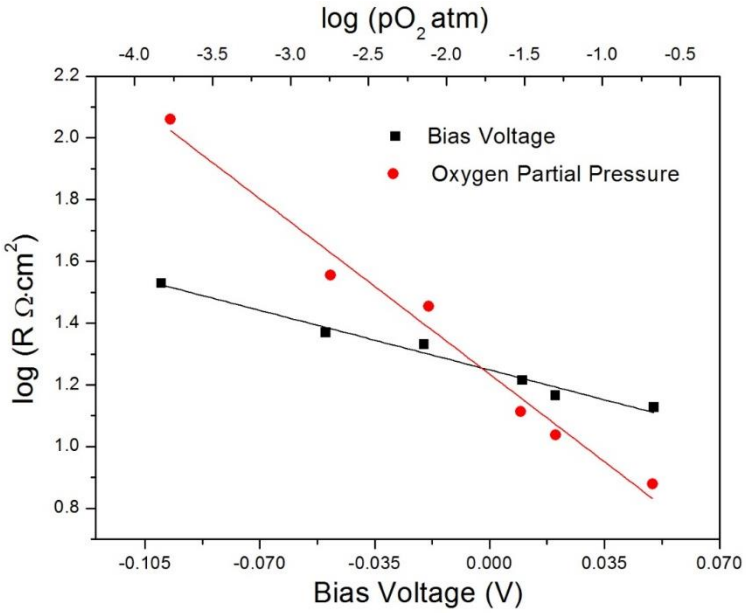

Figure 2. 20 The calculated electrode resistance as a function of bias voltage and oxygen partial pressure

Table 2. 1 The calculated electrode resistance as a function of bias voltage and oxygen partial pressure

	Cathodic polarization			Anodic polarization		
Bias (V)	0.01	0.02	0.05	0.02	0.05	0.1
PO_2 (atm)	0.03	0.05	0.21	0.008	0.002	0.0002

Task 3: Electrochemical Modeling on ORR kinetics of Hetero-structured Cathode Surface

Task 3.1 the Role of O_i'' in the Incorporation Reaction of Hetero-structured Cathode surface with R-P phase

A similar trend between D and k in perovskites has been reported. After collecting a number of results from independent sources, Kilner et al. derived an expression for *k* in terms of bulk atomistic parameters. Conceptually, the surface exchange reaction includes all subsequent steps until the mass transfer finishes in the gas/solid interface, which is different from the bulk transport that occurs in a single phase. The sole factor involved into both processes is $V_o^{\cdot\cdot}$. Therefore by assuming $V_o^{\cdot\cdot}$ to act a major role in the surface exchange process, the relationship between D and k was established in perovskites. Likewise, it appears rightful for one to explain the *D & k* correlation in LSNO by similarly stressingO_i''. But comparing the defects in perovskites and R-P phase, an immediate question coming up is how two opposite species, $V_O^{\cdot\cdot}$ andO_i'', can play similar

roles in the incorporation process, because only vacancies regardless in lattice or in interstice are the active sites in such reaction. In the following, a relationship between k and $O_i''$is proposed, by which the seemingly contrary roles of $V_O^{\cdot\cdot}$ in perovskite and O_i'' in R-P structure could be harmonized in principle.

The surface exchange process is carried out in several sequent steps as shown above. The reaction orders are calculated using the routine reported elsewhere and listed after each elementary reaction. Oxygen surface exchange: $O_2 \rightarrow 2O_{ads} \xrightarrow{e} O_{ads}^- \xrightarrow{e,V_i^\times} O_i''$

Step 1	$O_2 \leftrightarrow 2O_{ads}$	n=1	(3.1)
Step 2	$O_{ads} + e \leftrightarrow O_{ads}^-$	n=3/8	(3.2)
Step 3	$O_{ads}^- + e + V_i^\times \leftrightarrow O_i''$	n=1/8	(3.3)
Step 3'	$O_{ads}^- + e + V_o^{\cdot\cdot} \leftrightarrow O_o^\times$	n=1/8	(3.4)

For those specimens with apparent excessive oxygen such as LNO and Sr10, interstitial vacancy in LaO layer instead of oxygen vacancy in ABO_3 layer is taken as the primary active species, as shown in step 3. Since the amount of excessive oxygen decreases with Sr doping, for the end members with little oxygen hyper-stoichiometry like Sr40, oxygen vacancies in perovskite layer might also come to play as active sites. Therefore, besides through interstitial insertion, the incorporation step can proceed via the lattice oxygen vacancies as shown in step 3' as well. Within the law of mass action, the reaction rate for oxygen incorporation process is,

$$r_3 = k_3[O_{ads}^-][V_i^\times]\exp\left(-\frac{\Delta E_{2PB}F}{2RT}\right) - k_3^-[O_i'']\exp\left(\frac{\Delta E_{2PB}F}{2RT}\right) \tag{3.5}$$

where $k_i$and $k_i^-$are the rate constants for the forward and backward reaction, [X] the activity of X species.

Assuming incorporation steps as the RDS, at equilibrium, there is no net oxygen flux across the surface/electrode and the 2PB over-potential is zero. The exchange oxygen ion flux density of step 3, j_3^0, is

$$j_3^0 = k_3[O_{ads}^-][V_i^\times] = k_3^-[O_i''] \tag{3.6}$$

At this moment, a false proportional dependency between j_3^0 and $[O_i'']$is about tobe drawn if focusing on $k_3^-[O_i'']$ only, because the opposite can be arrived if instead considering the second term$k_3[O_{ads}^-][V_i^\times]$. The cause of such discrepancy lies in the unique feature of this reaction: site conservation.

Interstitial site conservation in R-P phase gives

$$[O_i''] + [V_i^\times] = C \tag{3.7}$$

where C is a constant. Inserting Eq. 3.6 into Eq. 3.7 gives

$$K_3 = \frac{k_3}{k_3^-} = \frac{1}{[O_{ads}^-]\left(\frac{C}{[O_i'']}-1\right)} \tag{3.8}$$

Where K_3 is the equilibrium constant of incorporation step. It is found that *K*3 will increase with $[O_i'']$ provided $[O_{ads}^-]$ is not directly dependent on$[O_i'']$, meaning $k_3$may increase and/or k_3^-may decrease as $[O_i'']$ rises.

Combining Eq. 3.6 and 3.7 to eliminate $[O_i'']$ and $[V_i^\times]$, one obtains

$$j_3^0 = \frac{C}{\frac{1}{k_3[O_{ads}^-]}+\frac{1}{k_3^-}} \tag{3.9}$$

By appropriately setting the evolution of k_3 and k_3^-towards $[O_i'']$, a non-monotonic relationship between $[O_i'']$ and j_3^0 can be established. A possible scenario is qualitatively illustrated in Fig. 3.1. In this diagram, k_3 increases and k_3^- decreases with $[O_i'']$ according to the dependency of K3 on $[O_i'']$ in Eq. 3.8. Within $[O_i'']$ poor region, k_3 is set to change more drastically than k_3^-; in the $[V_i^\times]$ poor region, the opposite is valid. Due to the different gradients for k_3 and k_3^- vs.$[O_i'']$, j_3^0 reaches its maximum at a certain $[O_i'']$ value according to Eq. 3.9. Over that point, going forward to increase $[O_i'']$ or backward to increase $[V_i^\times]$ will lead to decrease in j_3^0.

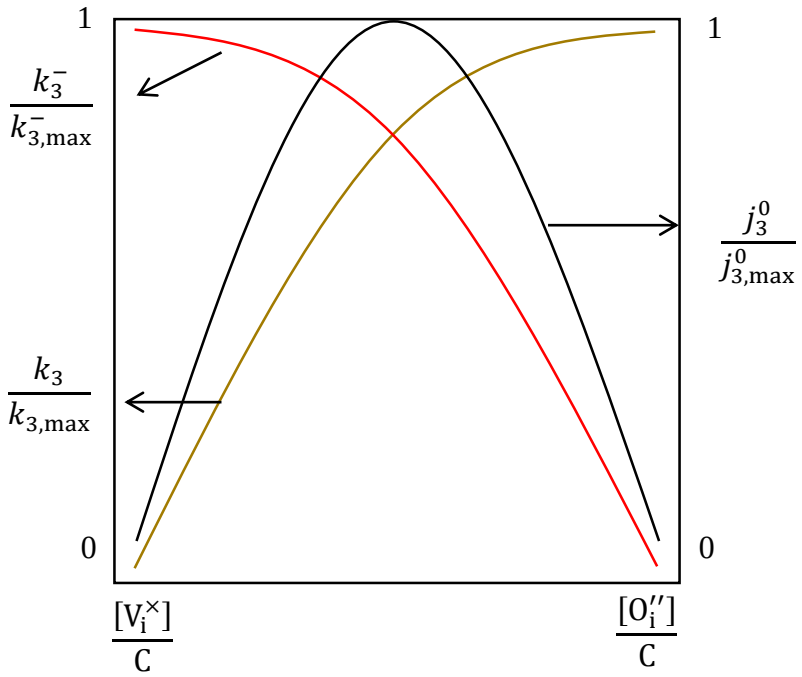

Figure 3. 1 Evolution of k_3 and k_3^-, and the resultant j_3^0 with $[O_i'']$.

It seems that the constant C in Eq.3.7 should be determined under the charge neutrality corresponding to Ni oxidation status (C=0.25 at Ni^{3+}). However, as the interstitial vacancies in La_2O_2 layer are equivalent in the incorporation reaction and each site has the same chance to accommodate an adsorbed oxygen ion, it makes more sense to take C as the maximum interstitial sites in the rock salt layer, that is, 2 per unit cell. The reported δ values for LSNO in

cathode condition are about 0.15 and turn fewer after Sr doping, which belongs to the $[O_i'']$ poor region. In this case, increasing $[O_i'']$ results in enlarged j_3^0. Likewise, a similar diagram can be built for perovskites, except C being 3 per unit cell. The reported $[V_O^{\cdot\cdot}]$ for the perovskites seldom exceeds 0.5, which probably belongs to $[V_O^{\cdot\cdot}]$ poor region. As a result, increasing $[V_O^{\cdot\cdot}]$ will increase the exchange rate of incorporation reaction in perovskites. By this fashion, the contradiction mentioned before could be resolved.

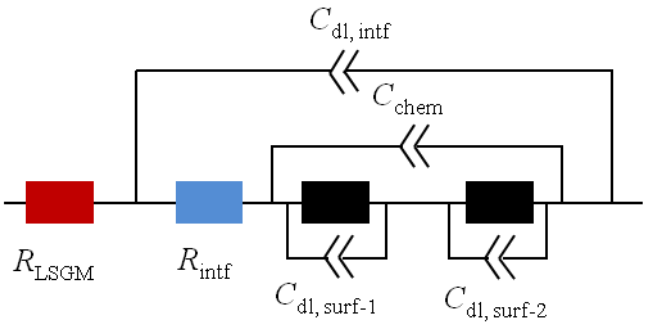

Figure 3. 2 Equivalent circuit for LSNO with two subsequent surface processes.

Some analysis can be conducted to the check the possibility of the scenario in Fig. 3.2. The feasibility of building such parabolic profile for j_3^0relies on the variability of K3, then k_3 and k_3^-. For normal chemical reactions where the initial concentrations of reactants/products are independent of each other, the equilibrium constants can really be constant, and certainly the reaction rate constants are related to Ea, temperature ($k_i \propto \exp(\frac{-E_a}{RT})$) only, other than to the concentrations of reactants/products. But because of the site conservation in defect chemistry which puts an extra restriction on step 3, the development of equilibrium is hence partially influenced by Eq.3.6 which, when combined with Eq.3.5, leads to Eq.3.7, indicating that K3 could alter with $[O_i'']$ .This observation has been favored by the changeable Ea for $[O_i'']$formation depending on the oxygen stoichiometry of the R-P phase materials.

As reported, the uptake of O_i'' is an exothermic process, $E_{\mathrm{a,forward}} < E_{\mathrm{a,backward}}$, which consequently lead to a judgment that $E_{\mathrm{a,forward}}$ decreases, and $E_{\mathrm{a,backward}}$increases with$[O_i'']$if the trends of k_3 and k_3^- vs. $[O_i'']$ in Fig. 3.2 is valid. It in turn gives rise to the prediction that the formation enthalpy for $[O_i'']$decreases (more negative) with increasing$[O_i'']$, and vice versa. The supportive evidences about this prediction can actually be found. Firstly, an increased enthalpy with Sr doping is implied by the phenomenon that $[O_i'']$ in LSNO decreases as Sr, which corresponds to a weakened driving force for the formation of O_i'' as Sr doping. Secondly, the partial molar enthalpy of O_i'' formation in LSNO have been calculated by Nakamura et al, and such value is found to enlarge with increasing Sr (less O_i'') in the whole oxygen hyper-stoichiometry region, enabling the possibility that at a fixed PO2the formation enthalpy increases with Sr doping. Nevertheless, it is particularly notable that the enthalpy tendency towards $[O_i'']$ triggered by Sr doping in LSNO might be not applicable to the change induced by PO2variation, because $[O_{\mathrm{ads}}^-]$in Eq. 3.3 is assumed to be constant upon $[O_i'']$ change, which in fact is explicitly dependent onPO2.

In above deviation, the activity of electron is left out assuming it is sufficient in all LSNO samples. $[O_{\mathrm{ads}}^-]$is taken as a fixed value which probably varies more or less at different Sr contents. In addition, the deviation is mathematically qualitative. However, in spite of all these assumptions,

such model is a meaningful try to exploit the role of O_i'' in surface exchange kinetics for the R-P phase structure materials.

Task 4: Development of the Hetero-structured Cathode

Task 4.1 Basic Development of Doped $La_2NiO_{4+\delta}$-based Materials with R-P phase

To clarify the effect of Sr doping on the electrode performance of LNO cathode, or more specifically, how it affects the bulk diffusion and surface exchange kinetics in the cathode ORR, LSNO cathode are characterized by EIS in different PO2 in temperature range of 600~800ºC.

Figure 4.1 shows the electrical conductivities of $La_{2-x}Sr_xNiO_{4+\delta}$. Sr doping enhanced the conductivity regardless of the doping level. The highest one is achieved with Sr10. But with heavier doping, the conductivity decreases gradually, which is different from the results reported by Nakamura that the conductivity increased with Sr content. Although sintered at 1450ºC, the pellets are still not completely dense. The relative density is determined by Archimedes method: 95.7% for LNO, 94.2% for Sr10, 93.6% for Sr20, 92.7% for Sr30, 91.9% for Sr40. Therefore, the difference shown in this work should be partially from the relative density. From 600 to 800oC, the conductivity decreases with temperature, which is more significant for LNO, Sr10 and Sr20 compared to Sr30 and Sr40. It primarily results from the reduction of electron hole density, accompanying by the decrease of δ as temperature increases.

Fig. 4.2 shows the EIS profiles for those samples measured in air at 700oC. The spectra were analyzed based on the impedance model introduced by Adler et al. The ohmic resistances have been subtracted. The spectrum for LNO features half tear shape, showing a 45o straight line at high frequency (HF) and a semi-circle in the low frequency (LF) domain. Straight line at HF limit as such is a prominent indicator of diffusion limitation. And the half tear-shaped spectrum is usually assigned to the Gerischer impedance depicting a situation controlled by a chemical reaction and the subsequent mass diffusion.

The measured polarization resistances (Rp) and fitting results for all samples at 700oC are tabulated in Table 4.1. The best performance is obtained with the undoped LNO sample, which reads 0.41 Ωcm2 and is a competitive output for the intermediate temperature cathodes at 700oC. The polarization resistance increases with doping level. According to the fitting results, the small capacitances and the large characteristic frequencies for the HF arcs of Sr30 and Sr40 indicate that those arcs can be reasonably associated to a charge transfer process. The incorporation of oxygen into cathode lattice has been taken into account in the ALS element. Meanwhile, the electron transfer from current collector to the cathode must not be the case because Sr30 and Sr40 possess higher electrical conductivities than LNO. In fact, a similar situation has been found on the LSCF electrode: a small HF arc was observed when replacing GDC with the less conductive electrolyte YSZ, and attributed to the slowed oxygen exchange rate between LSCF and YSZ. Such arcs herein are therefore assigned to the oxygen ion transfer process between lanthanum nickelates/GDC. The occurrence of such arcs should be determined by the transfer rate in the interface and attributed to the decrease of oxygen diffusivity of the Sr doped cathodes, since GDC barrier layer is the same in each sample from LNO to Sr40.

Table 4. 1 Summary of resistances, capacitances, characteristic frequencies from ALS fitting.

T=700oC	R_p(Ωcm^2)	O2- transfer nickelates/GDC			chem process		
		R_{IT}(Ωcm2)	C (mF/cm2)	(Hz)	R_{chem}(Ωcm^2)	C_{chem}(mF/cm^2)	α
LNO	0.41	-	-	-	0.41	14.1	0.96
Sr10	0.61	-	-	-	0.61	15.9	0.90
Sr20	1.74	-	-	-	1.74	2.1	0.80
Sr30	8.1	0.83	0.011	13000	7.3	0.20	0.90
Sr40	14.4	1.92	0.091	5400	12.5	0.15	0.88

Figure 4.3 indicates the electrical conductivities of as-prepared A-site deficient LNO as the measured temperature (250-800ºC). It can be seen that the temperature-dependent conductivities of all powders have the similar trend, namely the conductivity initially increases and then decreases as temperature. But the conductivity transition temperature of $La_{2-x}NiO_{4+\delta}$ increases with increasing the concentration of deficient lanthanum, and the conductivities of A-site deficient LNO are more stable than LNO materials under low temperature, both of which are beneficial to the application at low-temperature for A-site deficient LNO as cathode materials. The $La_{2-x}NiO_{4+\delta}$ with higher deficient exhibits the slightly higher conductivity below 800ºC. The maximum conductivities of $La_{1.85}NiO_{4+\delta}$, $La_{1.95}NiO_{4+\delta}$ and $La_2NiO_{4+\delta}$ are 105, 100 and 97 Scm^{-1}, respectively. Focusing on lanthanum deficient in LNO, the charge compensation mechanisms can be represented by two defect equations involving either oxygen vacancy or hole formation. The positive holes are treated in localized terms as Ni^{3+} and O^- small polaron species to form Ni-O-Ni transport way of electrons, which could increase p-type conductivity and promote overall reactivity of the catalyst material. The enhanced conductivity shows that part of lanthanum deficient was compensated by holes and increase the concentration of Ni^{3+}-O-Ni^{2+} transport way. But based on the slight rate of increase, the larger oxygen vacancy concentration for high deficient $La_{2-x}NiO_{4+\delta}$ was speculated.

Representative EIS data for symmetric cells using $La_{2-x}NiO_{4+\delta}$ (x=0-0.2) cathodes collected at OCV in air at temperature of 750ºC, respectively, are shown in Fig. 4.4. Typical equivalent circuits $R_s(R_{HF}Q_{HF})(R_{LF}Q_{LF})$ have been used to deconvolute the measured data for the cathodes, where R_s is the ohmic resistance of the symmetrical cells, and R_n and Q_n indicate resistance and constant phase element of different electrode processes, respectively. In the all case of $La_{2-x}NiO_{4+\delta}$ (x=0-0.2) cathodes, two RQ elements of semi-circle arcs reflect the electrode polarization. A equivalent capacitance value CHF($C_n = (R_n Q_n)^{1/n} / R$) in the range of 10^{-4}-10^{-3} F·cm^{-2} are obtained from high frequency response and corresponding to C_{LF} value of $\sim 10^{-2}$ F·cm^{-2}, both of which is typically attributed to charge transfer process and an intermediate behavior with a similar surface process. Such equivalent circuit model can well resolve the impedance plots of the symmetric cells using different cathodes. The R_p values of $La_{2-x}NiO_{4+\delta}$ (x=0-0.2) cathodes are 0.37, 0.42, 0.8 and 1.18 Ω·cm^2 at 750 °C, respectively. The obvious increase in cathode polarization resistance demonstrates that lanthanum deficient decreases the electrochemical activity and surface exchange kinetics of LNO electrodes. The actual polarization resistance of

SOFC cathode (R_p) can thereby be deduced from electrode area and half sum of R_n values (symmetric cell).Temperature-dependent polarization resistance is characterized in Figure 4.5. At 550^{o}C, an additional arc shows in A-site deficient LNO cathode as shown in 4.6. Considering the difference of oxygen ionic conductivity for electrolyte and $La_{2-x}NiO_{4+\delta}$ (x=0-0.2) materials, the additional arc is proposed the interface charge transfer between electrode and electrolyte. At low temperature, the oxygen ionic conductivity of $La_{2-x}NiO_{4+\delta}$ (x=0-0.2) is much higher than electrolyte, and oxygen ions will accumulate at the electrode/electrolyte interface leading to the interface capacitance formation. It indicates that the $La_{2-x}NiO_{4+\delta}$ with higher deficient exhibits rapid bulk oxygen transport properties. Comparing the Nyquist plots 750^{o}C to 550^{o}C, the high frequency arcs have larger variation for $La_{2-x}NiO_{4+\delta}$ (x=0-0.2) cathodes than that of low frequency arcs, as shown in Figure 4.7 and 4.8. Although the $La_{2-x}NiO_{4+\delta}$ with higher deficient have higher conductivity and rapid bulk oxygen transport properties, the surface charge transfer still gradually dominates the impedance with lanthanum deficient increasing. It indicates that surface charge transfer process for LNO materials is possibly controlled by surface interstitial oxygen concentration along with transition metal states.

From previous work we already knew, for R-P phase materials, the interstitial oxygen are more active than vacancy in ABO3 layer in terms of incorporation, and Ni is the main active site for oxygen adsorption process. Combining these two key results we choose Mn substitution Ni into the lattice of R-P phase to enhance the surface kinetics. Mn has strong ability of adsorbing oxygen which is already verified from the good k in LSM. On the other hand, Mn presents high state in R-P phase, which will be expected to produce the big amount of the interstitial oxygen.

Mn is found to substantially promote the surface kinetics, showing highest k of 1.57×10-6 cm/s at 700oC on La1.8Sr0.2Ni0.9Mn0.1O4+δ. Such value is ~80% larger than that of the undoped sample, and is one of the highest k among the currently available R-P phase intermediate temperature cathode.

Figure 4.9 shows the EIS arcs measured from LSNM symmetrical cells. To accurately assess the surface kinetics of cathode materials, dense thin layer has been widely adopted in literature in order to avoid bulk diffusion influence and complex microstructure in the standard porous electrode. An equivalent circuit for the dense electrode under surface exchange dominant situation has been derived elsewhere. The combination of the Cchem originated from oxygen stoichiometry change upon potential perturbation and the Rsurf is responsible for the main arc. Sr15Mn5 was fitted by this EC satisfactorily. The rest samples share the similar profile due to the same surface-dominant situation and were fitted into this EC also to yield R_{surf}.

The equivalent surface exchange coefficient can be calculated from R_{surf} through Eq. 5-1,

$$k = \frac{RT}{4F^2 R_{\mathrm{surf}} c_{\mathrm{o}}} \tag{4.1}$$

where F is the Faraday's constant, co the oxygen concentration in LSNM, R and T keep the usual physical meanings.

Figure 4.10 displays the k values for LSNM. The exchange rate ranks as Sr20Mn10>LNO>Sr15Mn7>Sr15Mn5>Sr40Mn20>Sr60Mn30. k for Sr20Mn10 is about twice bigger than that of the pristine LNO. The highest value is achieved by this modestly doped sample; increasing or decreasing Mn content further will lower the surface kinetics. To assess the real effect of Mn on this trend, both Sr and Mn need to be taken into account in such evolution of k. As stated before, although Mn is the designed substitute for Ni, Sr has to be used to obtain single phase structure. It has been demonstrated in previous studies that Sr doping impairs the surface

kinetics of LNO by increasing the oxidation state of Ni and reducing interstitial oxygen population. Thus, the improvement from Mn doping could be partially offset by Sr.

Due to this very concern, Sr15Mn5 sample was prepared. Comparing Sr15Mn5 and Sr15Mn7, with fixed Sr level, k is increased from 3.7×10-7 to 6.9×10-7 cm/s at 700oC by the extra 2.5% Mn content, which ambiguously proves the advantageous effect of Mn. On the other hand, Daroukh et al. found that full Mn B site La0.5Sr1.5MnO4 tends to keep the exact stoichiometry in a wide range of PO2 with strong reluctance to either accommodate interstitial oxygen or lose lattice oxygen to form vacancy. As the interstitial oxygen is crucial to the ion incorporation, high Mn content will probably lead to decreased exchange rate when limited by the incorporation process. As a result, the optimum Mn content should be the one balancing the rate limits from surface adsorption and ionic incorporation. The apparent activation energy is derived based on this Arrhenius plot. It is reduced gradually in those Mn $\geq$ 10samples compared to LNO, indicating an energetically more favorable surface process with Mn presence.

Table 5-1 summarizes some of the most commonly used R-P phase cathodes. Sr20Mn10 from this work displays one of the best k values, 1.57×10-6cm/s at 700oC, which is much better than its Co or Fe doped counterpart, demonstrating the substantial advantage of Mn over other dopants. At last, since the Sr/Mn=2 ratio was empirically chosen, higher surface performance can be reasonably expected through systematical study on the Sr content in the future.

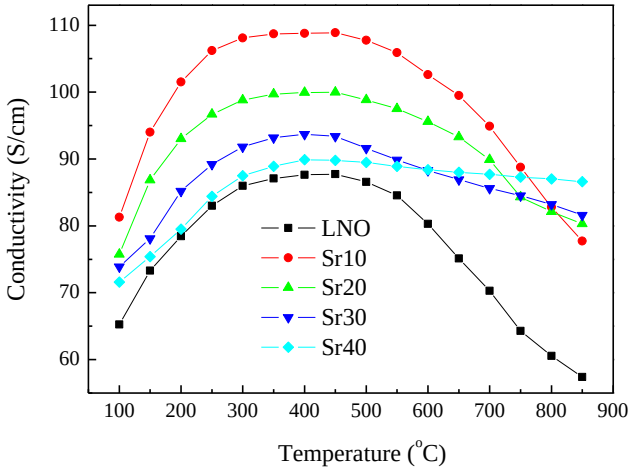

Figure 4. 1 Electrical conductivities for La2-xSrxNiO4+δ tested in air.

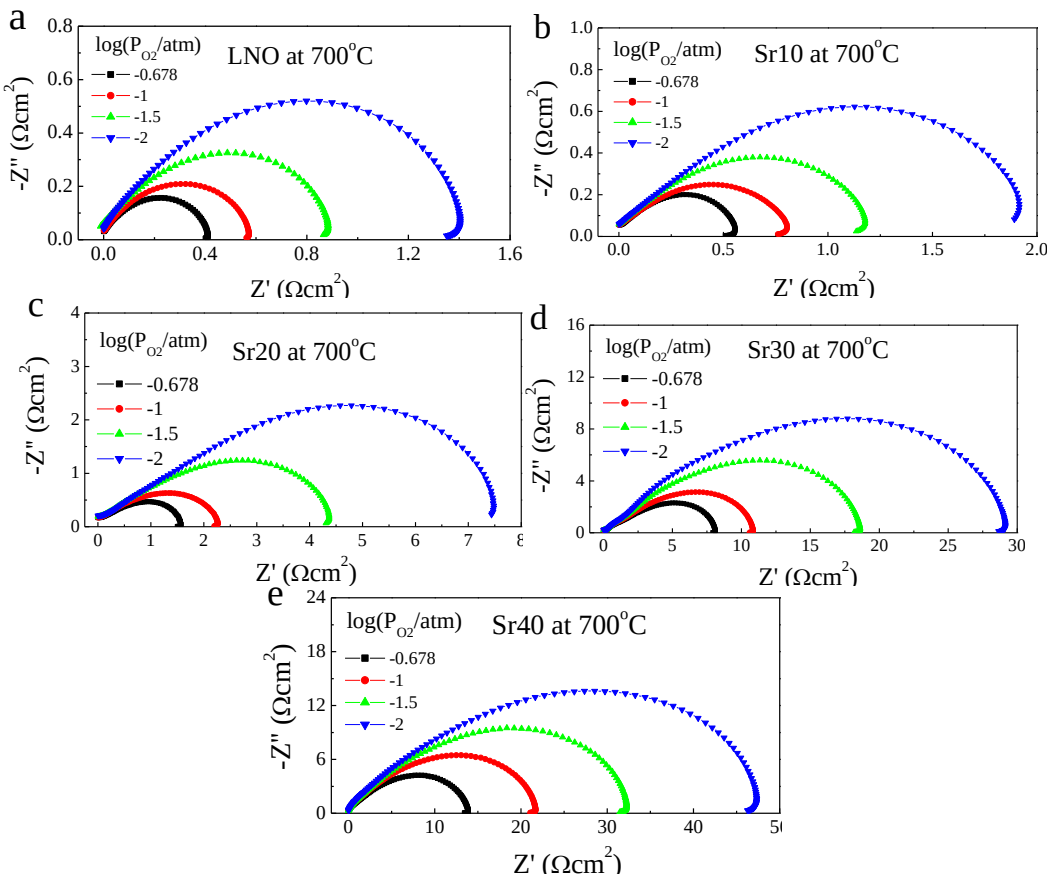

Figure 4. 2 EIS spectra for different Nickelates at 700oC in various PO2.

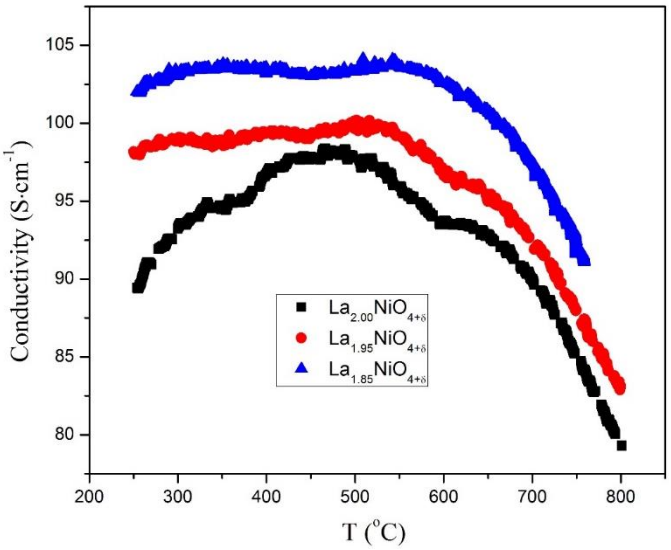

Figure 4. 3 The total conductivity of La2-xNiO4+δ pellets.

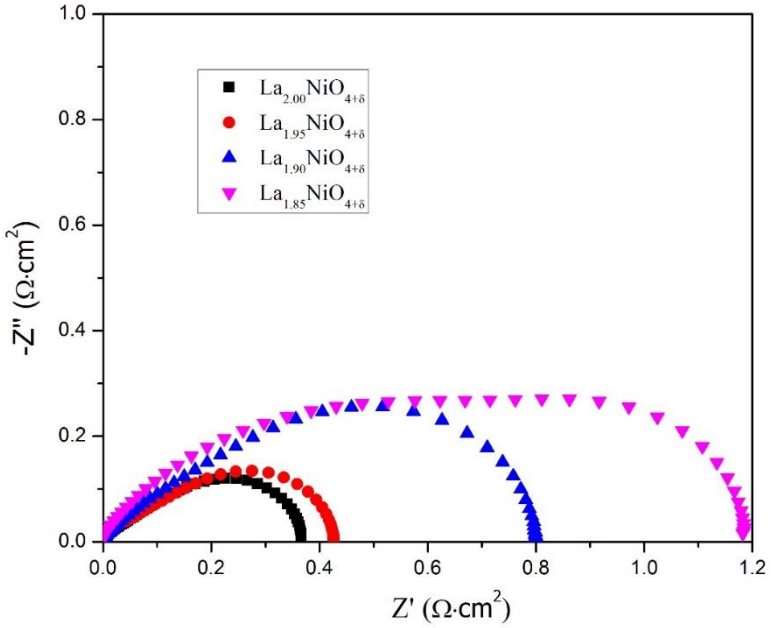

Figure 4. 4 Typical Nyquist plot for A-site deficient La2-xNiO4+δ cathode at 750oC

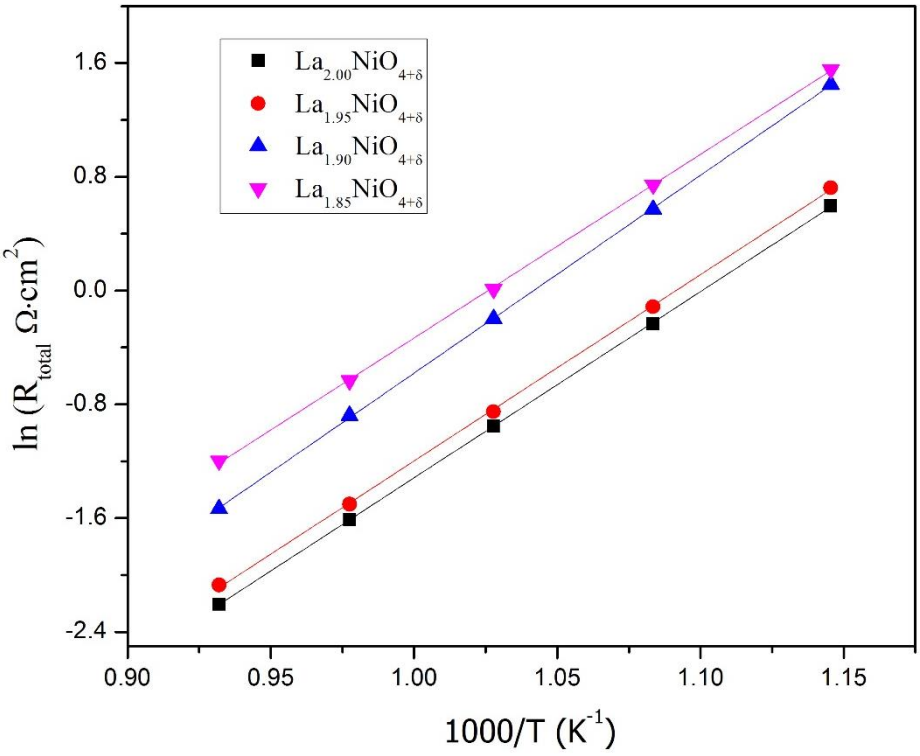

Figure 4. 5 Temperature-dependent polarization cathode resistance of La2-xNiO4+δ (x=0-0.2)

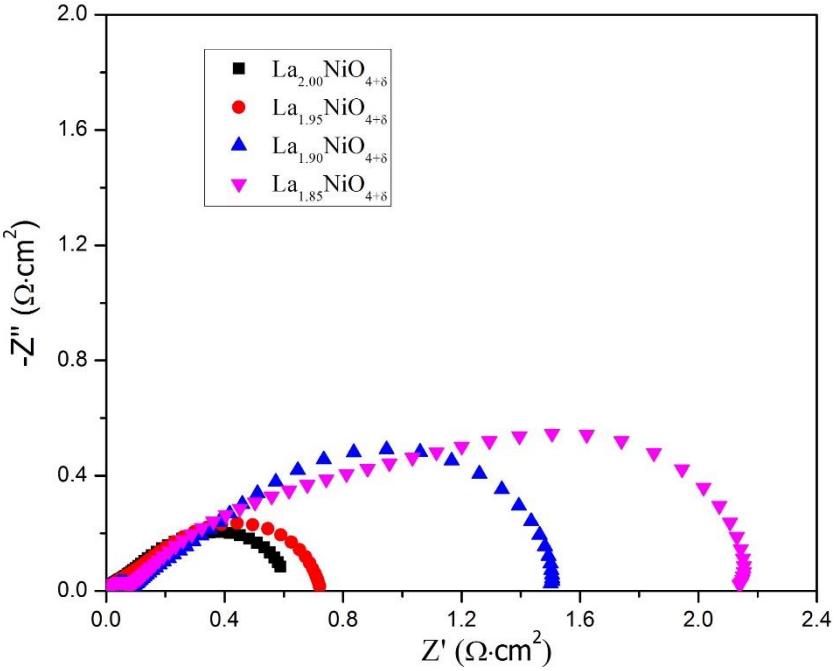

Figure 4. 6 Nyquist plot for A-site deficient La2-xNiO4+δ cathode at 550oC

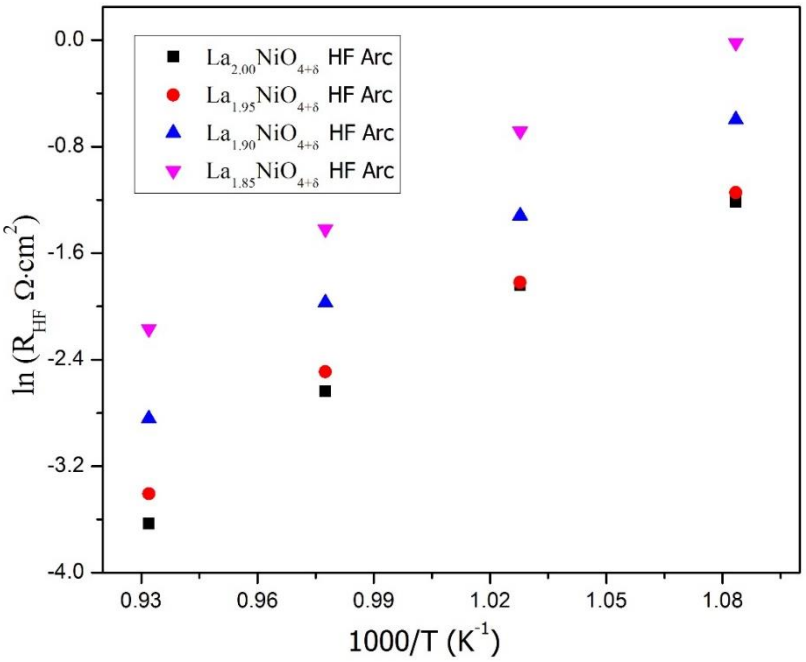

Figure 4. 7 Temperature-dependent polarization cathode resistance of La2-xNiO4+δ (x=0-0.2) for high frequency arcs

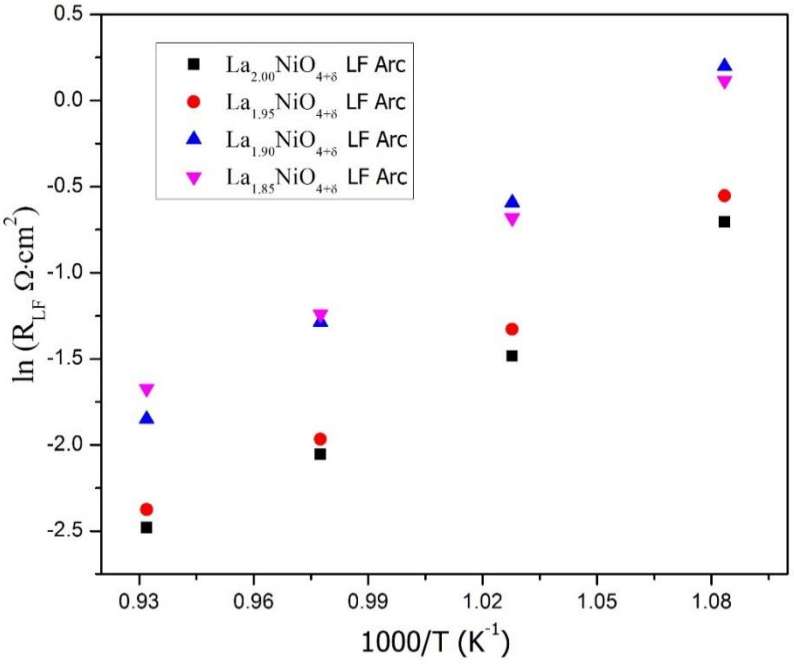

Figure 4. 8 Temperature-dependent polarization cathode resistance of La2-xNiO4+δ (x=0-0.2) for low frequency arcs

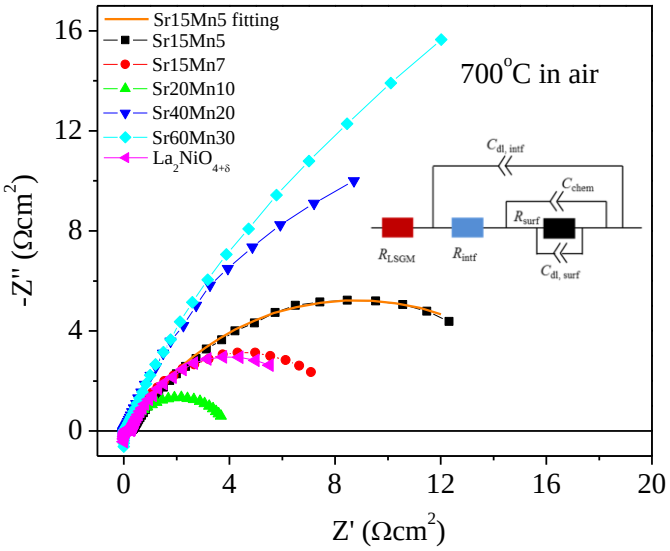

Figure 4. 9 EIS of LSNM symmetrical cells at 700oC in air

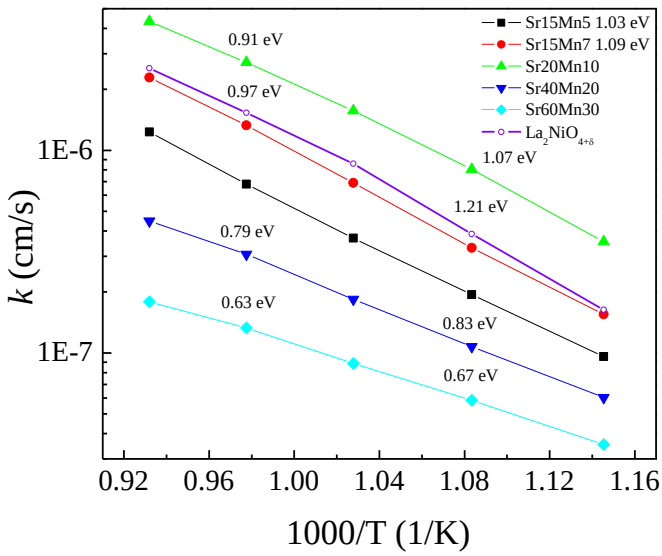

Figure 4. 10 Equivalent k for LSNM calculated from R_{surf}.

Table 4. 2 Summary of resistances, capacitances, characteristic frequencies from ALS fitting.

T=700oC	R_p(Ωcm^2)	O2- transfer nickelates/GDC			chem process		
		R_{IT}(Ωcm2)	C (mF/cm2)	(Hz)	R_{chem}(Ωcm^2)	C_{chem}(mF/cm^2)	α
LNO	0.41	-	-	-	0.41	14.1	0.96
Sr10	0.61	-	-	-	0.61	15.9	0.90
Sr20	1.74	-	-	-	1.74	2.1	0.80
Sr30	8.1	0.83	0.011	13000	7.3	0.20	0.90
Sr40	14.4	1.92	0.091	5400	12.5	0.15	0.88

Table 4. 3 Comparison of k for common R-P phase cathodes at 700oC

	k (cm/s)	Ea (eV)
Sr20Mn10	1.57×10-6	0.91~1.07
La2Ni0.9Co0.1O4+δ	1.41×10-6	0.6

Pr2NiO4+δ	1.0×10-6	0.77
LNO	8.6×10-7	0.97~1.21
La2Ni0.9Fe0.1O4+δ	4.0×10-7	1.39
La1.8Sr0.2NiO4+δ	2.7×10-7	1.06~1.37
Nd1.8Ca0.2NiO4+δ	1.5×10-7	1.35

Task 4.2 Development of $La_2NiO_{4+\delta}$-Infiltrated LSCF Hetero-Structured Cathode

Firstly, we develop a new LSCF based composite materials prepared by infiltration, namely La2NiO4+δ (LNO)-infiltrated LSCF. The special interest associated with the employment of LNO materials mainly lies in the sequent three points: 1) Rapid bulk oxygen diffusion and surface oxygen exchange can be offered in the LNO nickelates based on their additional conduction pathway in high concentration of oxygen interstitials. Skinner et al. have confirmed that LNO-based materials show higher bulk oxygen diffusion coefficient D of about 5×10-8 cm^2s^{-1} than that of LSCF materials by one order of magnitude, and slightly higher surface oxygen exchange coefficient k of about 2-5×10^{-7} cms^{-1} at 700-750ºC) LNO as Sr acceptor shows extremely promising to improve cathode stability and electro-catalytic properties without invoking deleterious LSCF surface reactions related to the formation of inactive Sr species. Reports have shown there is obvious increase in electronic conductivity and oxygen transfer capability of Sr-containing LNO in comparison to LNO itself. Unlike previous research attempting to physically block for Sr-enrichment on the surface of LSCF with surface thin films, a chemical driving force in the LNO/LSCF combination is expected for diffusion of Sr from LSCF into LNO to benefit surface oxygen exchange and material stability of the composite cathode. 3) Hetero-structured interface would potentially extend the active regions of two phase boundary (2PB, LSCF/LNO) and triple phase boundary (TPB, LSCF/LNO/gas) with high oxygen transfer capability, leading to total ORR kinetic enhancement of SOFC cathode. Efforts in development of $(La,Sr)CoO_{3-\delta}/(La,Sr)_2CoO_{4+\delta}$ (LSC113/LSC214) hetero-structured architecture via pulsed laser deposition (PLD) has been made by MTI group. It was found that interfacial regions are responsible for enhanced ORR kinetics of about 3 orders of magnitude for the entire electrode with surface decorations of LSC214 relative to bulk LSC 113.

For these reasons, the main aim of this study is to examine the influence of LNO infiltration into porous LSCF cathode, from both a scientific and technological point of view, on ORR behavior and long-term availability of the LNO-infiltrated LSCF cathodes.

The LNO precursor solution with a concentration of 1 mol/L was composed of $La(NO_3)_3{\cdot}6H_2O$ and $Ni(NO_3)_2{\cdot}6H_2O$ (99.9%, Alfa Aeser) dissolved in mixture of ethanol and deionized water with a ratio of 1:0.6. We confirmed that appropriate amount of ethanol can promote the formation of LNO phase and improve its distribution status on LSCF substrate. After infiltrating the nitrate solution into each side of porous LSCF cathode, the cells were sintered at 900ºC for 1 h to allow the formation of LNO single phase on the LSCF backbone. Repeated infiltration followed by firing process was carried out to increase the amount of LNO phase in the modified cathode.

Figure 4.11 displays the XRD patterns of LSCF pellets with and without LNO infiltration. All of the reflections in the diffract gram of bare LSCF sample on the electrolyte can be labeled in terms of LSCF, GDC and YSZ phases. While the appearance of single Ruddlesden-Popper (RP) phase for LNO infiltrated LSCF sample confirms the existence of LNO in the LSCF backbone. The diffraction peaks of LNO phase can be identified as tetragonal K_2NiF_4 structure of I4/mmm space group (JCPDS card No. 34-0314), which shows excellent agreement with those reported in related literature.

To obtain uniform LNO nano-layer on LSCF surface, microstructure of LNO-infiltrated LSCF was modified in our primary work. Disperser of infiltration solution (TX100), drying rate, concentration of infiltration solution, vacuum treatment and LNO loading, all of which are key factor on infiltration microstructure, are considered in our work.

Figure 4.12 and 4.13 displays the microstructures of LNO-infiltrated LSCF with different heat treatment for low-temperature preprocesses and different mass of disperser. Reducing the heating rate from 5ºC/min to 2ºC/min for low-temperature preprocesses and introduction of disperser TX100 with 0.9g in 1mol LNO solution could homogeneity of solvent evaporation and dispersity of solution, resulting in enhancement of uniformity of LNO nanoparticles. The change of concentration of infiltration solutions and the application of vacuum have little effect on the microstructure as shown in Figure 4.14 and 4.15. Therefore, to simplify infiltration process, 1mol/L infiltration solution was chosen in our future work without application of vacuum.

Figure 4.16 displays the microstructures of LNO-infiltrated LSCF with different loading. The disperser TX100 and ethanol were applied in the infiltration solution to enhance the surface tension and the dispersity of LNO nanoparticles. After repeating the infiltration process, LSCF cathode with different amount of infiltrated LNO were obtained. With increasing the loading of LNO, the distribution of LNO nanoparticles in the LSCF substrate are of island, film or multiple sheet. With 15.4 wt. % LNO infiltration, a uniform LNO nano-layer almost covers on LSCF surface completely with particles size 50-150nm. With continuously increasing the LNO loading to about 20 wt. %, a multiple layer of LNO was formed and the extra LNO nano-particles were found on the LNO layer surface. And Figure 4.17 shows the typical electrochemical impedance spectra of LSCF/GDC/YSZ/GDC/LSCF symmetrical cells with different amount of LNO infiltration under OCV. The small quantity of LNO infiltration, less than 10 wt. %, obtained the largest electrode resistance 0.16 $\Omega \cdot cm^{-2}$ because of the inadequate specific surface area and LNO/LSCF interface, but still lower than the blank LSCF one (about 0.3 $\Omega \cdot cm^{-2}$). And slight increase of cathode resistance was yielded for the electrode with 20 wt. % LNO loading, comparing with the single layer LNO (15 wt. %) infiltration electrode (0.06 VS. 0.08 $\Omega \cdot cm^{-2}$ under 700ºC). Therefore, 15 wt. % LNO loading, which covers on LSCF surface completely with a single uniform LNO nano-layer, was applied in our next work.

Representative EIS data for symmetric cells using bare LSCF or LNO-infiltrated LSCF cathodes collected at OCV in air at temperature of 700 and 750°C, respectively, are shown in Figure 4.18. Typical equivalent circuits have been used to deconvolute the measured data for the cathodes, as displayed in the insets of Fig. 4.19 (a) and (b), where R is the ohmic resistance of the YSZ electrolyte, and R_n and Q_n indicate resistance and constant phase element of different electrode processes, respectively. In the case of LSCF cathode, two RQ elements of semi-circle arcs reflect the electrode polarization. An equivalent capacitance value C_1 ($C_n = (R_n Q_n)^{1/n} / R$) in the range of 10^{-3}-10^{-2} $F \cdot cm^{-2}$ are obtained from high frequency response, which is typically attributed to charge transfer process according to literature. Corresponding to C_2 value of $\sim 10^{-2}$ $F \cdot cm^{-2}$, an intermediate behavior with a similar surface process (e.g. surface diffusion, adsorption/desorption,

dissociation, etc.) between gas diffusion and charge-transfer is observed. For LNO-infiltrate LSCF cathode, an additional contribution at low frequency with C_3 value of $10^0 \sim 10^1$ F·cm^{-2} has also been used for fitting, which may be assigned to gas diffusion as reported elsewhere. Such equivalent circuit model can well resolve the impedance plots of the symmetric cells using different cathodes. The actual polarization resistance of SOFC cathode (R_p) can thereby be deduced from electrode area and half sum of Rn values (symmetric cell).

The Rp values for bare LSCF cathode are 1.34 Ω·cm^{-2} at 700°C and 0.62 Ω·cm^{-2} at 750°C, respectively, which are higher than those in literature reporting Rp≈ 0.3-0.6 Ω·cm^{-2} at 700°C and 0.1-0.3 Ω·cm^{-2} at 750°C. This could be explained by relatively higher sinter temperature of 1150°C applied here for the LSCF cathode, leading to decreased surface area and more Sr segregation. For comparison, LNO-infiltrated LSCF cathode decreases the R_p values into 0.042 Ω·cm^{-2} at 700°C and 0.023 Ω·cm^{-2} at 750°C.The obvious reduction in cathode polarization resistance demonstrates that LNO infiltration enhances the electrochemical activity and surface exchange kinetics of LSCF electrodes. In the meantime, temperature-dependent polarization resistance is also characterized in Figure 4.20, and activation energy (Ea) for the electrode polarization contribution can be calculated from the linear relationship of lnRp-1/T by using the Arrhenius law. It can be observed that the activation energy drops from 1.38 eV to 1.06 eV after the infiltration of LNO into LSCF. Hence, LNO can be further evaluated as an effective catalyst to enhance ORR reaction kinetics and electro-catalytic activity of LSCF cathode. The performance improvement could be resulted from nanoscale LNO fine particles increasing surface active area, hetero-structured LSCF/LNO interface architecture offering more active reaction regions of 2PB and 3PB, and/or favorable cation diffusion from LSCF to LNO facilitating oxygen exchange and transport.

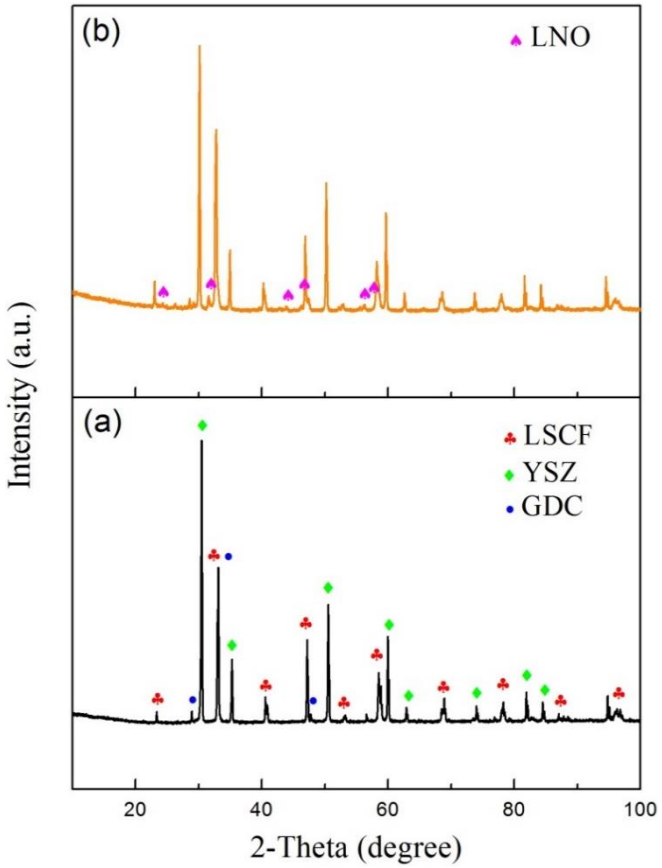

Figure 4. 11 XRD patterns of (a) bare LSCF cathode and (b) LNO-infiltrated LSCF on GDC/YSZ electrolyte.

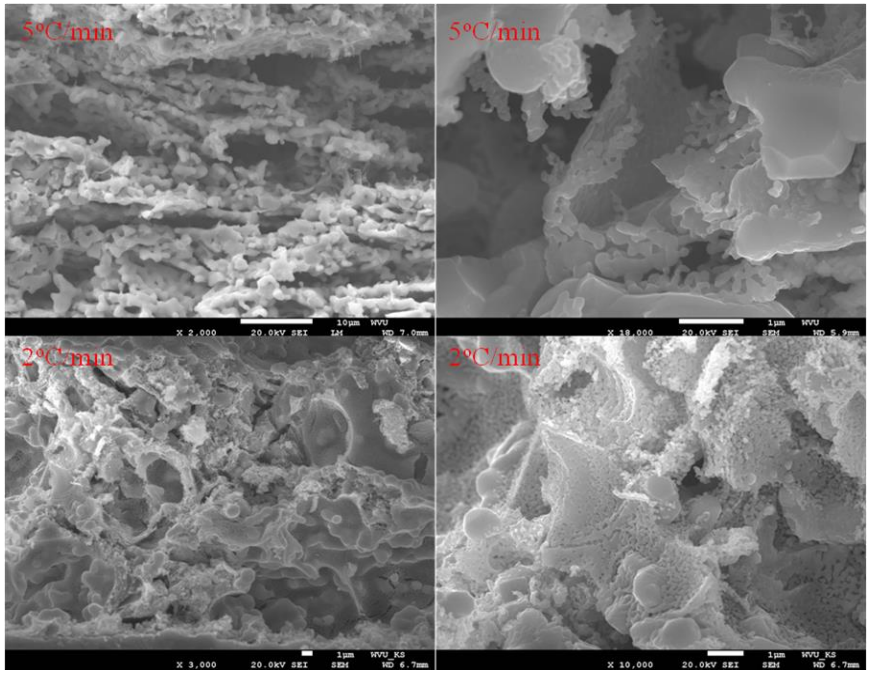

Figure 4. 12 Microstructure of LNO-infiltrated LSCF electrode with different heating rate for low-temperature preprocess

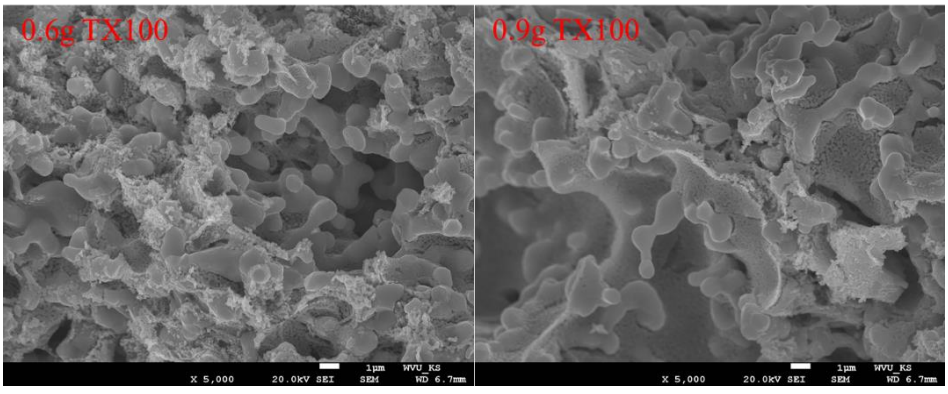

Figure 4. 13 Microstructure of LNO-infiltrated LSCF electrode with different mass of disperser TX100 with 1mol LNO

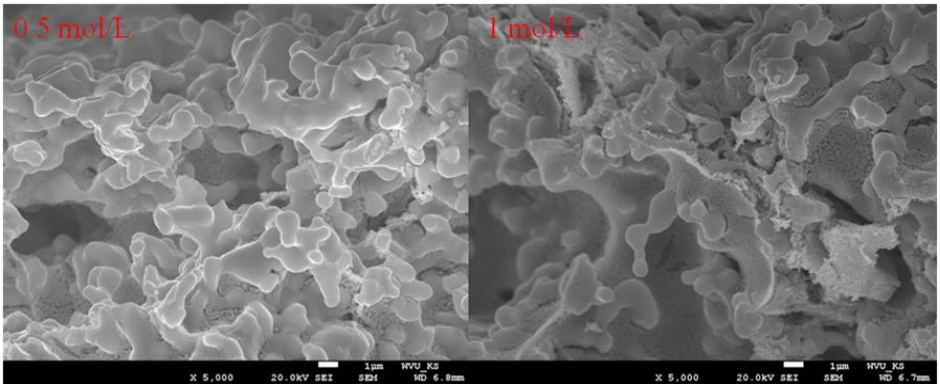

Figure 4. 14 Microstructure of LNO-infiltrated LSCF electrode with different concentration of LNO infiltration solutions

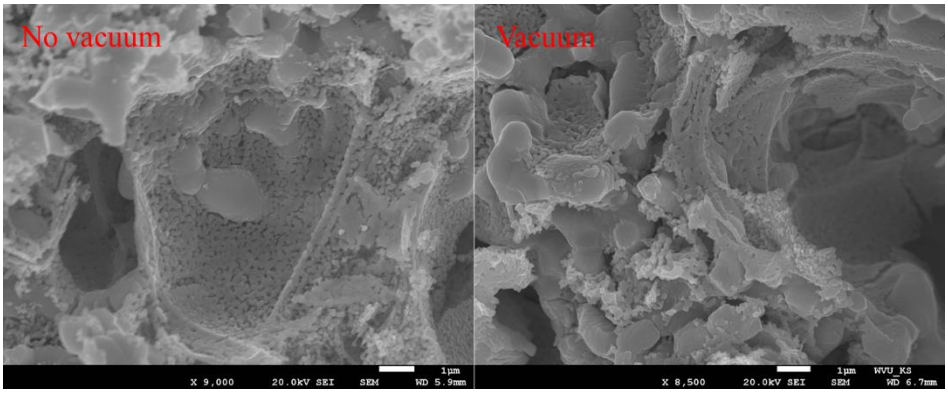

Figure 4. 15 Microstructure of LNO-infiltrated LSCF electrode with and without vacuum treatment during infiltration process

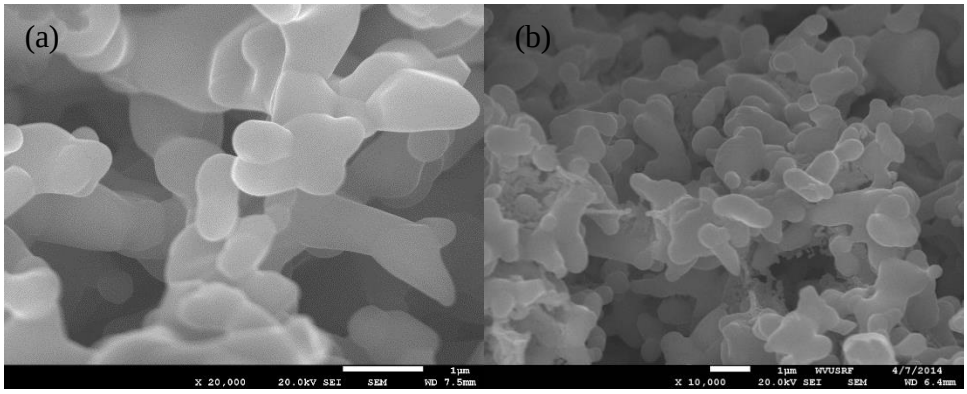

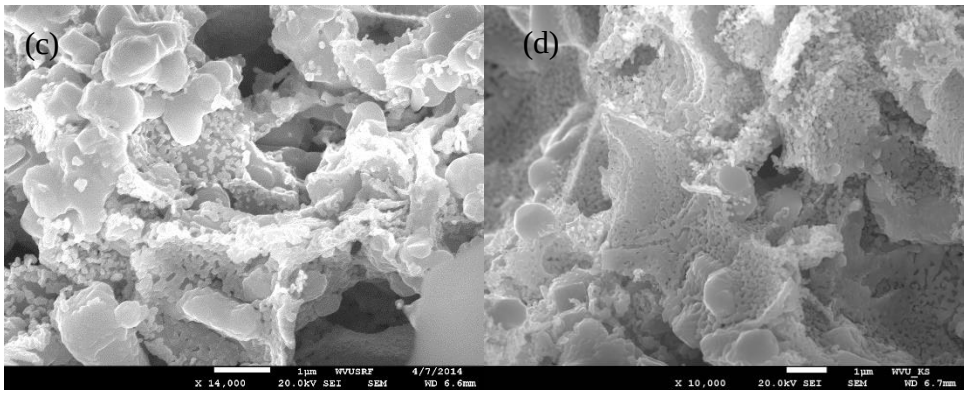

Figure 4. 16 SEM image of LSCF cathode (a) without LNO infiltration or with (b) 8.60 wt. %, (c) 15.4 wt. % and (d) 20.3 wt. % of LNO infiltration after 850oC sintering for 1h.

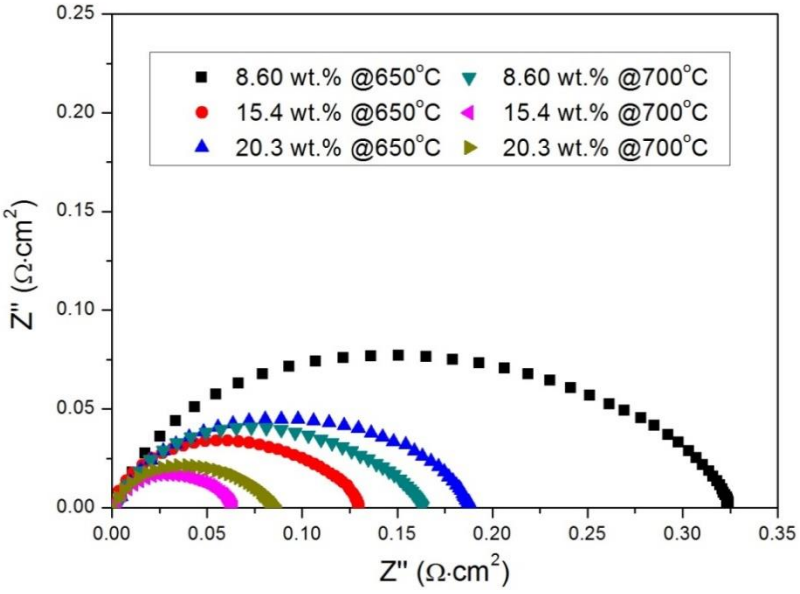

Figure 4. 17 Typical electrochemical impedance spectra of symmetrical cells with different LNO loading under OCV at 650oC and 700oC

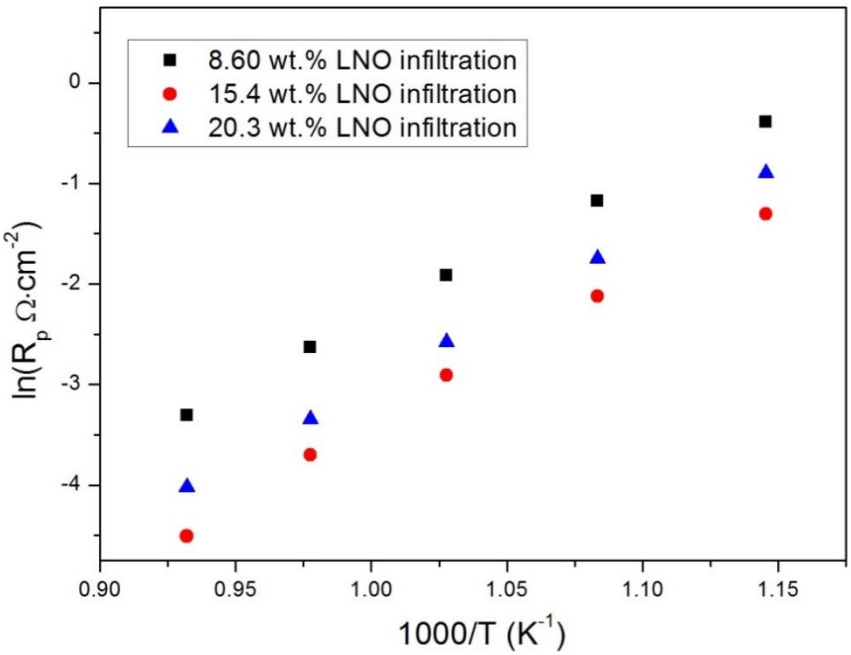

Figure 4. 18 Cathode polarization resistance as function of measuring temperature for LSCF cathode with different LNO loading.

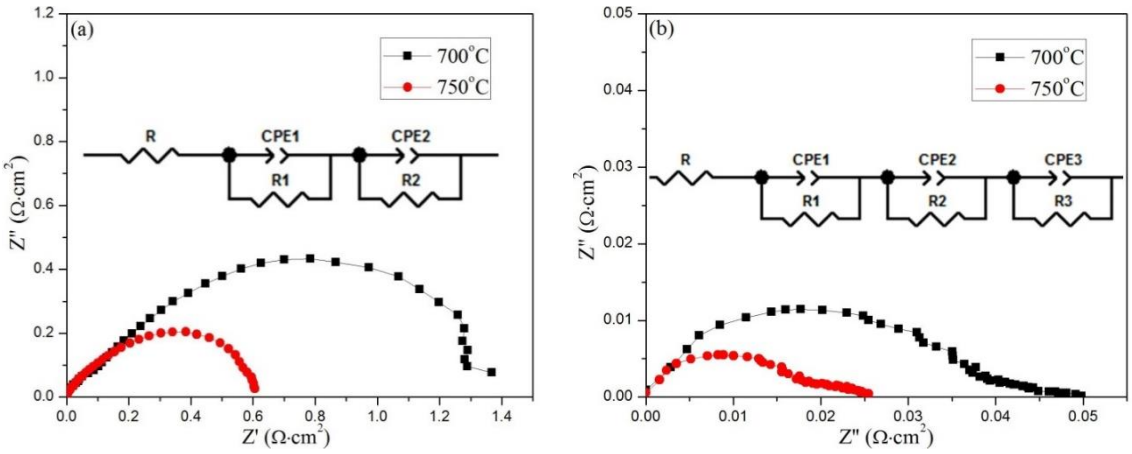

Figure 4. 19 Typical electrochemical impedance spectra of symmetrical cells using LSCF cathodes (a) without and (b) with LNO infiltration under OCV at 700 and 750oC

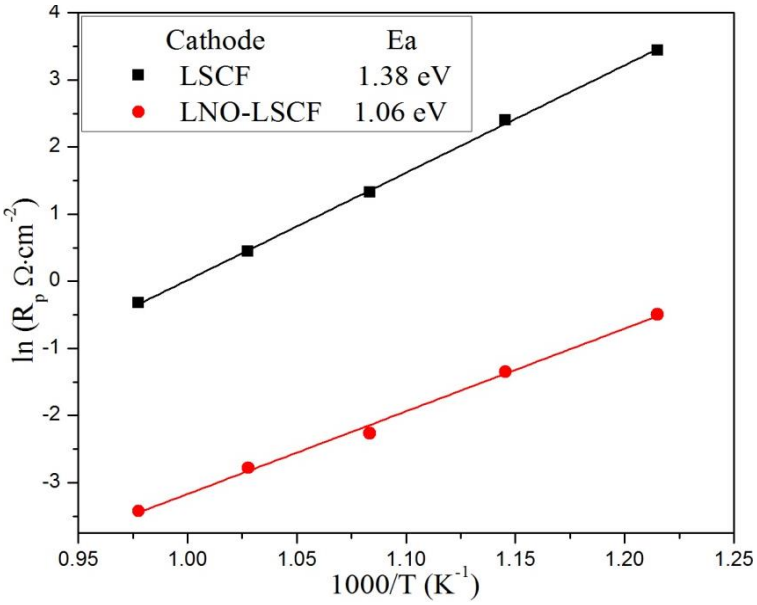

Figure 4. 20 Cathode polarization resistance as function of measuring temperature for LSCF and LNO-infiltrated LSCF cathodes, showing relative activation energies in the inset.

Conventional ECR technique can only be used for characterizing oxygen transport kinetics in single phase cathode. Based on improvement for the ECR data fitting method in our previous work. This technique will be further developed to characterize oxygen transport in the hetero-structured cathode.

Sandwich structure samples were fabricated for characterization of oxygen exchange behavior between the hetero-structured surface and bulk of LSCF cathode. After the system reaches equilibrium under the new oxygen partial pressure, the saturated concentration are $C_{\infty}^{'}$ and C_{∞} separately for the infiltrated material and LSCF. Oxygen flux was assumed as a constant and diffusion process inside the infiltrated layer was ignored due to its very small thickness. Oxygen transport can then be described with the three equations listed below.

$$C_1 - C_{\infty}^{'} = \frac{J}{k_{surface}} \tag{4.2}$$

$$C_2 - C_{\infty} = \frac{J}{k_{interface}} \tag{4.3}$$

$$C_3 - C_2 = \frac{Ja}{D} \tag{4.4}$$

Equation 4.2 is the surface exchange occurring on the gas/hetero-structured surface. Equation 4.2 represents the exchange occurring at the hetero-structured surface/LSCF bulk interface and Equation 4.4 showed the diffusion inside LSCF. Therefore, the total surface exchange coefficient can be deduced by combining Equation 4.2 and 4.3. the oxygen exchange coefficient at LNO/LSCF interface will be deduced based on our previous study for LSCF.

$$\frac{1}{k} = \frac{1}{k_{\text{interface}}} + \frac{1}{k_{\text{interface}}} \tag{4.5}$$

$$k_{surface} = \frac{cS_V k_{LNO}}{1-V} \tag{4.6}$$

Where, c is the thickness of LNO thin layer, SV is the specific surface area and V is the porosity

Therefore, the ECR of pure LSCF, LSCF and LNO-coated LSCF samples were measured in our work. Here, pure LNO samples have been prepared by dry pressing method and sintering at 1300℃. Fig. 4.21 shows normalized conductivity relaxation data and the correspondingly fitted curves of pure LNO sample at 700°C for reduction steps at different oxygen partial pressures as function of time. The total relaxation time for LNO is about 900 s when lowering PO2 from 0.2 to 0.18atm, and a longer relaxation time of 1100 s is observed for 0.02 to 0.018atm. Hence, a faster equilibration time can be obtained when using higher oxygen pressure, indicating *k&D* change with oxygen partial pressure.

Fig. 4.22 shows the surface exchange coefficient plot of the LNO at different PO2. The fitted oxygen surface exchange k and diffusion coefficient D at different PO2 are listed in Table 4.4. The oxygen surface exchange coefficient of LNO is increased with decreasing oxygen partial pressure. From 0.05 to 0.15 atm, there is slight change in k values. This could be explained by isothermal adsorption regime. Based on the initial guesses of D and k used in the fitting process, error analysis needs to be further performed to confirm the accuracy of surface oxygen exchange coefficient.

Fig. 4.23 shows the oxygen diffusion coefficients of the LNO sample as function of PO2.With the decrease of oxygen partial pressure, the relaxation time enlonged. It has been reported that for perovskite oxides oxygen diffusion coefficient depends on both oxygen vacancy concentration and vacancy diffusion coefficient. In LNO material, its ion carriers primarily consist of interstitial oxygen ion and oxygen vacancy. However, the amount of interstitial oxygen in LNO material plays a key role in the oxygen diffusion coefficient. As reported in literature, the amount of hyper-stoichiometric interstitial oxygen decreases with the decrease of oxygen partial pressure. It is thereby reasonable to conclude that D value of the LNO sample drops as oxygen partial pressure decreases.

Fig. 4.24 shows the normalized conductivity relaxation plots and fitted curves for the LNO-coated LSCF samples at 700℃ at different oxygen partial pressures. The total surface exchange coefficients for the LNO-LSCF coated samples obtained from the fitted data are listed in Table 4.4. The total surface oxygen exchange coefficients increase as the oxygen partial pressure increases in term of the (PO2)1/2 law. It can be observed that the bulk diffusion coefficients of LSCF decrease with increasing oxygen partial pressure. This can be attributed to the change of oxygen vacancy concentration at different oxygen partial pressure. The $k_{\text{interface}}$ values decrease with the increase of oxygen partial pressures, showing the similar trend of total surface oxygen exchange coefficients with oxygen partial pressures. Also, these results could be associated with the decrease of surface oxygen coefficient of LSCF with the reduction of oxygen vacancy concentration.

In the previous study, the oxygen transport process of SOFC cathodes including dense La2NiO4+δ (LNO) and LNO/LSCF/LNO has been studied to describe the change of oxygen chemical surface exchange coefficient (k) and chemical diffusion coefficient (D) as a function of oxygen partial pressure, based on the perturbation of oxygen stoichiometry during ECR measurements. However, the global minimum of the error for oxygen exchange coefficient is

much larger. To obtain more accurate k value, the single process control sample is required, which reduces the diffusion equations to a single k dependent equation as shown in Equation

$$1 - \frac{\sigma(t) - \sigma(0)}{\sigma(\infty) - \sigma(0)} = \exp(-\frac{kt}{a}) \quad (4.7)$$

Where, σ, k, t and a represent conductivity, surface oxygen coefficient, time and sample thickness. Since the characteristic length for LNO and LSCF 50-500μm, the thickness of the k single process control sample should less than the characteristic length. In our experiment, the dense LNO and LNO/LSCF thin film based on GDC substrate were prepared by air brush spraying method with thickness about 50μm. Figure 4.27 shows a typical set of normalized conductivity relaxation data and the correspondingly fitted curves of LSCF/GDC and LNO/LSCF/GDC samples at 700℃, respectively, for reduction steps switching PO2 from0.20 atm to 0.18 atm as function of time. The fitted oxygen surface exchange k of LSCF and LNO/LSCF at different PO2 are listed in Table 4.5. It can be seen from Fig. 2 that the total relaxation time for LSCF is about 140-160s when lowering PO2 from 0.21 to 0.18 atm, which is longer than LNO/LSCF sample about 40-60 s. The total surface oxygen exchange coefficient of LSCF and LNO/LSCF is about 9.02×10-4 cm/s and 1.9×10-4 cm/s at 700℃ under air condition, respectively, which means the LNO coating with Co diffusion would enhance the surface ORR rate. The Co diffusion in LNO layer would enhance the surface oxygen exchange rate comparing with the pure LNO one. The surface exchange coefficient of La2NiO4+δ was tested and listed in Table. 4.6. Meanwhile, surface oxygen exchange coefficient of the LSCF and total LNO/LSCF decreases as a function of the square root of oxygen particle pressure. According to the thermodynamic properties and oxygen exchange kinetics, the dependence of surface oxygen exchange coefficient on temperature and oxygen particle pressure reflects the oxygen reduction mechanism. The k order in PO2 is about 1/2 in our experiment, which usually means that the rate limiting step in ORR is oxygen incorporation into surface oxygen defect site. The modified ECR code and experiment error and will be carry out to improve the accuracy and confirm the relationship between k value of the LNO/LSCF and PO2 in our further work to obtain the mechanism of interface oxygen exchange.

According to the $k_{La2NiO4+\delta}$ and $k_{LNO\text{-}LSCF\ total}$, It can be deduced from eq. (2) that the interface oxygen exchange coefficient between LNO and LSCF is about 3×10-4 cm/s. The higher $k_{interface}$, with respect to k_{LSCF} (9.02×10-5cm/s), indicates that the incorporation rate of oxygen into LSCF is enhanced when using LNO/LSCF cathode.

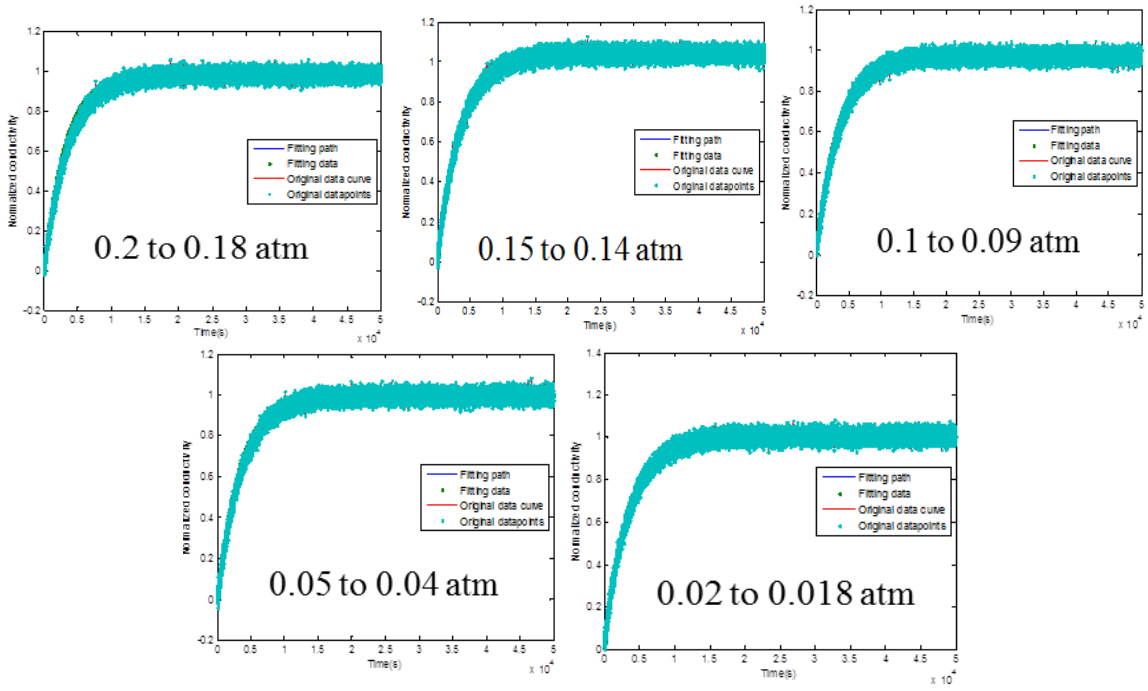

Figure 4. 21 Normalized conductivity results and fitting curves of LNO with oxygen partial pressure, changing from 0.2 to 0.18atm, 0.15 to 0.14atm, 0.1 to 0.09atm, 0.05 to 0.04atm, and 0.02 to 0.018atm at 700 C.

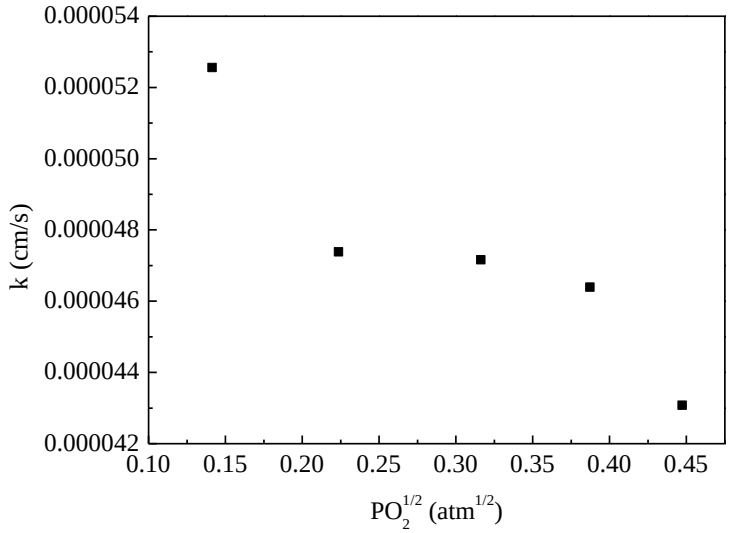

Figure 4. 22 Surface oxygen exchange coefficient of LNO at different PO2

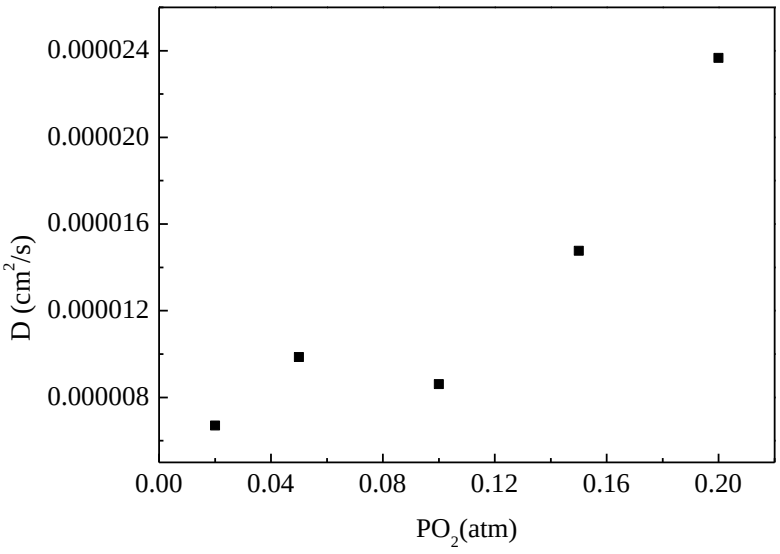

Figure 4. 23 Oxygen diffusion coefficient of LNO at different PO2

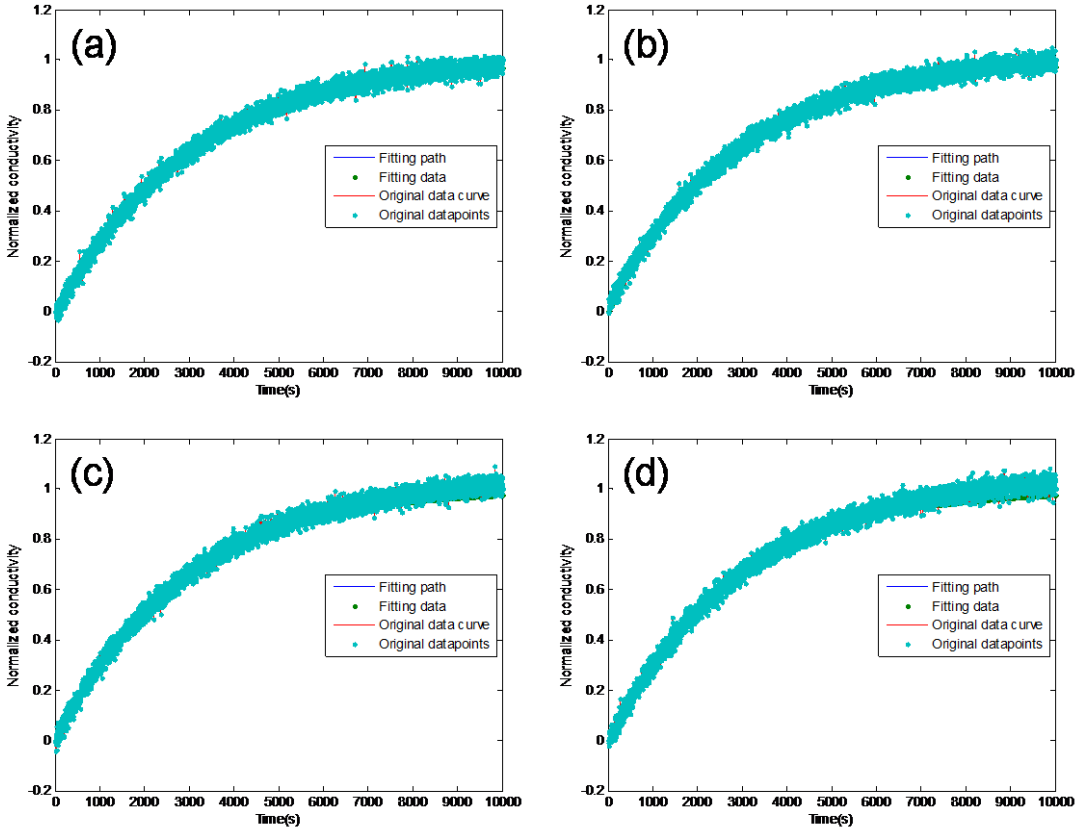

Figure 4. 24 ECR fitting data for LNO-LSCF-LNO samples at 700oC under different oxygen partial pressure (a) 0.20-0.18 atm, (b) 0.10-0.09 atm, (c) 0.05-0.04 atm and (d) 0.02-0.018 atm.

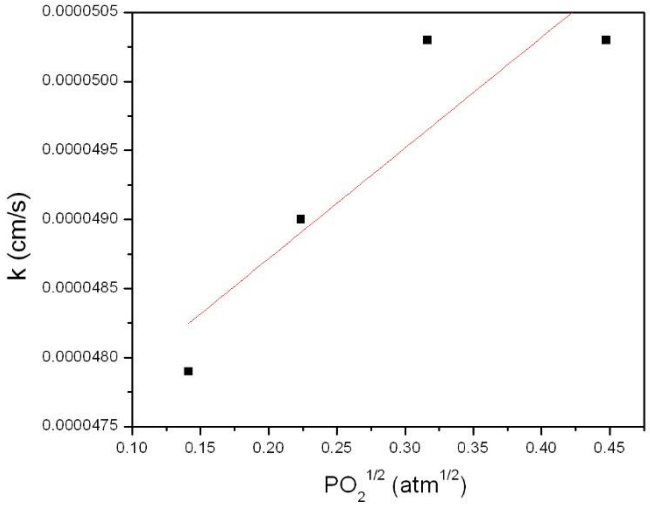

Figure 4. 25 Total surface oxygen exchange coefficient of LNO-coated LSCF as a function of oxygen partial pressures at 700℃.

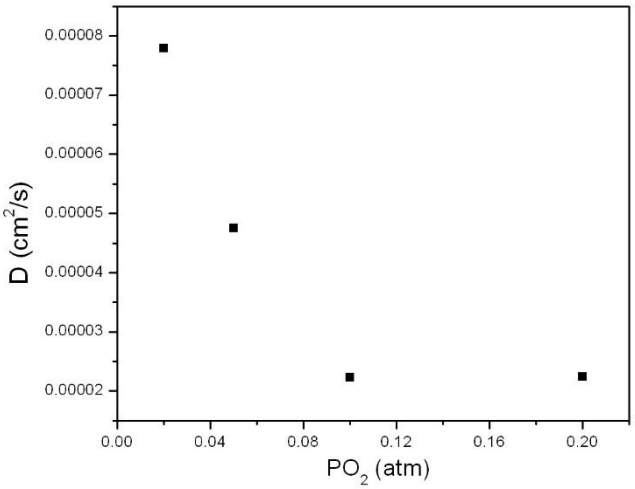

Figure 4. 26 Total oxygen diffusion coefficient of LNO-coated LSCF as a function of oxygen partial pressures at 700℃.

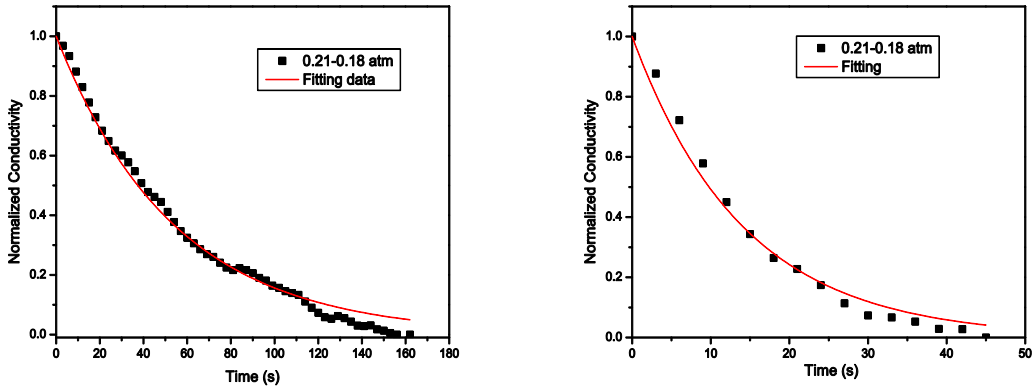

Figure 4. 27 Normalized conductivity results and fitting curves of (a) LSCF and (b) LNO-coated LSCF (LNO/LSCF) samples at 700℃ at air switched to 0.18 atm.

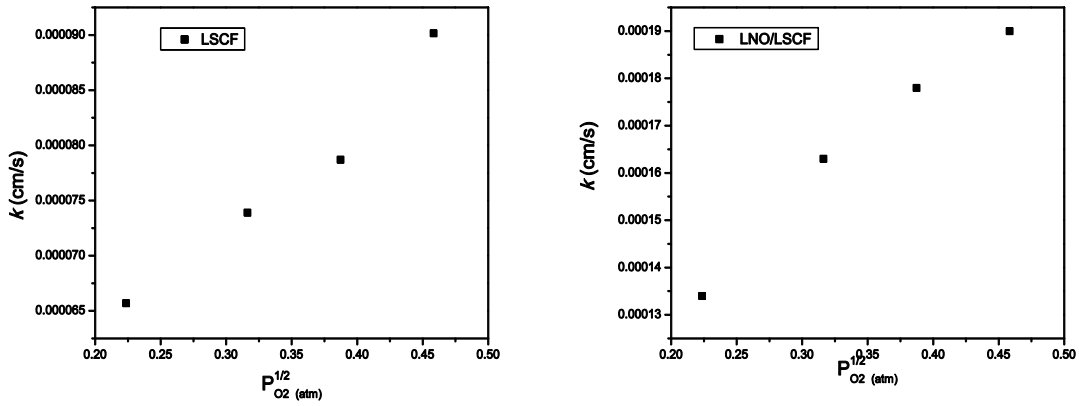

Figure 4. 28 Surface oxygen exchange coefficient of (a) LSCF and (b) LNO-coated LSCF (LNO/LSCF) samples as a function of PO21/2at 700oC.

Table 4. 4 The oxygen surface exchange coefficient and oxygen diffusion coefficient of LNO at different oxygen partial pressure.

PO2(atm)	0.2	0.15	0.1	0.05	0.02
k(cm/s)	4.31E10-5	4.64E10-5	4.71E10-5	4.74E10-5	5.26E10-5
D(cm2/s)	2.37E10-5	1.47E10-5	8.6E10-6	9.85E10-6	6.96E10-6

Table 4. 5 Total surface oxygen transport kinetic parameters for LNO-coated LSCF samples

P_{O2} (atm)	0.20	0.10	0.05	0.02
D (cm2/s)	2.24E-05	2.23E-05	4.75E-05	7.79E-05
k (cm/s)	5.03E-05	5.03E-05	4.90E-05	4.79E-05
$k_{surface}$(cm/s)	1.27E-04	1.39E-04	1.40E-04	1.55E-04
$k_{interface}$ (cm/s)	8.32E-05	7.88E-05	7.54E-05	6.93E-05

Table 4. 6 The surface oxygen exchange coefficient (k) and of La2NiO4+δ, LSCF and LNO-coated LSCF (LNO/LSCF) cathode at 700℃ under different oxygen pressure.

PO2 (atm)	0.21	0.15	0.10	0.05
$k_{La2NiO4+\delta}$ (cm/s)	3.95 E-04	3.54 E-04	3.26 E-04	2.83 E-04
k_{LSCF}(cm/s)	9.02 E-05	7.87 E-05	7.37 E-05	6.57 E-05
$k_{LNO-LSCF}$ total (cm/s)	1.90 E-04	1.78 E-04	1.63 E-04	1.34 E-04
$k_{LNO-LSCF\ interface}$ (cm/s)	3.66 E-04	3.58 E-04	3.26 E-04	2.55 E-04

Task 4.3 Further Stability Improvement of $La_2NiO_{4+\delta}$-based Infiltrated LSCF Hetero-Structured Cathode

For comparison and performance evaluation, $La_{2-x}NiO_{4+\delta}$ (x=0-0.2) was infiltrated into the both sides of LSCF layers in the LSCF|GDC|YSZ|GDC|LSCF cell to form a symmetric cell using LNO infiltrated LSCF cathode. Representative EIS data for symmetric cells using $La_{2-x}NiO_{4+\delta}$ (x=0-0.2) cathodes are collected at different temperature under OCV in air. Temperature-dependent polarization resistance is characterized in Figure 4.29. The R_p values of $La_{2-x}NiO_{4+\delta}$ (x=0-0.2) infiltrated LSCF cathodes are 0.025, 0.028 and 0.035 $\Omega \cdot cm^2$ at 750 °C, respectively. The cathode electrochemical performance reduces with increasing the concentration of lanthanum deficient, which is consistent with the pure $La_{2-x}NiO_{4+\delta}$ (x=0-0.2) cathode properties because of its surface electro-catalytic. The obvious one order of magnitude decrease in cathode polarization resistance after infiltration demonstrates that A-site deficient $La_{2-x}NiO_{4+\delta}$ is still one potential infiltration materials for bare LSCF cathode. The cells with $La_{2-x}NiO_{4+\delta}$ infiltrated LSCF cathode will be assembled, and the stability of the cathode will be characterized and analyzed in the future.

To avoid the influence of microstructure variation of infiltrated nanoparticles, the stabilities of electrochemical performance of infiltrated LSCF were examined by dense $La_{2-x}NiO_{4+\delta}$ coated LSCF thin cathode fabricated by air-brushed dry pressing method. The electrochemical impedance data were collected after different polarization times from 30-960mins. In the all case of $La_{2-x}NiO_{4+\delta}$ (x=0-0.2) cathodes, two RQ elements of semi-circle arcs reflect the electrode polarization. The small high frequency arcs are correspond with electrode/electrolyte interface process based on the high frequency 10^5 Hz, and the large low frequency arcs reflect surface ORR process. The initial R_p values of $La_{2-x}NiO_{4+\delta}$ (x=0-0.2) coated LSCF cathodes increase with

increasing the concentration of lanthanum deficient, which is consistent with the pure $La_{2-x}NiO_{4+\delta}$ (x=0-0.2) cathode properties because of its surface electro-catalytic.

In our previous work, the growth of the infiltration particles can be detected by TEM from 50nm to about 150nm after long-term cell operation, which is the one key factor for the cell performance degradation. For particles growth process, three major mechanisms have been developed and applied in the past investigation of sintering phenomenon according to the characteristic of mass transfer, which are 1) lattice, grain boundary and surface diffusion of mass transport; 2) viscous flow of mass transport; 3) evaporation-condensation of mass transport. Among which the diffusion and viscous flow of mass transport are the main factors for ceramic particles growth at high temperature. In diffusion-controlled particles growth, atom diffusivity and mobility based on the gradient of vacancy concentration decide the rate of particles growth. To suppress kinetics of particles growth, one method is reduce the atom vacancy concentration by adjustment of dopant. The other one is introduce uniform second phase with low atom diffusivity into backbone materials to inhibit the inter-diffusion of atoms. CeO2 has been provided with low inter-diffusion properties with most atoms of cathode materials, which has been wildly used as interlayer between YSZ and cathode to restrain the diffusion of lanthanum and strontium etc.. While, in viscous-controlled process, either for Newtonian fluid or plastic fluid, the concentration of molten mass is one of key factors on growth kinetics, which is mostly related with the melting point of particles. The higher particles growth temperature will be obtained when the materials with higher melting point are introduced in electrode. The cubic fluorite structure of CeO2 shows more than 500oC (2400oC) higher melting point than common cathode materials. Hence, it is a potential second phase in electrode to reduce nano-particles growth. The high-melting-point and stable materials CeO2 along with La2NiO4+δ was co-infiltrated into backbone to prevent the particle growth and aggregation in our next work.

CeO_2 & $La_2NiO_{4-\delta}$ was co-infiltrated into the both sides of LSCF layers in the LSCF|GDC|YSZ|GDC|LSCF cell at same time to form a symmetric cell using CeO_2 & $La_2NiO_{4-\delta}$ co-infiltrated LSCF cathode. After drying at 250^oC for 1h, the infiltration steps were repeated to reach the desired loading. Then, the result cells were sintered at 900^oC to decompose nitrite and form pure RP and CeO_2 phase. The loading was detected by balance. Silver ring were attached to both electrode sides of the symmetric cells by using Pt paste as current collectors.

Fig.4.30 shows the XRD patterns of the CeO_2 & LNO co-infiltrated LSCF electrode based on YSZ electrolyte with GDC as buffer layer. The CeO_2 and LNO characteristic peaks were seen in the XRD patterns. But the sharpness and intensity of the peaks of CeO_2 and LNO were much weaker than backbone. So in order to confirm the purity of the CeO_2 & LNO co-infiltration since CeO_2 & LNO were infiltrated in one steps and there is no second phase existence, the metal nitrate infiltration solutions mixed with complexing agent citric acid were evaporated at 80^oC to obtain the gel, and oxide powder were yielded after combusting the gel at 250^oC and sintering the precursor at 1100^oC for 6h. Figure 4.31 shows the XRD patterns of oxide powder. Only LNO peaks with tetragonal structure and CeO_2 peaks were seen in the patterns. But the position of CeO_2 peaks move to the smaller angles, which means larger lanthanum ion was possibly doped into CeO_2 lattice when mixing cerium and lanthanum ions together.

The electrochemical performances for the CeO_2 & LNO co-infiltrated LSCF cathode were characterized by electrochemical impedance spectroscopy. The typical Nyquist diagrams of the CeO_2 & LNO co-infiltrated LSCF symmetrical cells show in Fig. 4.32 with different CeO_2 weight ratio. After CeO_2 co-infiltration, the gas diffusion arcs disappear with increasing the CeO_2 concentration, and there are two R-Q elements of semi-circle arcs reflecting the electrode polarization similar with the pure LNO infiltration. The high frequency arc is corresponding with the

charge transfer process and the intermediate frequency one is attributed to the surface adsorption/dissociation process. Both of them increase with increasing the concentration of CeO_2 infiltration, because of the lower catalytic and conductivity of CeO_2 compared with LNO. From the data of fitting electrode resistance shown in Figure 4.33, the activation energy Ea increases with increasing CeO_2 concentration in the infiltration solution. But compared with bare LSCF cathode, it can be seen that the resistance for 20 mol % CeO_2 & LNO co-infiltrated LSCF is still one magnitude less than pure LSCF. Hence, CeO_2 & LNO are still one potential infiltration materials for bare LSCF cathode. And Gd or Sm doped CeO_2 materials possessing higher catalytic activity will be introduce in the co-infiltration process to enhance the electrochemical performance in our future work.

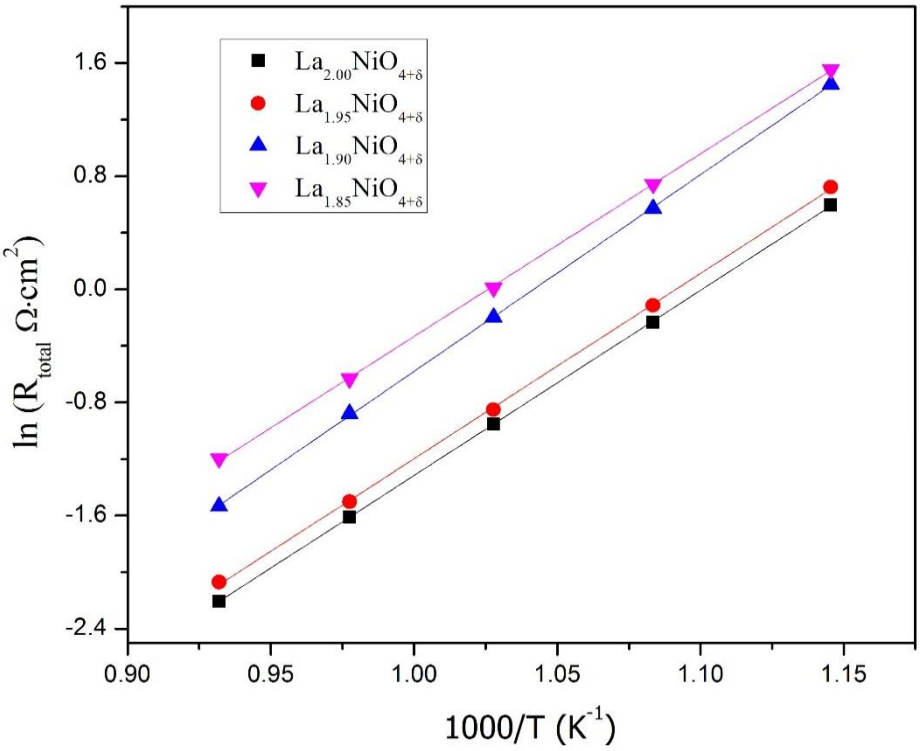

Figure 4. 29 Temperature-dependent polarization cathode resistance of $La_{2-x}NiO_{4+\delta}$ (x=0-0.2).

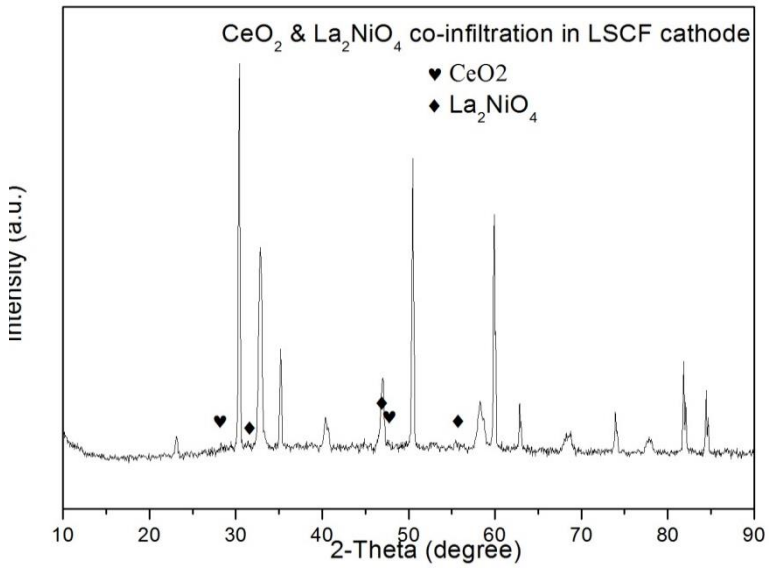

Figure 4. 30 XRD pattern of CeO2 & LNO infiltration electrode.

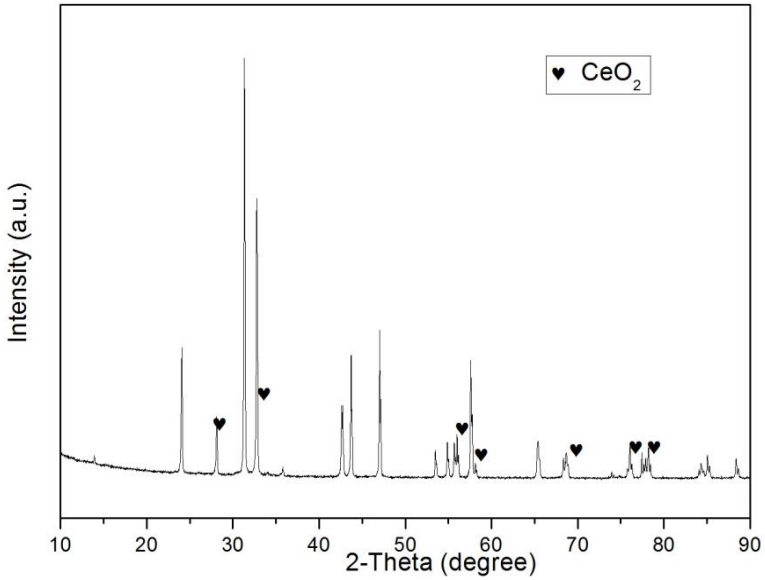

Figure 4. 31 XRD pattern of CeO2 & LNO powders co-synthesized by sol-gel solution

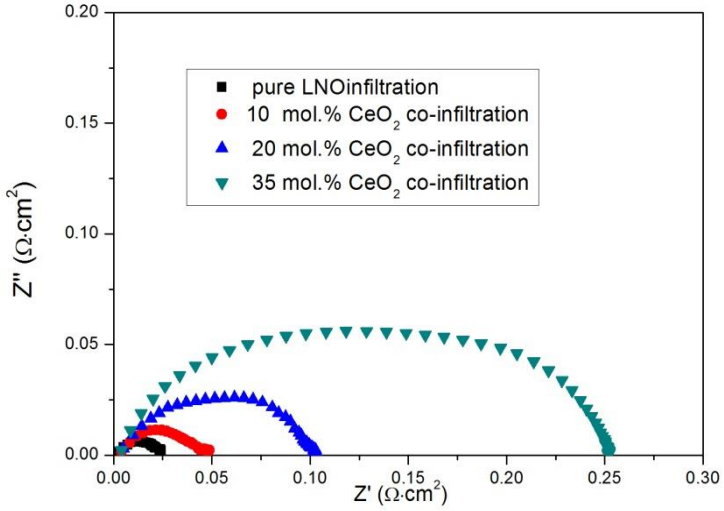

Figure 4. 32 Nyquist diagram of electrochemical impedance spectra for LNO infiltrated LSCF symmetrical cells with and without CeO2 co-infiltration.

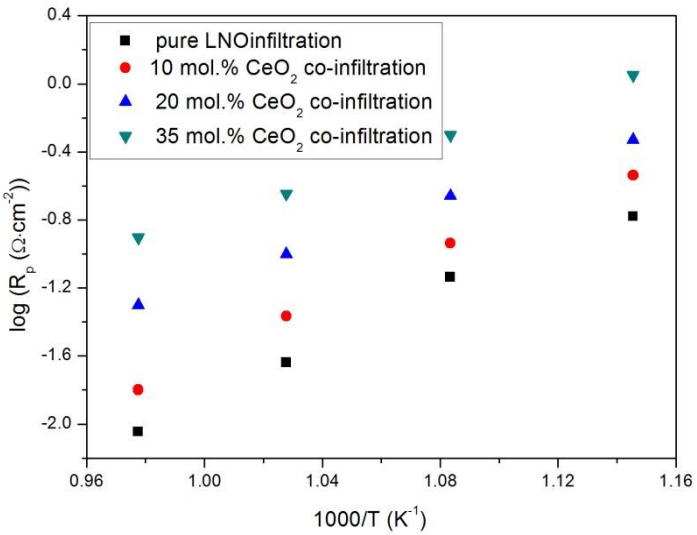

Figure 4. 33 Arrhenius plots of fitted electrochemical impedance spectra for LNO infiltrated LSCF symmetrical cells with and without CeO2 co-infiltration.

Task 5: Long-term Stability

Task 5.1 Microstructural Characterization

It has to be emphasized that the degradations observed for bare LSCF and LNO-infiltrated LSCF cathodes should be ascribed to different mechanisms. The performance loss with time for the

bare LSCF could be associated with cation segregation, like the diffusion of Sr and La into cathode surface, as widely suggested in the literature. While nanoparticle thermal coarsening or low-performance phase formation resulted from chemical instability between bulk substrate and surface catalyst is usually responsible for long-term operation degradation of cathode containing surface catalysts. In order to explain relatively higher degradation rate of LNO-infiltrated LSCF cathode, the SEM, TEM and EDAX characterization analyses after the on-cell testing are depicted in Figure 5.1 and 5.3. It can be observed that the growth of LNO nanoparticles from around 50nm to 100-150 nm occur and LNO nanoparticles are delaminate from LSCF backbone. Correspondingly after on-cell testing of 500 h, the loss of interface, surface area and 2PB/3PB active regions during the intermediate-temperature measurements could be responsible, at least in part, for the performance degradation the LNO-infiltrated LSCF cathode. At the same time, the surface chemistry states of LNO-infiltrated LSCF has been investigated to study the degradation mechanism of LNO-infiltrated LSCF further by XPS. Figure 5.2 shows the La 3d and Ni 3p spectra on the surface of LNO-coated LSCF samples. The La 3d peak were fitted by at least two sets of La 3d5/2 and 3d3/2 doublets with an energy separation of 1.79 eV and a branching ration of 0.67. And Ni 3p were also fitted by at least two sets of Ni 3p 3/2 and 3p1/2 doublets. They represent the surface and bulk chemistry state of La and Ni. Based on the area of peaks, the ratio of La and Ni was calculated. The ratio of La to Ni changes from 2.25-2.89 to 3.94 after 0.2V cathodic polarization. Lanthanum enrichment was found on the surface after polarization, which occupies the surface efficient site instead of active nickel elements. It is possible another reason for the degradation of LNO-infiltrated LSCF cathode.

EDAX results of LNO-infiltrated LSCF cathode indicate that the diffusion of Co, Sr and Fe occurs from LSCF to LNO phase. The extraction of the cations from LSCF perovskite lattice reveals the intrinsic instability of the LSCF cathode. As an acceptor, LNO materials could positively take advantage from the cation diffusion to enhance surface catalytic properties and ORR kinetics. The cobaltic electrode usually feature fast oxygen surface exchange and high electro-catalytic activity for oxygen reduction. It has been reported that doped-Fe LNO, at least for small amounts of Fe loading have no influence on the electro-catalytic properties of LNO materials. As to Sr doping into LNO, a possible reaction according to charge compensation may appear to increase the concentration of electron hole, as below,

$$2SrO + Ni_{Ni}^{\times} \longleftrightarrow 2Sr_{La}^{'} + Ni_{Ni}^{\bullet} + O_{O}^{\times} \tag{5.1}$$

More importantly, a space charge layer at the LNO/LSCF hetero-structured interface could be introduced based on charged transport and defect chemistry from the cation segregation. These facts might lead to the improved electrochemical performance and fast surface exchange of the LSCF based cathode. Certainly, evidence to support these hypotheses should be provided by evaluating the valence and amount of the Fe (Ⅳ)/Fe(Ⅲ), Co(Ⅳ)/ Co (Ⅲ), Ni(Ⅳ)/ Ni (Ⅲ) and Sr (Ⅱ) in the LNO infiltrant in the course of durability evolution. Further work on detailed characterizations associated with ORR process and kinetics of the composite cathodes are shown below.

To acquire useful information about LNO/LSCF interface and surface, dense LNO-coated LSCF samples have been prepared by using spin-coating and air-brushed dry pressing method. XRD pattern of the LNO-coated LSCF materials shows that no extra lines than pure Ruddlesden-Popper (RP) phase (PDF# 34-0314) are observed in the XRD diagram. Figure 3.16 displays the SEM cross-section of the LNO-coated LSCF sample. It can be observed that a dense LNO of

about 4.0μm thickness was coated on LSCF backbone. In the meantime, strong bonding between LNO and LSCF should be benefited from high temperature co-fired process. Sr and Co diffusion from LSCF to LNO occurs along with EDX line scans can be detected from Figure 5.5, which is consistent with the previous TEM and EDX data in infiltrated LSCF cathode. We then performed XPS measurements to examine the changes in the surface composition of $La_2NiO_{4+\delta}$ based layer after heating treatment. Figure 5.6 shows the XPS Sr spectra on the $La_2NiO_{4+\delta}$ layer surface and bulk after 1350^{o}C sintering. The Sr 3d peak were found on the $La_2NiO_{4+\delta}$ surface, which means $La_2NiO_{4+\delta}$ would be an acceptor for Sr segregation or diffusing from LSCF substrate to relieve the stability problem of LSCF. The Sr 3d peak was found to be fitted by at least two sets of Sr 3d5/2 and 3d3/2 doublets with an energy separation of 1.79 eV and a branching ration of 0.67, corresponding to single set of that in LSCF bulk. The additional peak can be associated with the different sites of Sr in LNO (ABO_3 perovskite layer and AO salt layer) and/or surface secondary phases such as $SrO/Sr(OH)_2$, which will be compared with pure Sr-doped $La_2NiO_{4+\delta}$ materials in our future work to verify the Sr state in $La_2NiO_{4+\delta}$ layer.

To primary confirm the influence of CeO_2 nano-particles on the nano-particles growth, the electrode undergone heat treatment at 750^{o}C for 300h. The microstructure and electrochemical performance were collected before and after heat treatment. Figure 5.7 (a) shows the microstructure of 10 mol. % CeO_2& LNO co-infiltrated electrode. It can be seen that the nano-particles distribute on the LSCF surface more uniform with diameter about 50nm. And comparing with pure LNO infiltration, more flat and hetero-structured contact areas were obtained in CeO_2& LNO co-infiltrated electrode, since CeO2 infiltration solution has more strong wettability on the LSCF substrate. The microstructure of samples after the heat treatment shows in Figure 5.7 (b) and (c), the great mass of nano-particles are still less than 100nm and the nanoparticles are still attached on LSCF backbone tightly. Compared with the microstructure of pure LNO infiltrated electrode after long-term cell testing with constant current density as shown in Figure 5.7 (d), the particles growth were inhibited by the addition of CeO_2 particles apparently. But the surface of the CeO_2& LNO nano-particles became coarser, which may produce more low energy plane on the surface and decrease the surface kinetic properties. But more details about the electrochemical treatment need to be detected in our future.

And the electrochemical performance for the LNO-infiltrated LSCF and CeO_2& LNO co-infiltrated LSCF cathode were characterized by measuring the electrochemical impedance spectra of the symmetrical cell as a function of time. The Fig.5.8 shows the cathode resistance of the symmetrical cells under OCV. It indicates that the CeO_2 nanoparticles inhibit the degradation of the infiltrated electrode in the first three hundreds hours. The degradation rate of CeO_2& LNO co-infiltrated LSCF cathode is much smaller than that of pure LNO infiltration. But more repeatable electrochemical experiments need to be finished under electrochemical and heat treatment conditions. And the full cells with CeO_2-based materials & LNO infiltrated LSCF cathode will be assembled, and the stability of the cathode will be characterized and analyzed in the future.

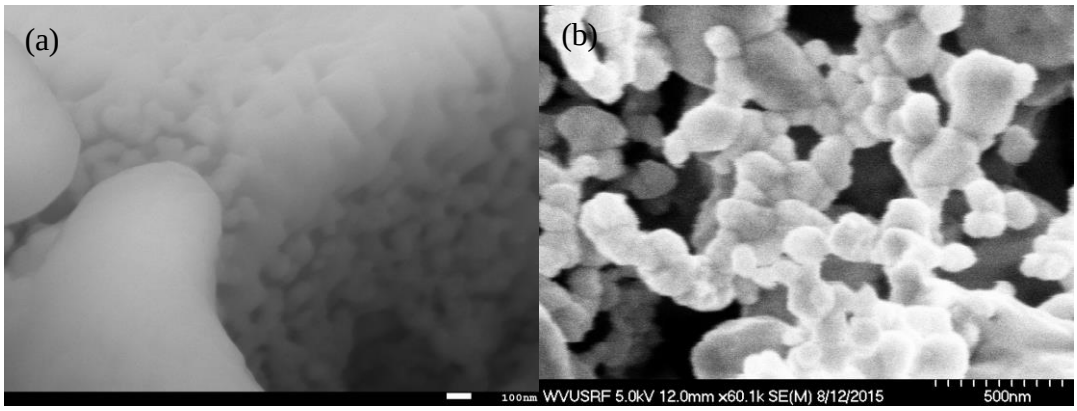

Figure 5. 1 SEM image of LSCF cathode with LNO infiltration (a) without long-term operation and (b) with 1000h long-term operation under a constant current density of 250 mA·cm^{-2} .

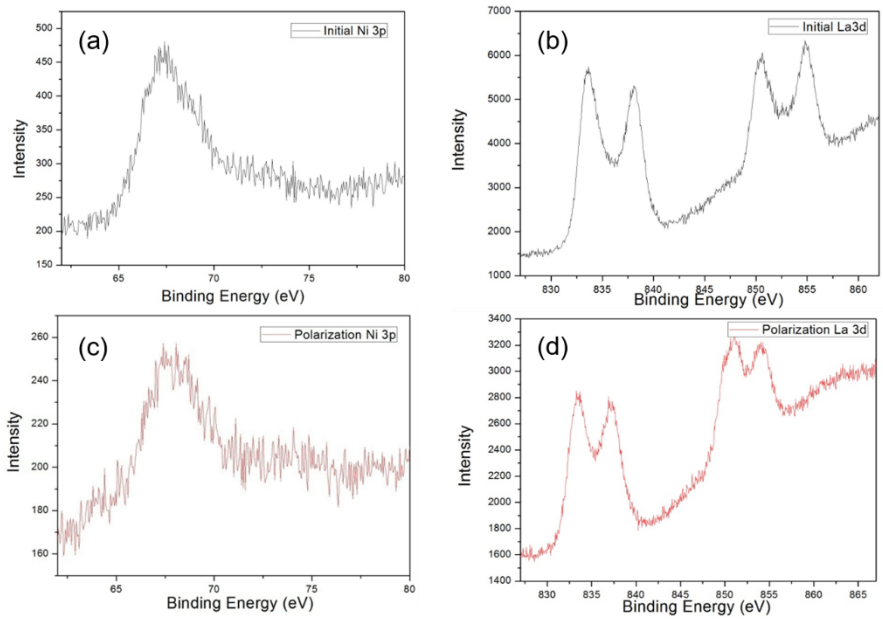

Figure 5. 2 La 3d and Ni 3p XPS spectra of (a) the surface of La2NiO4-δ-coated LSCF before cathodic polarization and (b) the surface of La2NiO4-δ-coated LSCF after cathodic polarization

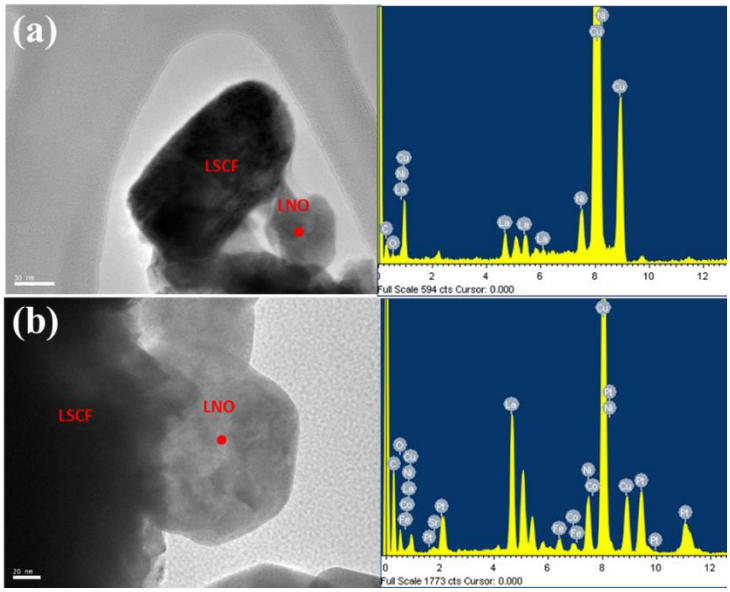

Figure 5. 3 TEM images and EDAX spectra of LNO-infiltrated LSCF cathode (a) before on-cell testing and (b) after long term testing.

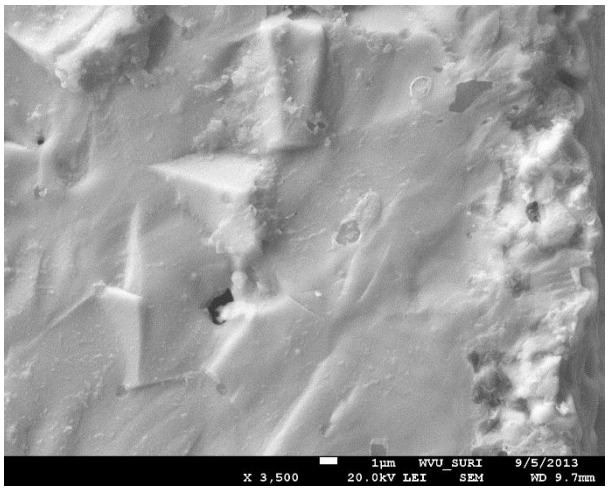

Figure 5. 4 Cross-section morphology of LNO-coated LSCF material.

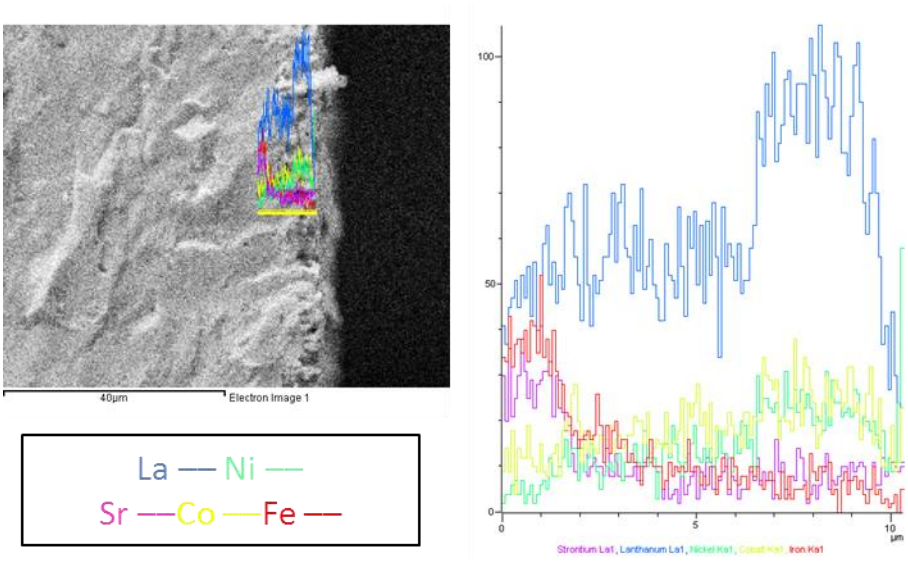

Figure 5. 5 EDX line scan results for LNO-coated LSCF.

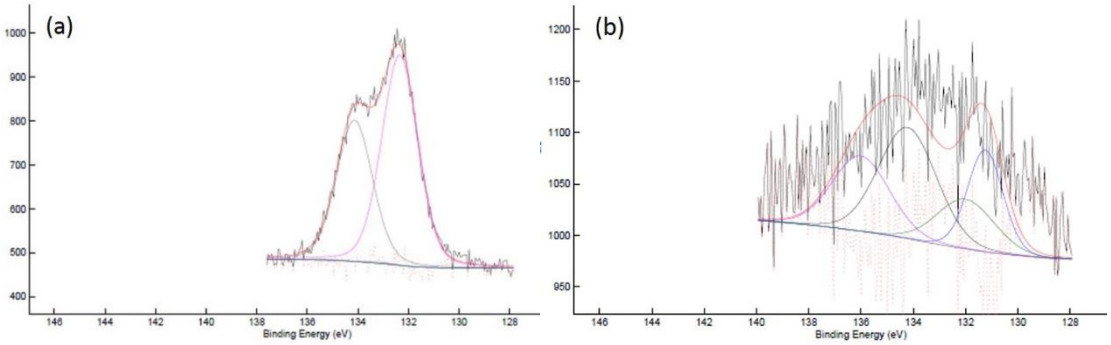

Figure 5. 6 Sr 3d XPS spectra of (a) the surface of LSCF and (b) the surface of La2NiO4-δ-coated LSCF.

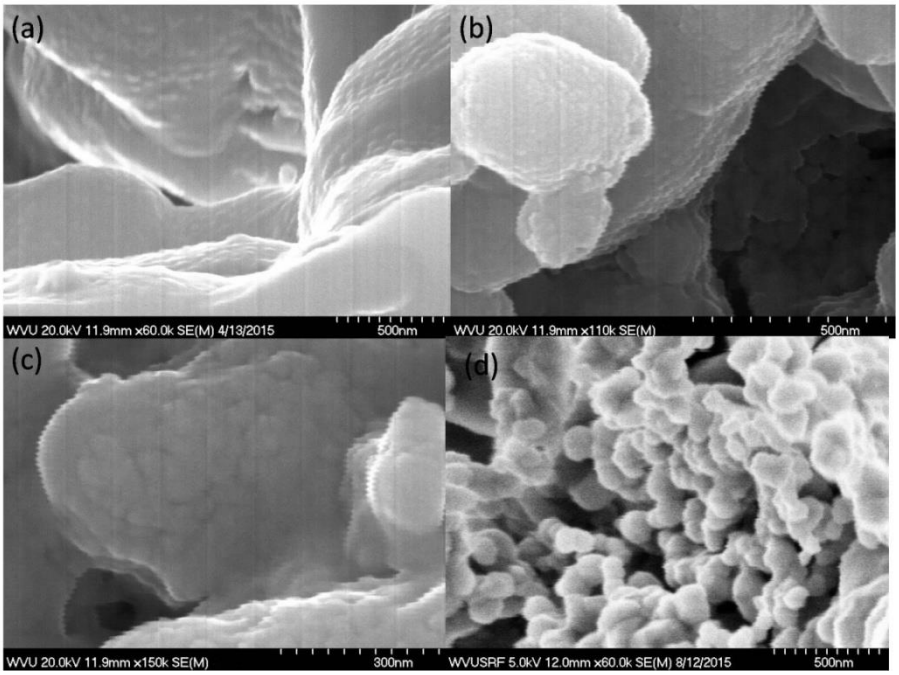

Figure 5. 7SEM image of LNO-based infiltrated electrode (a) 10 mol. % CeO2 co-infiltrated into electrode initially, (b) 10 mol. % CeO2 co-infiltrated into electrode with 150h heat treatment at 750oC, (c) 10 mol. % CeO2 co-infiltrated into electrode with 300h heat treatment at 750oC and (d) without CeO2 infiltration for long-term testing at constant current density at 750oC

Task 5.2 Fuel Cells Stability under Constant Current Density

Figure 5.8 presents the current-voltage characteristics and the corresponding power density for anode-supported fuel cells using bare LSCF or LNO-infiltrated LSCF cathodes during long-term operation of about 500 h at 750°C. The open circuit voltages (OCVs) for both on-cells are very close to the theoretical value derived from the Nernst equation, which demonstrates that the cells are well sealed with a gas-tight electrolyte. The power densities show an initial increase with the extension of time, indicating the activation process of cathode materials. The maximum power densities for the on cells with the cathodes of LSCF and LNO-infiltrated LSCF reach 418 and 697 $mW \cdot cm^{-2}$ after duration of around 100 h, respectively. Hence, a 67% increase in the power density has been achieved through infiltration LNO into LSCF backbone. Even after around 500 h, LNO-infiltrated LSCF still can deliver power density of 637 $mW \cdot cm^{-2}$, which is much higher than pure LSCF electrode with power density of 392 $mW \cdot cm^{-2}$. Figure 5.10 indicates the voltage of the test cells as a function of time at a constant current density of 250 $mW \cdot cm^{-2}$ at 750°C. The obviously higher voltage achieved by using LNO-infiltrated LSCF, as compared to pure LSCF cathode, further confirm that the LNO nanoparticles can serve as high-performance electro-catalyst. However, both of them have experienced a degradation of voltage with the extension of time. In the case of bare LSCF cathode, the voltage drops from 0.841-0.839 to 0.839-0.836 V, showing a degradation rate of 0.36% over 500 h. This is lower than the values reported in the literature (e.g. 0.9-1.5% per 1,000 hour) for LSCF cathodes operated under similar conditions. The relatively high stability of pure LSCF cathode provides us a good baseline and high standard for the study of LNO infiltration.

In contrast, the cell using LNO-infiltrated LSCF cathode exhibits performance degradation of about 0.39 % with a voltage drop from0.952-0.949 to 0.949-0.946 V after 500 h. Thus, a slightly higher degradation rate is obtained for LNO-infiltrated LSCF cathode than LSCF itself. Compared to the reports of LSCF based cathodes including modified LSCF with other surface catalysts, as showed much higher degradation rate of the cathodes, the LNO-infiltrated LSCF cathodes with good long-term stability over 500 h seems to be promising candidates for SOFC application. As far as the similar degradation rate for both LSCF and LNO-infiltrated LSCF cathodes is concerned, the extended durability measurements will be carried out in the future.

In addition, XRD refinements using Rietveld method have been carried out for dense LNO-LSCF to obtain the detailed crystal structure information and explain the *k* and *D* variation, such as cell parameters and Ni-O/La-La bond distance. A shifted Cherbyshev background function and pseudo Voigt peak shape were used in the refinement process. A best fit to the experimental data was obtained in the tetragonal I4/mmm space group with the La occupying (0,0,z) position, Ni occupying (0,0,0) position and two kinds of oxygen occupying (0,0,z) and (0,1/2,0) position. Refined crystal structure information was shown in Figure 5.10 and Table 5.1, 5.2, 5.3 and 5.4. For the bond length analysis, we can find that the La-O2 (*1) bond length decreases after LNO applied on LSCF surface. Figure 5.11 shows the crystal structure of LNO, the distance of La-O2(*1) bond represent the length of AO rock salt layer which is critical for the oxygen interstitial transport located in the oxygen or lanthanum tetrahedron. The decrease of La-O2 (*1) will reduce the space of interstitial oxygen transport channels and further influence the oxygen transport properties. The oxygen atomics occupy in two position shows in Table. 5.1-5.4. It indicates that the concentration of oxygen vacancy decreases in LNO layer coated on LSCF surface. And if the interstitial oxygen atomics were added in the crystal model occupying the 16n site in tetragonal, after modification, it can be found that the occupancy of interstitial is higher in LNO-LSCF than that in pure LNO phase. Most researchers believed that the oxygen incorporation processes in LNO are controlled by interstitial oxygen state in AO rock salt layer. The higher interstitial oxygen and oxygen vacancy concentration can enhance surface oxygen incorporation and transport rate on LSCF/LNO surface and interface. However, it's worth noticing that the large error and Uiso value will influence the accuracy of interstitial oxygen occupancy, more detail and precise oxygen transport properties should be characterized by modifying the model and oxygen bulk transport testing.

For the A-site deficient LNO infiltrated LSCF cathode, the initial R_p values of $La_{2-x}NiO_{4+\delta}$ (x=0-0.2) coated LSCF cathodes increase with increasing the concentration of lanthanum deficient, which is consistent with the pure $La_{2-x}NiO_{4+\delta}$ (x=0-0.2) cathode properties because of its surface electro-catalytic. But after -0.2V cathodic polarization for 960min, the degradation of $La_{2-x}NiO_{4+\delta}$ (x=0-0.2) coated LSCF reduces with increasing lanthanum deficient concentration, as shown in Figure 5.12. The enhanced stability of $La_{2-x}NiO_{4+\delta}$ (x=0-0.2) coated LSCF demonstrates that A-site deficient $La_{2-x}NiO_{4+\delta}$ is one potential infiltration materials for bare LSCF cathode to improve the surface stability.

For the CeO2 & LNO co-infiltrated LSCF cathode, to primary confirm the influence of CeO_2 nano-particles on the nano-particles growth, the electrode undergone heat treatment at 750^{o}C for 300h. The microstructure and electrochemical performance were collected before and after heat treatment. Figure 5.13 (a) shows the microstructure of 10 mol. % CeO_2& LNO co-infiltrated electrode. It can be seen that the nano-particles distribute on the LSCF surface more uniform with diameter about 50nm. And comparing with pure LNO infiltration, more flat and hetero-structured contact areas were obtained in CeO_2& LNO co-infiltrated electrode, since CeO2 infiltration solution has more strong wettability on the LSCF substrate. The microstructure of samples after

the heat treatment shows in Figure 5.13 (b) and (c), the great mass of nano-particles are still less than 100nm and the nanoparticles are still attached on LSCF backbone tightly. Compared with the microstructure of pure LNO infiltrated electrode after long-term cell testing with constant current density as shown in Figure 5.13 (d), the particles growth were inhibited by the addition of CeO_2 particles apparently. But the surface of the CeO_2& LNO nano-particles became coarser, which may produce more low energy plane on the surface and decrease the surface kinetic properties. But more details about the electrochemical treatment need to be detected in our future.

And the electrochemical performance for the LNO-infiltrated LSCF and CeO_2& LNO co-infiltrated LSCF cathode were characterized by measuring the electrochemical impedance spectra of the symmetrical cell as a function of time. The Fig.5.14 shows the cathode resistance of the symmetrical cells under OCV. It indicates that the CeO_2 nanoparticles inhibit the degradation of the infiltrated electrode in the first three hundreds hours. The degradation rate of CeO_2& LNO co-infiltrated LSCF cathode is much smaller than that of pure LNO infiltration. But more repeatable electrochemical experiments need to be finished under electrochemical and heat treatment conditions. And the full cells with CeO_2-based materials & LNO infiltrated LSCF cathode will be assembled, and the stability of the cathode will be characterized and analyzed in the future.

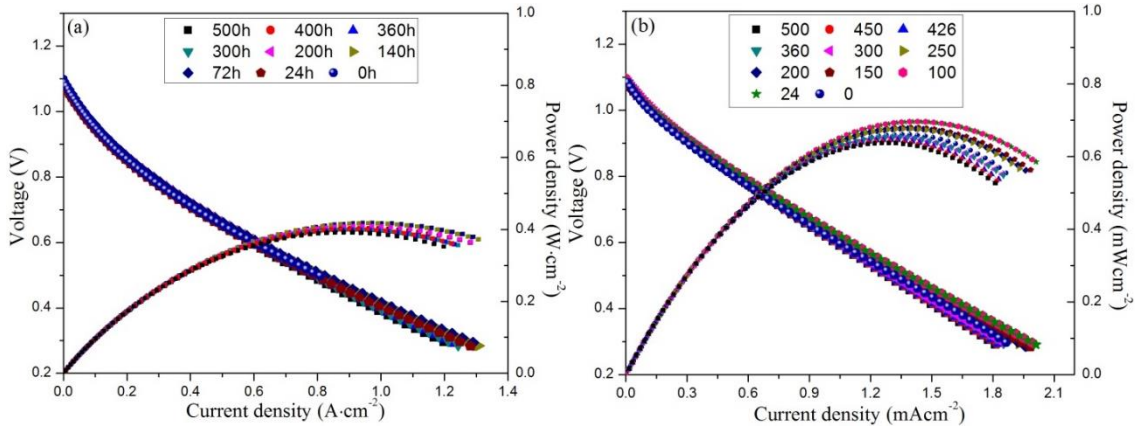

Figure 5. 8 Cell voltage and power density as function of current density for (a) pure LSCF and (b) LNO-infiltrated LSCF measured at 750oC during cell operation of 500 h.

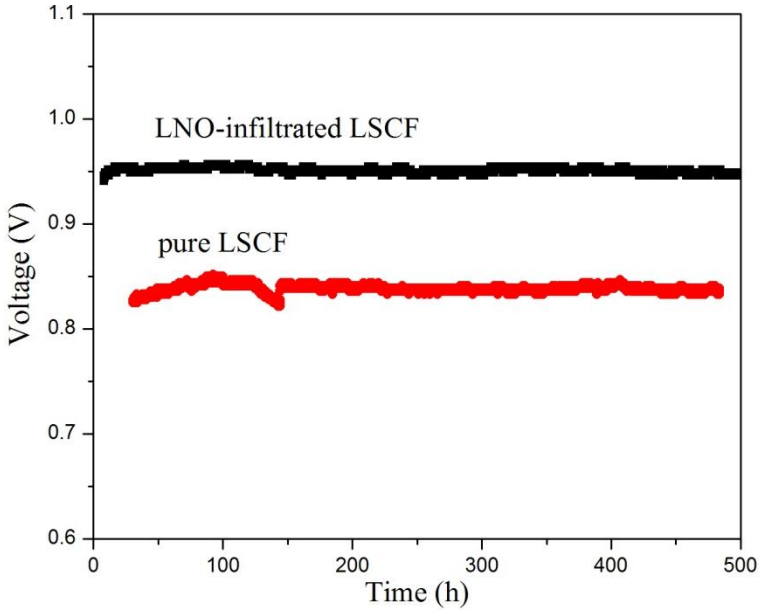

Figure 5. 9 Cell voltage as function of time at a constant current density of 250 mA cm-2 for both bare LSCF and LNO-infiltrated LSCF.

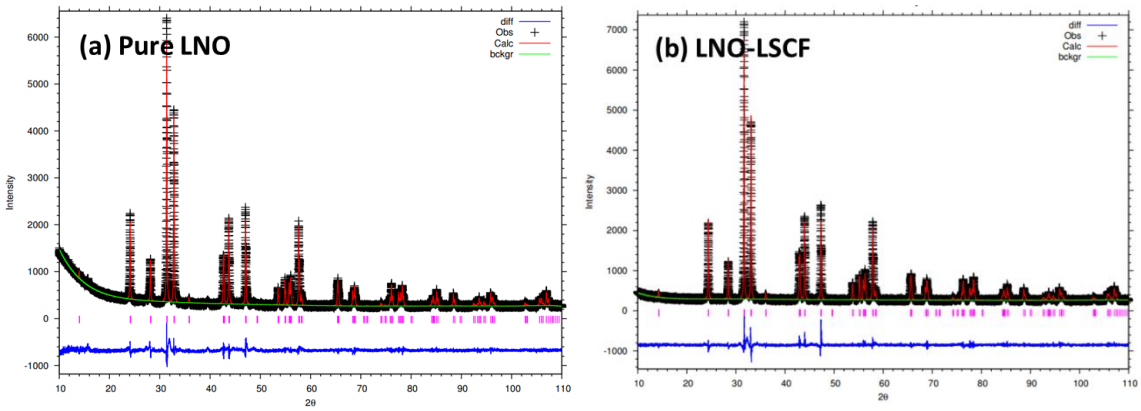

Figure 5. 10 XRD data for (a) pure LNO pellet and (b) LNO layer coated on LSCF surface recorded at room temperature. (+) represent the experimental data points, solid red line is refined data fit.

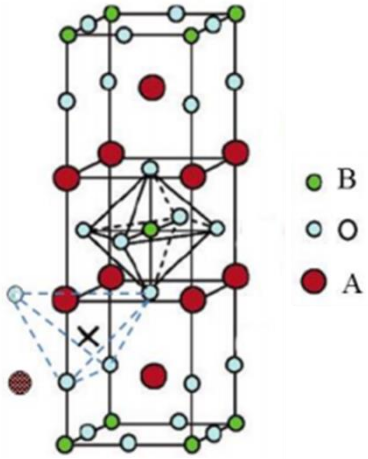

Figure 5. 11 The crystal structure of A2BO4 (*) represent the interstitial oxygen atomics.

Table 5. 1 Refined cell parameters and error value in I4/mmm space group

	a	b	c	R_{wp} (%)	R_p (%)	χ^2
Pure LNO	3.86127	3.86127	12.68641	6.39	4.68	1.689
LNO-LSCF	3.86768	8.36768	12.69597	6.64	4.96	1.541

Table 5. 2 Refined atomic position for pure LNO in I4/mmm space group

	x	y	z	occupy	U_{ISO}
La1	0.00000	0.00000	0.36058	1	0.01147
Ni1	0.00000	0.00000	0.00000	1	0.01131
O1	0.00000	0.50000	0.00000	0.9432	0.02833
O2	0.00000	0.00000	0.16961	0.9832	0.02833
	*				
O3	0.74087	0.00000	0.15985	0.154	0.06283

Table 5. 3 Refined atomic position for LNO layer coated on LSCF in I4/mmm space group.

	x	y	z	occupy	UISO
La1	0.00000	0.00000	0.36018	1	0.01041
Ni1	0.00000	0.00000	0.00000	1	0.01214
O1	0.00000	0.50000	0.00000	1.0030	0.03110
O2	0.00000	0.00000	0.17385	0.9767	0.03110

	*				
O3	0.65000	0.00000	0.23000	0.188	0.05000

Table 5. 4 Refined band length in I4/mmm space group.

	La-O1 (4)	La-O2 (1)	La-O2 (4)	Ni-O1 (4)	Ni-O2 (2)
Pure LNO	2.618	2.423	2.757	1.931	2.153
LNO-LSCF	2.625	2.366	2.769	1.934	2.207

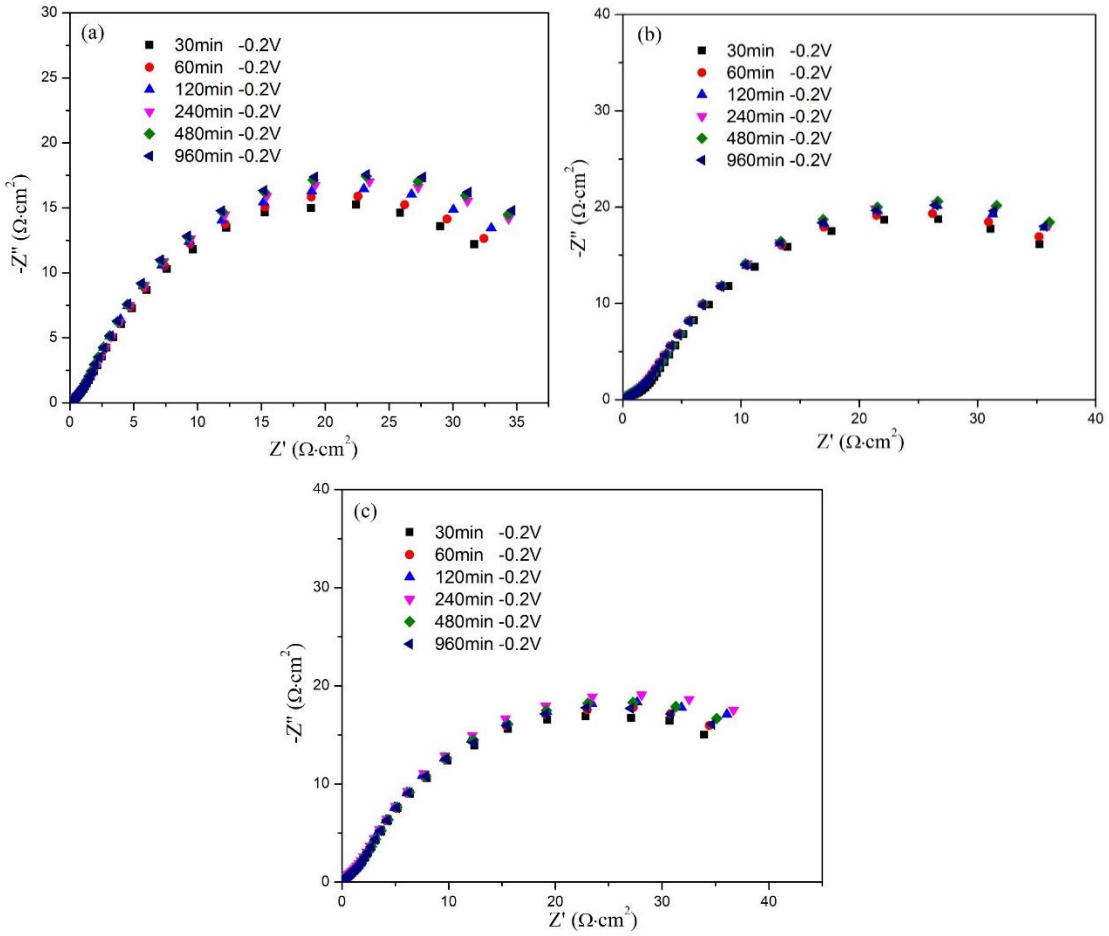

Figure 5. 12 Nyquist plot of three electrode cell with A-site deficient La2-xNiO4+δ coated LSCF cathode at 700oC after -0.2V cathodic polarization (a) La2NiO4+δ, (b) La1.95NiO4+δ and (c) La1.85NiO4+δ.

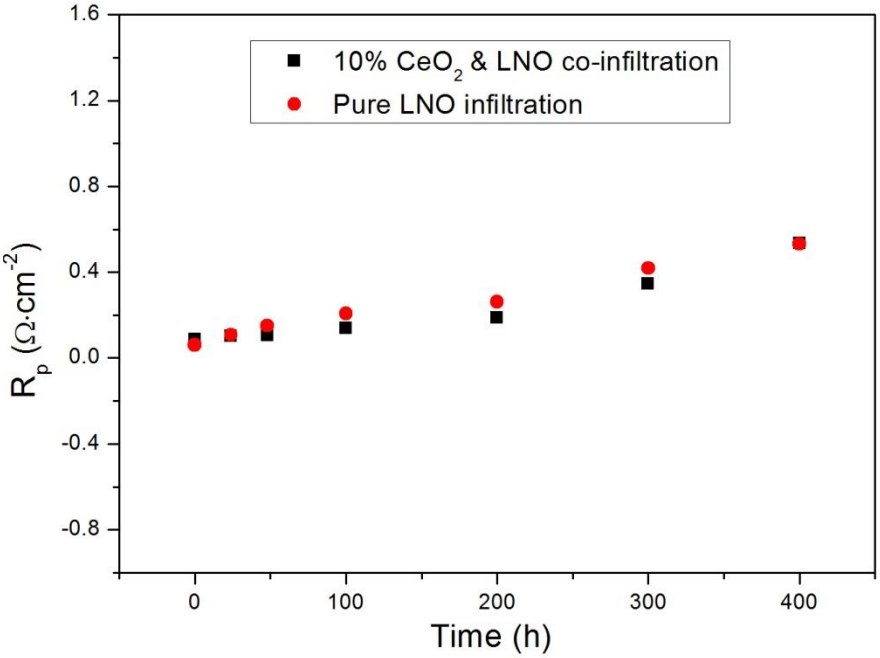

Figure 5. 13 Cathode resistance calculated from EIS within 500h heating treatment under 750oC in air.

3.0 Conclusions

New unique hetero-structured cathode has been developed in this project. $La_2NiO_{4+\delta}$ (LNO) as a surface catalyst with interstitial oxygen defects was introduced onto the state-of-the-art bulk $(La_{0.6}Sr_{0.4})_{0.95}Co_{0.2}Fe_{0.8}O_{3-\delta}$ (LSCF) to enhance the surface-limited ORR kinetics for cathode side. Furthermore, the hetero-structured cathode surface maintains high activity under electrode polarization with fewer negative effects from surface cation segregation of Sr, which is known to cause degradation issues for conventional LSCF and LSC cathodes, thus improving the cathode long-term stability. The higher interface oxygen exchange coefficient (3×10-4 cm/s), with respect to that of bare LSCF cathode (9.02×10-5cm/s), indicates that the incorporation rate of oxygen into LSCF is enhanced when using LNO/LSCF cathode. A low degradation rate of 0.39% at a constant current density for the fuel cell using LNO-infiltrated LSCF cathode can be still achieved after long-term durability of about 500 h at 750^{o}C. The interface chemistry distribution and oxygen transport properties have been studied to prove the enhancement of power out and stability of LNO-infiltrated LSCF cathode. The Co and Sr diffusion, as well as higher interstitial oxygen and oxygen vacancy concentration, have been detected in surface LNO layer by XPS and TEM-EDX data. For the first time, a physical model is proposed to illustrate how unique interstitial species on hetero-structured cathode surface work to regulate the exchange rate of the incorporation reaction. The further investigation demonstrates that CeO_2 & $La_{2-x}NiO_{4+\delta}$ (x=0-0.2) co-infiltrated LSCF is one potential infiltration materials for bare LSCF cathode to limit nano-particles growth/delamination and further improve the surface stability based on CeO_2 high melting point & wetting properties and $La_{2-x}NiO_{4+\delta}$ high surface chemical stability.

Fundamental understanding of the surface oxygen exchange and bulk oxygen transport properties under over-potential conditions across cathode materials have been carried out in this project. The alternation of the local chemical composition of the electrode materials and electrical boundary conditions under service condition usually ~0.3 V over-potential have been discussed and compared to the Nernst equation that is generally applied to treat any oxide electrodes under equilibrium. It is found that the electrode bulk is not locally electroneutral and the resultant electrostatic gradient can be established in the region near electrolyte due to the uneven distributions of ions and electrons. Therefore, besides the concentration gradient, electrical field force produced by the electrostatic potential is also the driving forces in the ion diffusion and introduces new concepts in handling chemical and electrical contributions in the overall electrochemical response of electrode system. Meanwhile, the uncoordinated relationship on electrode resistance is found between thermodynamic (oxygen partial pressure) and electrochemical (over-potential) activated conditions based on the Nernst equation. This Non-Nernst behavior demonstrates that it should be cautious to choose the effective activity or concentration used in Nernst equation to build the equivalence relation between thermodynamic and electrochemical driving force and predict performance of electrode.

4.0 Future Work

The future work of the LNO-LSCF hetero-structured cathode will focus on the following:

- The stability of the anode-supported full cells with CeO_2-based materials & A-site deficient LNO infiltrated LSCF cathode need to be characterized after more than 1000h operation in the future;
- Further fundamental understanding of the altered oxygen conduction behavior across the surface/bulk interface between materials of quite different oxygen transport properties in order to provide scientific rationale and quantified criteria for cathode design;

5.0 Products Produced

Xinxin Zhang, Hui Zhang, Xingbo Liu. *High performance La2NiO4+δ-infiltrated (La0.6Sr0.4) 0.95 Co0.2Fe0.8O3−δ cathode for solid oxide fuel cells*. Journal of Power Sources, 2014, DOI:10.1016/j.jpowsour.2014.06.132

Bo Guan, Wenyuan Li, Hui Zhang, Xingbo Liu. *Oxygen Reduction Reaction Kinetics in Sr-Doped La2NiO4+ δ Ruddlesden-Popper Phase as Cathode for Solid Oxide Fuel Cells.* Journal of the Electrochemical Society, 2015*,* DOI:10.1149/2.0541507jes

Bo Guan, Wenyuan Li, Xinxin Zhang, Xingbo Liu. *Surface Oxygen Exchange Properties of Sr Doped La2NiO4+ δ as SOFC Cathode: Thin-Film Electrical Conductivity Relaxation Investigation.* ECS Transactions, 2015, DOI:10.1149/06801.0801ecst

Wenyuan Li, Bo Guan, Xinxin Zhang, Jianhua Yan, Yue Zhou, Xingbo Liu, *New Mechanistic Insight into the Oxygen Reduction Reaction on Ruddlesden-Popper Cathodes for Intermediate-Temperature Solid Oxide Fuel Cells.* Physical Chemistry Chemical Physics, 2016 DOI: 10.1039/C6CP00056H

Wenyuan Li, Bo Guan, Jianhua Yan, Nan Zhang, Xinxin Zhang, Xingbo Liu, *Enhanced surface exchange activity and electrode performance of* $(La_{2-2x}Sr_{2x})(Ni_{1-x}Mn_x)O_{4+\delta}$ *cathode for intermediate temperature solid oxide fuel cells,* Journal of Power Sources, DOI:10.1016/j.jpowsour.2016.04.022